

INFORMATION TO USERS

This manuscript has been reproduced from the microfilm master. UMI films the text directly from the original or copy submitted. Thus, some thesis and dissertation copies are in typewriter face, while others may be from any type of computer printer.

The quality of this reproduction is dependent upon the quality of the copy submitted. Broken or indistinct print, colored or poor quality illustrations and photographs, print bleedthrough, substandard margins, and improper alignment can adversely affect reproduction.

In the unlikely event that the author did not send UMI a complete manuscript and there are missing pages, these will be noted. Also, if unauthorized copyright material had to be removed, a note will indicate the deletion.

Oversize materials (e.g., maps, drawings, charts) are reproduced by sectioning the original, beginning at the upper left-hand corner and continuing from left to right in equal sections with small overlaps.

**ProQuest Information and Learning
300 North Zeeb Road, Ann Arbor, MI 48106-1346 USA
800-521-0600**

UMI[®]

NORTHWESTERN UNIVERSITY

**X-ray Investigations of Ferroelectric Thin Films and Related
Surface Structures**

A DISSERTATION
SUBMITTED TO THE GRADUATE SCHOOL
IN PARTIAL FULFILLMENT OF THE REQUIREMENTS

for the degree of
DOCTOR OF PHILOSOPHY

Field of Physics and Astronomy

By

David Marasco

EVANSTON, ILLINOIS

December 2002

UMI Number: 3071678

Copyright 2002 by
Marasco, David

All rights reserved.

UMI[®]

UMI Microform 3071678

Copyright 2003 by ProQuest Information and Learning Company.
All rights reserved. This microform edition is protected against
unauthorized copying under Title 17, United States Code.

ProQuest Information and Learning Company
300 North Zeeb Road
P.O. Box 1346
Ann Arbor, MI 48106-1346

© Copyright by David Marasco 2002
All Rights Reserved

ABSTRACT

X-ray Investigations of Ferroelectric Thin Films and Related Surface Structures

David Marasco

The field of ferroelectrics has been of great interest of late due to its technological potential in the field of computer memory. While there has been considerable study into the electrical properties of these materials, many details of the atomic-scale structure are as yet unknown.

In this work, the x-ray standing wave (XSW) technique was used to determine the structure of the (3x2) and (2x1) Sr/Si(001) sub-monolayer reconstructions, and an extension of the technique for thin films was used to probe the polarity of both as-grown PbTiO₃/SrTiO₃(001) thin films and switched Ag/Pb(Zr_{0.3}Ti_{0.7})O₃/SrRuO₃/SrTiO₃(001) capacitor structures. For the Sr/Si(001) system, Sr was deposited at room temperature in a UHV environment, and surface structures were grown by annealing the Si substrate, desorbing the Sr to different coverages. The coverage measurements were compared to those found in the literature, and using XSW data combined with STM information from the literature, it was concluded that Sr occupies the cave site. The XSW method has been applied to thin films, using the weak reflections from the films themselves to generate a standing wave field. By observing the fluorescence signal from ions in the

films, the structure of the films, in this case the polarity, can be probed. Epitaxial films of the ferroelectric perovskite PbTiO_3 grown on $\text{SrTiO}_3(001)$ by metalorganic chemical vapor deposition (MOCVD) were examined by the thin-film XSW method. For 100, 200 and 400 Å films, the films exhibited both high crystalline quality and a preference for unipolar growth. The 600 Å sample was of lower quality and contained domains of both up and down polarizations. The capacitor structures containing $\text{Pb}(\text{Zr}_{0.3}\text{Ti}_{0.7})\text{O}_3$ as a switchable dielectric were electrically examined and then left in a known switched state. The electrical measurements revealed that the samples were strongly imprinted, showing a preference for one orientation. Thin-film XSW measurements revealed that the capacitors left in the preferred polarization state remained in that state, while one of the capacitors in the hard state had backswitched to the easy state. The thin-film XSW method successfully probed these systems in a non-destructive manner, in contrast to traditional electrical measurements.

ACKNOWLEDGEMENTS

First and foremost I'd like to thank my thesis advisor Michael Bedzyk for his support and patience through the years.

Then there are the medical professionals who fixed my lungs and stomach. Life is much more enjoyable when you have your health.

I'd like to thank all of my co-workers in the Bedzyk group. Drs. Paul Lyman and Alexander Kazimirov deserve special attention for all the knowledge they imparted to me, and also for their good natures. Dr. Tien-Lin Lee taught me a great deal about running a beamline and programming simulations. Duane Goodner has my gratitude for cheerfully doing extra dirty work when my health took a dip.

I also extend my thanks to the other partners in this project: on the ferroelectric growth side, Carol Thompson, Orlando Auciello, Stephen Streiffer, Chris Foster, G.-R. Bai and C.B. Eom, and on the beamline side, the staffs at both the DND-CAT and BESSRC-CAT at the Advanced Photon Source, with special notice to Dennis Keane, John Quintana, Gordon Knapp, Mark Beno, Guy Jennings and Chuck Kurtz.

My roommates had to put up with a lot over the years. While I've lived with a number of interesting people, Tom Haard, Dmitry Epstein and Kirill Vorobeychik suffered the most damage. Don't hate yourselves in the morning.

I wouldn't have made this without help from my friends. Greg Lopez, who has been a storyteller for as long as I can remember. Anthony Mrse, a man who understood the rigors of graduate school and the limits of health. Jill Murphy, always just a phone call

away. Locally, Brian Robinson and Tom Renbarger provided strong support that perhaps went underappreciated at times. Brian also lent his editing talents to this project. Thanks for everything guys. And of course there are my parents and brother. They made me who I am and kept me sane. And then there is Fleur. Words can't say enough to express my gratitude.

TABLE OF CONTENTS

ABSTRACT	iii
ACKNOWLEDGEMENTS	v
LIST OF FIGURES	x
LIST OF TABLES	xiv
Chapter 1 Introduction	1
Chapter 2 An Overview of Thin Films of Ferroelectrics	5
2.1 Introduction	5
2.2 Structure and Thin Film Growth of Perovskites	7
2.3 Novel Measurements of Ferroelectric Thin Films	10
Chapter 3 X-ray Methods and Theory	14
3.1 The X-ray Standing Wave Technique	14
3.1.1 Introduction	14
3.1.2 The X-ray Standing Wave Field	16
3.2 Thin Film X-ray Standing Waves	20
3.3 Dynamical Diffraction from Thin Slabs	24
3.3.1 Introduction	24
3.3.2 The Takagi – Taupin Equations	25
3.3.3 Recursion Formulae for the Reflected Amplitude Ratios	27
3.3.4 Total Amplitude	31
3.4 The Evanescent Wave Effect for Probing Thin Films	32
3.5 Crystal Truncation Rod Measurements	36

Chapter 4 Experimental Setup	39
4.1 Optics and Detectors for X-ray Measurements	39
4.2 Ultra High Vacuum Chamber	44
Chapter 5 XSW Measurements of the Sr/Si(001) Surface Structure	50
5.1 Introduction	50
5.1.1 Background	50
5.1.2 Previous Studies of Sr/Si(001)	51
5.2 Sample Preparation	55
5.3 Sr/Si(001) XSW Results	57
5.4 Discussion of Sr/Si(001) Results	69
Chapter 6 Thin Film X-ray Standing Wave Measurements of	
MOCVD-Grown PbTiO₃ / SrTiO₃	75
6.1 PbTiO ₃ Structure and Growth	75
6.2 PbTiO ₃ Thin Film Experimental	77
6.3 PbTiO ₃ XSW Results	79
6.3.1 Overview	79
6.3.2 100 Å Sample	80
6.3.3 400 Å Sample	80
6.3.4 200 Å & 600 Å Samples	81
6.4 PbTiO ₃ CTR Measurements	95
6.4.1 PbTiO ₃ 100 Å CTR Experimental	95
6.4.2 PbTiO ₃ 100 Å CTR Results	97
6.5 Discussion of X-ray Measurements of the PbTiO ₃ / SrTiO ₃ System	102

Chapter 7 Thin-Film X-ray Standing Wave Measurements of	
MOCVD-Grown $\text{Pb}(\text{Zr}_{0.3}\text{Ti}_{0.7})\text{O}_3 / \text{SrTiO}_3$	106
7.1 PZT Capacitor Structure and Growth	106
7.2 PZT Experimental	109
7.3 XSW Results for PZT Capacitor Structures	113
7.4 Discussion of XSW Measurements	120
 Chapter 8 Summary	 122
 References	 126
 Appendix 1 Software Written for This Dissertation	 132
A1.1 Introduction	132
A1.2 Description of the XSW Fitting Software	132
A1.3 Flow Charts of the XSW Fitting Program	134
A1.4 Description of Routines for the XSW Fitting Program	136
A1.5 Description of the CTR Fitting Software	139
A1.6 Flow Charts of the CTR Fitting Program	141
A1.7 Description of Routines for the CTR Fitting Program	142

LIST OF FIGURES

2.1.1	Ideal hysteresis loop for a ferroelectric material.	6
2.2.1	The atomic arrangement that defines the perovskite crystal structure family.	7
2.2.2	Diagram of a standard MOCVD deposition system.	9
3.1.1	X-ray standing wave field in and above a perfect crystal.	15
3.1.2	Fluorescence yield as a function of angle for different (004) coherent positions.	18
3.2.1	Use of an XSW field generated by a reflection from the substrate to probe a thin film.	21
3.2.2	Profile of reflectivity and E-field intensity at the Pb site as a function of depth.	23
3.3.1	Reflected and transmitted amplitude ratios from a thin slab.	28
3.4.1	Theoretical XSW results using Pb $L\alpha$ and Ti $K\alpha$ as the observed fluorescence signal while scanning through the (001) Bragg reflection of a 400 Å thick PTO film.	32
3.4.2	Two experiments, illustrating the evanescent-wave effect.	33
3.4.3	Evanescent-wave effect near the critical angle. Ti $K\alpha$ photons with an energy of 4.51 keV emitted from PTO.	35
4.1.1	Setup of an XSW experiment at an undulator beamline at the Advanced Photon Source.	40
4.1.2	Side-view of the post-mono table.	41
4.1.3	λ vs. θ DuMond diagram for the x-ray optics at the APS undulator beamlines at 18.5 keV	42
4.2.1	Top view of the UHV system at the BESSRC 12ID-D undulator beamline.	45

4.2.2	Filament calibration for the heater in the MBE chamber.	46
4.2.3	Sample manipulator from the x-ray chamber (shown removed from UHV chamber).	47
4.2.4	Geometry for UHV XSW.	48
5.1.1	Phase diagram of the Sr/Si(001) system, and LEED results as a function of coverage and annealing temperature.	51
5.1.2	Si(001) surface and possible Sr occupation sites.	53
5.2.1	Thickness of Sr on Si(001) substrate as a function of time, measured by quartz crystal thickness monitor.	56
5.2.2	LEED diffraction patterns from the Sr/Si(001) surface.	59
5.2.3	LEED images and inverted LEED images for the (2x1) surfaces.	60
5.2.4	LEED images and inverted LEED images for a (3x2) surfaces.	61
5.3.1	The x-ray fluorescence spectrum recorded by a Si(Li) solid-state detector from a 0.6 ML Sr/Si(001) surface.	62
5.3.2	XSW measurement of the as-deposited unannealed Sr/Si(001) surface.	63
5.3.3	The XSW results of the 1 minute 750°C (2x1) surface.	64
5.3.4	The XSW results of the 10 minute 700°C (2x1) surface.	65
5.3.5	The XSW results of the (3x2) 004 surfaces.	66
5.3.6	The XSW results of the 022 reflection of the (3x2) surface	67
5.3.7	The XSW results of the substrate Si fluorescence signal for the high Sr coverage (2x1) sample	68
5.4.1	The positions of the Sr atoms as determined by XSW for the three different measured coverages.	72
5.4.2	Proposed models for the (2x1) and (3x2) reconstructions.	73
6.1.1	Room-temperature unit cells of PTO in the “Up” and “Down”	76

orientations, respectively.

6.2.1	Fluorescence data collected by the Si(Li) detector for the 100 Å PbTiO ₃ film grown on SrTiO ₃ (001).	78
6.3.1	100 Å film (001) reflection.	82
6.3.2	100 Å film (001) reflection.	83
6.3.3	100 Å film (001) reflection.	84
6.3.4	100 Å film (002) reflection.	85
6.3.5	100 Å film (002) reflection.	86
6.3.6	400 Å film (001) reflection.	87
6.3.7	400 Å film (001) reflection.	88
6.3.8	400 Å film (002) reflection.	89
6.3.9	400 Å film (001) reflection at 8.0 keV for Ti fluorescence.	90
6.3.10	400 Å film (002) reflection at 8.0 keV for Ti fluorescence.	91
6.3.11	200 Å film (002) reflection.	92
6.3.12	600 Å film (001) reflection.	93
6.3.13	600 Å film (001) reflection.	94
6.4.1	Determination of the CTR in reciprocal space.	95
6.4.2	The relationship between the miscut angle α of the sample surface normal with respect to the substrate (001) vector, the path of the CTR in reciprocal space and the misalignment angle γ between the film and sample lattice.	96
6.4.3	CTR scan of the PTO/STO (001) system at 13.5 keV, over the full range of the scan.	98
6.4.4	The δ dependence of the interference near the STO (001) peak.	99
6.4.5	CTR scan of the PTO/STO (001) system at 13.5 keV, in the region of	99

interference between the PTO and STO (001) peaks.

6.4.6	Side view lattice depiction for the best fit up and down orientations of PTO/STO(001) from CTR measurements.	101
6.5.1	Side view of the PTO structure.	104
7.1.1	A side view depiction of the PZT capacitor heteroepitaxial structure.	106
7.1.2	PZT phase diagrams from Jona and Shirane.	107
7.1.3	Map of the sample.	108
7.2.1	Polarization vs. voltage hysteresis loops for two capacitors.	110
7.2.2	Fluorescence data collected by the Si(Li) detector for the PZT ferroelectric capacitor structure.	111
7.2.3	Output of the single channel analyzer tuned to Ag L fluorescence.	112
7.3.1	Theta-Two Theta scan of capacitor pad D4M2.	115
7.3.2	Capacitor D2M0: poled in the down orientation.	116
7.3.3	Capacitor D3M2: poled in the up orientation.	117
7.3.4	Capacitor D2M2: poled in the down orientation.	118
7.3.5	Capacitor D4M2: poled in the up orientation.	119
A1.3.1	Flow chart for the boss.m routine.	134
A1.3.2	Flow chart relating Xh.m, wyh.m and their components.	135
A1.6.1	Flow chart detailing the CTR fitting routines.	141

LIST OF TABLES

5.3.1	Annealing history, LEED pattern, coverage and XSW data for the Sr/Si(001) surfaces examined in this study.	58
6.3.1	Summary of XSW measurements on PTO/STO reflections.	79
6.4.1	Fitting parameters used for fitting equation [3.5.5] to the CTR data of the 100 Å PTO film.	97

Chapter 1 - Introduction

Recently, there has been much interest in the field of ferroelectric thin films, mainly due to the possible applications in the field of non-volatile ferroelectric random access memories (NVFRAM). For the most part, past studies have concentrated on macroscopic electrical measurements of these systems; in this dissertation, we use the x-ray standing wave (XSW) and other non-destructive x-ray techniques. With these methods we examined the growth of Sr on Si on the atomic scale, important for the integration of ferroelectrics with semiconductor structures, the as-grown polarity of thin films of PbTiO_3 , and the effects of electrical switching on capacitor structures containing thin films of $\text{Pb}(\text{Zr}_{0.5}\text{Ti}_{0.5})\text{O}_3$.

A brief overview of ferroelectrics is presented in Chapter 2. Section 2.1 describes ferroelectrics and their possible applications. Section 2.2 details the crystal structure of perovskites and their growth via metalorganic chemical vapor deposition (MOCVD). Section 2.3 is a quick survey of novel non-electrical probes of ferroelectric thin films.

In Chapter 3 I discuss the x-ray methods used in this dissertation. Section 3.1 introduces the traditional x-ray standing wave (XSW) measurement as an atomic-scale structural probe. This technique is used in the Sr/Si(001) study found in Chapter 5. Section 3.2 extends the XSW method by using an epitaxial thin film as the generator of the standing wave field. As knowledge of the E -field ratio is necessary when interpreting thin-film XSW experiments. Section 3.3 discusses the Takagi-Taupin equations and both Bartels' and Lee's work on iterative formulae for thin slabs of diffracting material. The thin-film XSW method is used to study epitaxial ferroelectric thin films in Chapters 6 and

7. Sections 3.4 and 3.5 discuss the evanescent-wave effect and crystal truncation rod (CTR) method, two more x-ray tools used in this study.

Chapter 4 is devoted to the hardware used in the experiments described in Chapters 5, 6 and 7. These experiments took place at the Advanced Photon Source at the DND-CAT 5ID-C and BESSRC-CAT 12ID-D undulator beamlines. The post-monochromator optics and data collection systems are discussed in Section 4.1. The surface systems measured in Chapter 5 were grown in the UHV chamber located at the 12ID-D beamline. The chamber and its growth and analysis tools are described in Section 4.2.

Chapter 5 covers the surface structures for the sub-monolayer Sr/Si(001) system. A quick review of the previous work in the field, including proposed surface reconstructions, is given in Section 5.1. Section 5.2 describes our growth methods and contains LEED images for five observed surfaces. Our XSW results are presented in Section 5.3, and based upon those measurements and the previous studies discussed in Section 5.1, coverages and occupation sites for the (3x2) and (2x1) Sr/Si(001) surface reconstructions are proposed. We found that the (3x2) reconstruction existed at 1/6 of a monolayer, and the Sr atoms occupied the cave site. We found the (2x1) reconstruction at both 0.57 monolayers and 0.31 monolayers and also proposed the cave site, although it appears that there are two different surfaces at the different coverages, and the Sr atom is positioned closer to the Si(001) surface in the low coverage case.

Chapter 6 discusses the PbTiO₃/SrTiO₃ (001) system (PTO/STO). Films of the ferroelectric PTO were deposited at various thicknesses by metalorganic chemical vapor

deposition (MOCVD) on to STO substrates. Section 6.1 gives a brief overview of the growth of the films. Section 6.2 discusses the collection of the thin-film XSW data, including the use of the evanescent-wave effect to distinguish Ti fluorescence from the film from the Ti signal from the bulk. Section 6.3 presents the results of the thin-film XSW measurements, and Section 6.4 presents the collection of CTR data and results derived from that measurement. Section 6.5 summarizes the previous two experimental sections. The 100, 200 and 400 Å PTO films are found to be of excellent epitaxial quality and also highly oriented in one orientation. The relationship between the phase of the Pb and Ti fluorescence signals is discussed in terms of the structure factor of the PTO crystal. The 600 Å films display poor rocking curves and are of low crystalline quality. This may be due to the growth of strain-reducing a domains, which is suppressed at the thicknesses of the other films that were measured.

Chapter 7 presents XSW measurements of switched $\text{Pb}(\text{Zr}_{0.3}\text{Ti}_{0.7})\text{O}_3$ (PZT) ferroelectric thin-film capacitors. Section 7.1 is a description of the structure and growth of the capacitors, which consist of an STO substrate, an epitaxial SrRuO_3 bottom electrode, the PZT dielectric and a polycrystalline Ag top electrode. Section 7.2 describes the experimental setup for the measurements, including the electrical testing and switching of the capacitors, and the use of the Ag fluorescence signal to properly navigate on the array of capacitors. Section 7.3 presents thin-film XSW and electrical hysteresis data on four capacitors, two left in the down orientation and two left in the up orientation. Section 7.4 discusses the electrical and XSW findings. The thin films are found to be imprinted, with the down orientation being the easy state. The two capacitors

left in the down orientation stayed in the down orientation. Of the two capacitors left in the up orientation, the one that was imprinted in the down orientation lost its switched polarity and was found in a mixed state. Suggestions for more work on the PZT system are given.

This dissertation is briefly summarized in Chapter 8. The software written for analyzing some of the data in this thesis is discussed in the Appendix.

Chapter 2 – An Overview of Thin Films of Ferroelectrics

2.1 Introduction

Ferroelectrics get their name from their similarities to ferromagnetic materials. Like their magnetic counterparts, ferroelectrics are organized in a domain structure [1]. With the application of an external electric field, the domains align with the field to lower the net dipole moment energy. If a large enough field is applied along a polarization axis, all of the domains align with the field. When the external field is removed, the sample will exhibit a nonzero polarization. A hysteresis loop showing a ferroelectric's response to an external electric field is shown in Figure 2.1.1. The nomenclature follows the magnetic original.

In the zero-field condition, a ferroelectric can be understood as a device that exists in one of two stable states, polarized up or down. Since it is a binary system and requires no applied field (except for read/write operations), ferroelectrics are a good candidate for nonvolatile digital memory (NVFRAM). NVFRAM could compete in three different markets in the \$150 billion dollar range. Based on cost and density, NVFRAMS could compete against FLASH, EEPROMs, DRAMs and SRAMs. Due to its fast write times and non-volatile nature, NVFRAM can be used in “smart cards” used for fare collection, inventory control and other applications. In fact, ferroelectric thin films have already found their way into everyday life in the form of these low-density-memory smart cards. Finally, NVFRAM can be used in “system-on-chip” applications, where it does not need the added complexity of power transistors, as do EEPROMs and FLASH [2].

In addition to its switching properties, the perovskite family of ferroelectrics also possesses a high dielectric constant. This makes them a candidate to replace SiO_2 in dynamic random access memory (DRAM) capacitor structures [3.4]. As the size of memory elements shrink, memory makers have resorted to building complex structures in order to maximize the surface area of the SiO_2 dielectric. Eventually, the SiO_2 will have to be replaced by another material, as the techniques that manufacturers use to increase dielectric surface area will not be able to keep pace with size constraints demanded by the need for increasing capacitor density.

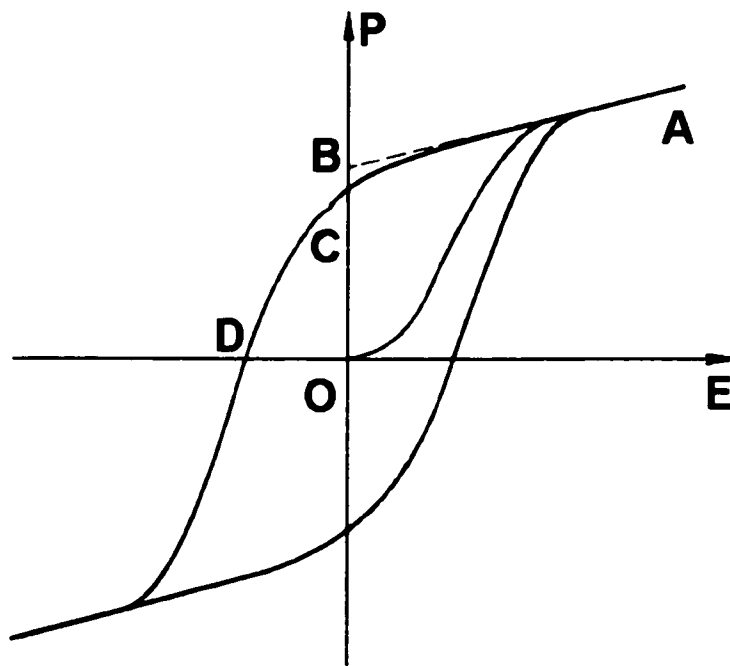


Figure 2.1.1 Ideal hysteresis loop for a ferroelectric material. The applied electric field is plotted along the x-axis and polarization along the y-axis. The nomenclature follows that found in ferromagnetic materials. Saturation, when all the domains are in one direction, is achieved at point A. As the field is reduced back to zero, some of the domains will revert to the opposite state. Extrapolation to point B gives the spontaneous polarization, and the actual value at zero field, C, is the remnant polarization. The external electric field required to reduce the polarization to zero is D, the coercive field.

2.2 Structure and Thin Film Growth of Perovskites

Perovskite is the complex oxide CaTiO_3 . Crystals following the same crystal structure as CaTiO_3 are grouped as perovskites. This includes many oxides of the form ABO_3 but is not exclusive; double fluorides such as KMgF_3 and KZnF_3 are also perovskites [1]. The basic perovskite crystal structure is shown in Figure 2.2.1. In the cubic phase, the oxygen anions occupy the face-center positions, the A cations occupy the corners of the cubic unit cell, and the B cations sit in the body-centered position. Small displacements of the A and B cations from their positions relative to the oxygen sublattice give rise to a spontaneous polarization. Many ferroelectric perovskites are tetragonal in their

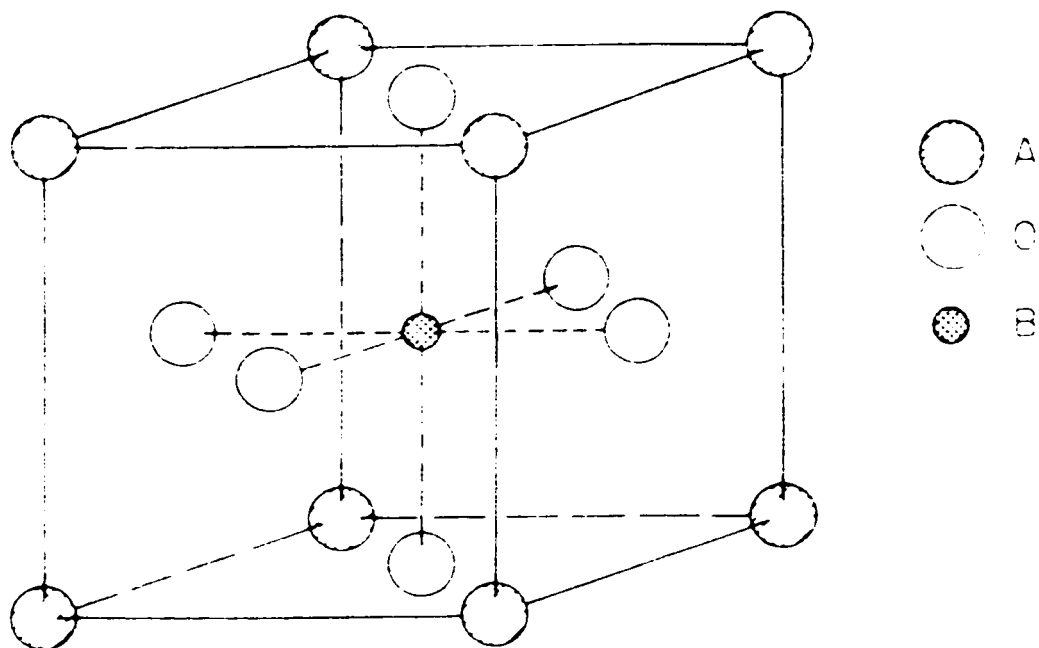


Figure 2.2.1 The atomic arrangement that defines the perovskite crystal structure family. In the cubic form, the oxygen atoms occupy the face-centered positions, the A cations the corner sites, and the B cations the body centered position. Small structural distortions from the cubic symmetry create a spontaneous polarization.

ferroelectric phase; however, ferroelectricity is possible in any non-centrosymmetric configuration where the centers of negative and positive charge do not coincide.

The first perovskite shown to possess ferroelectric properties was BaTiO_3 [5,6]. In the almost 60 years following this discovery, many other perovskite materials have also demonstrated ferroelectric properties [1]. Until the late 1980s, most studies on perovskites centered on bulk specimens. The high electric field needed to switch the ferroelectric crystals was one of many problems that beset the field. With the development of better surface science techniques, it was realized that thin films of ferroelectric materials could perform where the bulk materials failed [7].

In studies of thin films of ferroelectric materials, many growth techniques have been utilized, including plasma sputter deposition (PSD) [8], ion beam sputter deposition (IBSD) [9], pulsed laser deposition (PLD) [10], molecular beam epitaxy (MBE) [11], sol-gel processing [12], metalorganic deposition (MOD) [13] and metalorganic chemical vapor deposition MOCVD [14]. Sol-gel is currently being used for deposition of low-density NVFRAM in industry, and PSD, IBSD, PLD and MOCVD are the most utilized methods for film synthesis [2]. As our collaborators used the MOCVD method to grow the ferroelectric thin films studied in this dissertation, we will concentrate our discussion only on this technique.

MOCVD is seen as the process with the greatest potential in the ferroelectric memory industry because of its excellent film growth properties, ease of scaling to ULSI and its current wide-spread use in the IC industry [2]. Figure 2.2.2 shows a typical MOCVD system, in this case a reactor for growth of $\text{Pb}(\text{Zr}_x\text{Ti}_{1-x})\text{O}_3$ (PZT) [15]. Various

liquid-source stainless steel bubblers contain the organometallic precursors for Pb, Ti and Zr. These bubblers are both temperature and pressure regulated in order to create the desired vapors. The precursor vapors are delivered to the reaction chamber by inert carrier gasses, in this case N_2 , in gas lines that are heated in order to prevent condensation of the precursors. In the reaction chamber, the precursor vapors and O_2 are mixed in a low-pressure environment in the presence of a heated substrate. Details of the growth of thin films of $PbTiO_3$ and PZT via MOCVD can be found in Chapters 6 7, respectively.

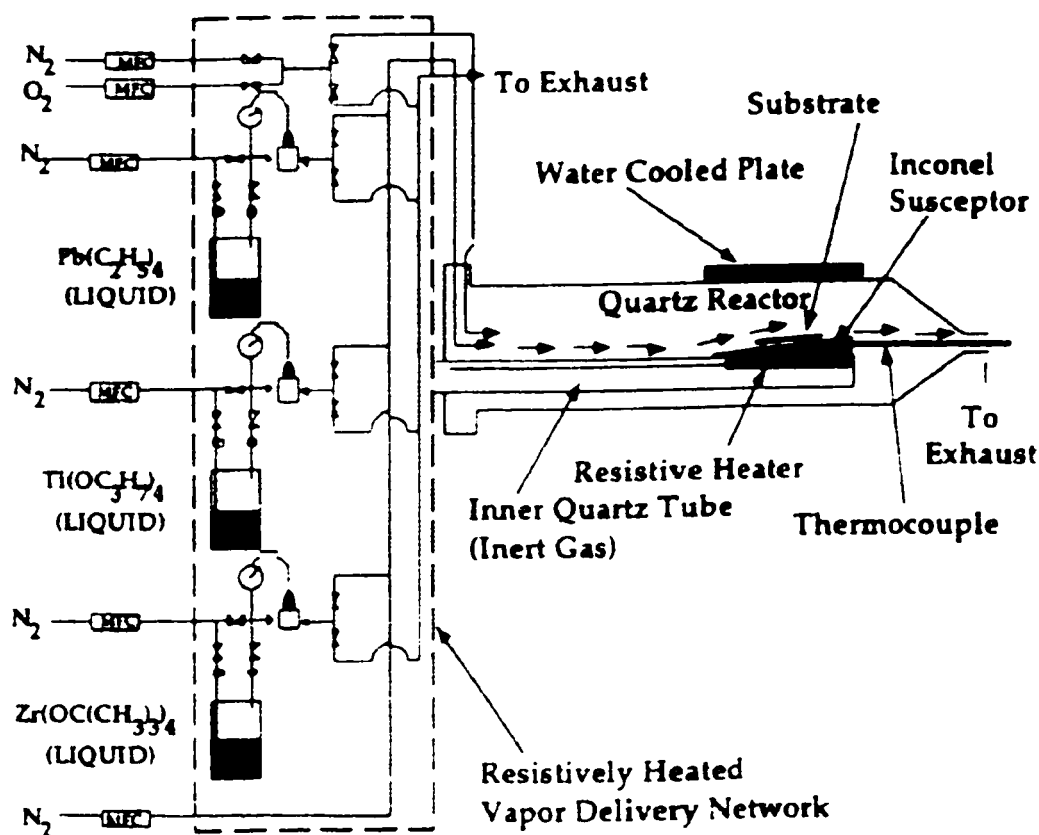


Figure 2.2.2 Diagram of a standard MOCVD deposition system. Liquid precursors are transported to the reaction chamber by carrier gases in heated lines in order to prevent condensation. In the chamber the film is grown on a heated sample [2].

2.3 Novel Measurements of Ferroelectric Thin Films

While domain switching in ferroelectric crystals is an electrical event, the use of macroscopic electrical measurements has its limitations. These probes do not reveal details of the atomic structure of the crystal; they are limited for the most part to the switchable domains in the ferroelectric and destroy the original state of the polarization. In this section we take a quick survey of some of the non-electrical techniques that have been used to directly probe the structure and ferroelectric properties of ferroelectric thin films.

Not surprisingly, imaging via microscopy has been used to examine the quality and structure of ferroelectric thin films. In a representative study, Stemmer *et al.* [16] used both plan-view and cross-sectional transmission electron microscopy (TEM) to study the relationship between film thickness and substrate on the formation of a domains in PbTiO_3 thin films. Recently, it was discovered that combined with other techniques, microscopy could be used to observe ferroelectric domains and even switch domains on the nanoscale. The first work that imaged ferroelectric domains by microscopy was Saurenbach and Terris's scanning force microscopy (SFM) work on $\text{Gd}_2(\text{MoO}_4)_3$ [17]. In this method, advanced greatly by Luthi and coworkers [18], an SFM tip is used as a top electrode. With ferroelectric samples grown on buffer layers that can be exploited as a bottom electrode, the SFM tip is biased with an AC signal to take advantage of the inverse piezoelectric effect. The local polarity of the thin film is measured by the vibrations created in response to the electrical signal. In addition, a DC voltage can be applied to the SFM tip, causing the domain directly under the tip to switch polarity. Use

of this technique allowed for the microscopic study by Gruverman of both fatigue [19] and polarization retention [20] in PZT films.

Like microscopy, x-ray diffraction has been used to provide basic information about ferroelectric thin films. X-ray diffraction measurements have been used to reveal details of crystalline quality, the presence of *a* domains, film thickness and other structural details of thin ferroelectric films. Recently, real-time *in situ* grazing-incidence x-ray scattering has been used to explore the surface and near surface structure of ferroelectric thin films. Munkholm and coworkers have used this technique to examine the surface of PTO films during growth [21]. PTO films with thicknesses ranging from 75 to 800 Å were deposited on STO(001) substrates at 950-1000 K via MOCVD. The samples were maintained at an elevated temperature, and the flow of the Pb precursor gas was continued in order to provide a Pb-rich environment during the x-ray study. In-plane scattering was monitored as the substrate temperature and Pb precursor pressure were varied. The phase diagram revealed a c(2x2) surface structure with a (1x6) reconstruction in the Pb-poor regions. The c(2x2) structure gave sharp diffraction peaks, indicating a well-ordered system. The (1x6) system gave broad peaks and was not studied further. To better understand the c(2x2) structure, 14 independent in-plane reflections were measured. By analyzing the intensity at these peaks, a single TiO₂ antiferrodistortive layer was proposed, with a rotation of the oxygen cages by about 10°. This result may be useful in the understanding of growth of ferroelectric films. Streiffer and coworkers have also used grazing-incidence diffraction to study stripe domains in ferroelectric films [22]. In bulk ferroelectrics, it has been observed that stripe domains,

consisting of domains polarized in opposite directions, occur with a regular periodicity. This helps to minimize the energy of the electric field due to the polarization of the sample. After growing PTO films via MOCVD, Streiffer observed in-plane scattering profiles as the temperature of the sample was lowered below the ferroelectric transition temperature. Odd-order satellite peaks were revealed around all hkl peaks except those with $l = 0$. The dearth of satellites at $l = 0$ implies that the polarization is out-of-plane along the c -axis, parallel to the polarization. The absence of even-order peaks suggests a 1:1 ratio of the domains, as would be expected from a field-canceling mechanism. These stripe domains vanished as the sample was lowered to room temperature.

While x-rays have been used extensively to probe the structure of ferroelectric films, until recently it was believed that the detection of the direction of polarization in a ferroelectric by diffraction was impossible due to Friedel's law [23]. What is at issue here is that only the magnitude of the structure factor, and not the phase, can be extracted from an intensity measurement. Ignoring anomalous dispersion, the magnitude of the structure factor is the same upon an inversion through the center; therefore, the difference in polarities cannot be detected. Thompson and coworkers have used the sharp interface between epitaxially grown thin films of perovskite ferroelectrics and single-crystal substrates to perform crystal truncation rod (CTR) experiments about the (001) peaks of both PTO and PZT. The interference between the fields scattered from the film and the substrate served to probe the structure of the film. For more details, see Section 3.5 of this dissertation. With the PTO experiment, they probed the polarity of the as-grown film [24]. The PZT experiment involved a capacitor structure that was switched electrically *in*

situ [25]. The two switched states were compared via the CTR method, and signs of imprint were found that were in agreement with electrical measurements. The capacitors were then cycled until fatigue became apparent, and further measurements showed a relationship between the imprinted state and fatigue.

Chapter 3 X-Ray Methods and Theory

3.1 The X-ray Standing Wave Technique

3.1.1 Introduction

The x-ray standing wave (XSW) technique is a chemically sensitive atomic-scale probe based upon the dynamical diffraction of x-rays. In the Bragg condition, interference between incident and diffracted plane waves creates a standing wave field both inside and above a crystal surface. The nodes and antinodes of the standing wave field have the same periodicity as the Bragg planes that created the reflection. As illustrated in Figure 3.1.1, as the sample is rocked through a Bragg peak, the antinodes of the standing wave field move down through the crystal, starting at a position halfway between the diffraction planes and ending on the diffraction planes. The diffraction plane position is defined by the phase of the structure factor [1]. The movement of the antinodes causes the modulation of the fluorescence yields of the atoms in or deposited on the crystal. By monitoring these yields, structural information about the crystal can be determined.

The existence of an XSW field inside a crystal was first demonstrated by Batterman while observing Bragg reflection on a Ge single crystal [2]. Batterman then monitored As K fluorescence from a doped Si (220) single crystal, proving that the XSW method can determine the position of impurity atoms in a bulk crystal [3]. The XSW technique was added to the arsenal of surface science tools when Cowan, Golovchenko, and Robins used the standing waves above a Si (220) crystal to determine the position in

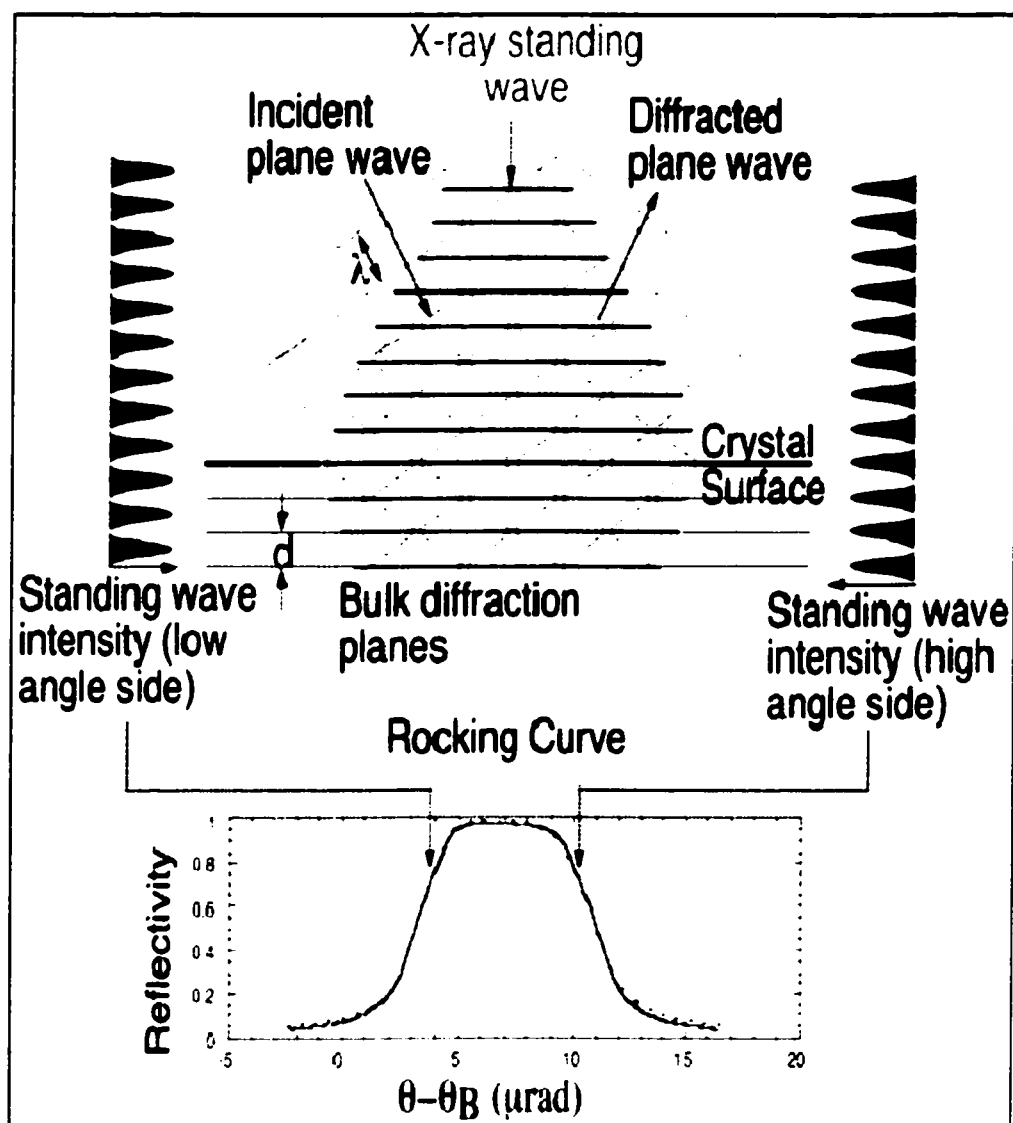


Figure 3.1.1 X-ray standing wave field in and above a perfect crystal. The incident wave diffracts from the crystal lattice. The incoming and outgoing waves interfere to create a standing wave field. The spacing of the antinodes is the same as that of the bulk diffraction planes. As the crystal is rocked through its reflection, the antinodes of the standing wave field move inwards from a position halfway between the bulk diffraction planes to a position coincident with the diffraction planes. By monitoring the fluorescence yield of the atoms in or on the crystal, structural information about the crystal or its adsorbates can be determined.

the surface normal direction of Br adsorbates [4]. In the two decades following the work of Cowan *et al.*, the XSW method has been applied to many systems. An extensive review of the technique and its application has been written by Zegenhagen [5]. In this section I will give a brief overview of the XSW method.

3.1.2 The Standing Wave Field

Under the Bragg condition, an incident electric field plane wave will diffract from a periodic lattice. The incident plane wave can be expressed as

$$\mathcal{E}_O(\mathbf{r}, t) = \mathbf{E}_O e^{2\pi i(\nu t - \mathbf{K}_O \cdot \mathbf{r})}, \quad [3.1.1]$$

and the diffracted wave as

$$\mathcal{E}_H(\mathbf{r}, t) = \mathbf{E}_H e^{2\pi i(\nu t - \mathbf{K}_H \cdot \mathbf{r})}, \quad [3.1.2]$$

where ν is the wave frequency and \mathbf{K}_O and \mathbf{K}_H are the incident and diffracted wavevectors inside the crystal, respectively. The total E-field inside the crystal is then

$$\mathcal{E}_T(\mathbf{r}, t) = [\mathbf{E}_O e^{-2\pi i \mathbf{K}_O \cdot \mathbf{r}} + \mathbf{E}_H e^{-2\pi i \mathbf{K}_H \cdot \mathbf{r}}] e^{2\pi i \nu t}. \quad [3.1.3]$$

As the Bragg condition is assumed, the wavevectors are related to the reciprocal lattice vector \mathbf{H} by

$$\mathbf{K}_H = \mathbf{K}_O + \mathbf{H}. \quad [3.1.4]$$

Assuming σ polarization (true for the experiments in this dissertation; this assumption will be used throughout the dissertation), the total E-field intensity near the surface can be normalized as

$$I(\theta, \mathbf{r}) = 1 + \left| \frac{E_H}{E_O} \right|^2 + 2 \left| \frac{E_H}{E_O} \right| \cos(\phi(\theta) - 2\pi \mathbf{H} \cdot \mathbf{r}), \quad [3.1.5]$$

where

$$\frac{E_H}{E_O} = \left| \frac{E_H}{E_O} \right| e^{i\phi}. \quad [3.1.6]$$

Therefore, $|E_H/E_O|^2$ is the reflectivity $R(\theta)$, and $\phi(\theta)$ is the phase of the XSW field. How $R(\theta)$ and $\phi(\theta)$ are derived from dynamical diffraction is covered in Zegenhagen [5].

In the dipole approximation, the photoeffect cross section is proportional to the E-field intensity at the center of the atom. Therefore, the characteristic fluorescence x-rays from these atoms will be linear with the intensity of the XSW field at the position of the atom in the atomic lattice. As the position of the antinodes sweeps through the unit cell as the crystal is rocked through a reflection, the normalized intensity of the fluorescence signal acts as a chemically sensitive structural probe. The fluorescence signal is collected in parallel with the reflected intensity. See Chapter 4 for experimental details. The normalized fluorescence yield from atoms near the surface can be expressed as

$$Y(\theta) = \int \rho(r) I(\theta, r) dr = 1 + R(\theta) + 2\sqrt{R(\theta)} f_H \cos(\phi(\theta) - 2\pi P_H), \quad [3.1.7]$$

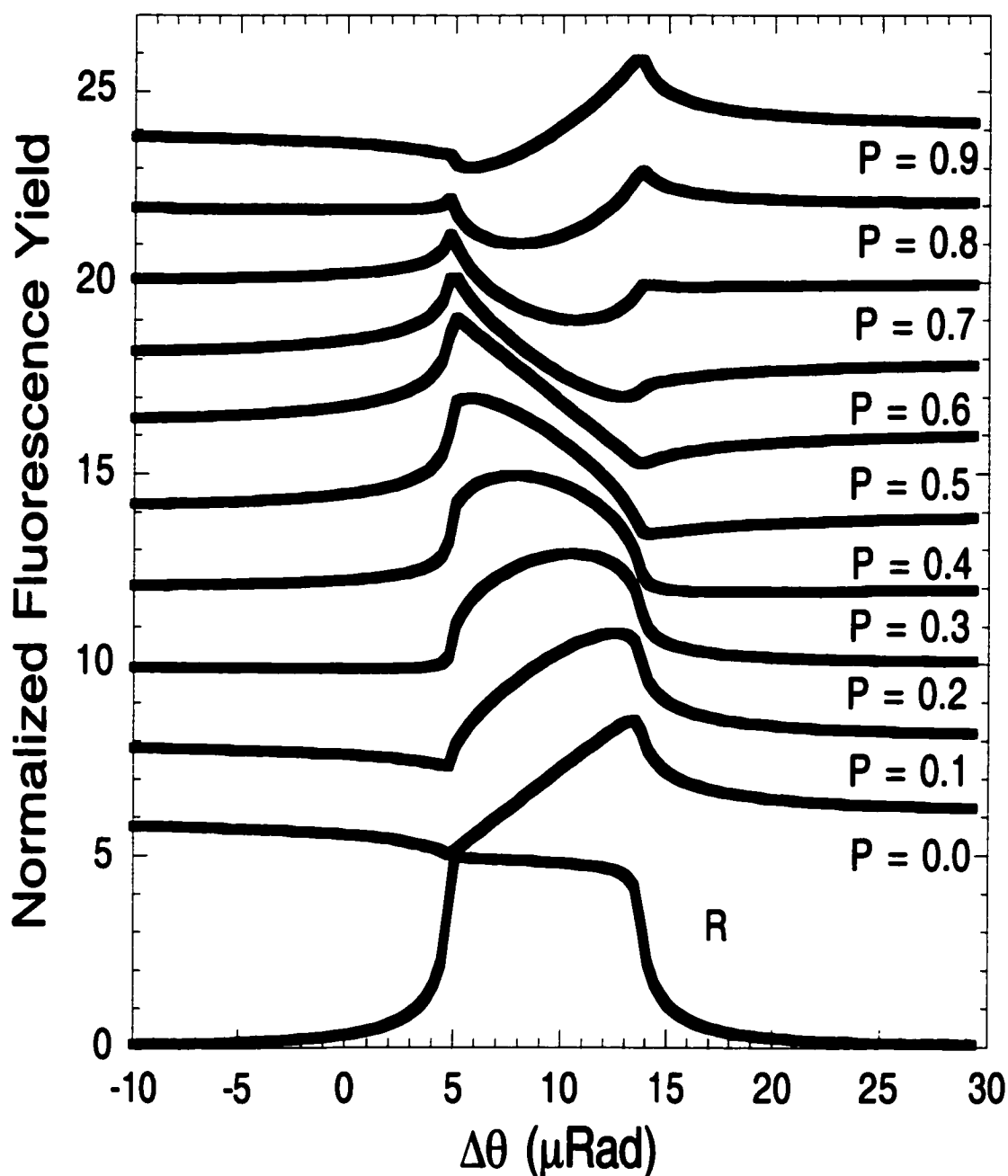


Figure 3.1.2 Fluorescence yield as a function of angle for different (004) coherent positions. This is a simulation of an Si(004) rocking curve, along with the normalized fluorescence yields corresponding to coherent positions at various places in the unit cell. An incoming energy of 13.5 keV and a coherent fraction of unity are assumed. The fluorescence yields are offset by 2 for each position for the sake of clarity, and the reflectivity is scaled by a factor of 5. In this simulation, the origin lies on a Si(004) atomic plane.

where the coherent fraction and coherent position, f_H and P_H , are defined as the amplitude and phase of the H th Fourier component \mathcal{F}_H of the normalized atom density $\rho(r)$,

$$\mathcal{F}_H = \int \rho(r) e^{2\pi i \mathbf{H} \cdot \mathbf{r}} d\mathbf{r} = f_H \exp(-2\pi i P_H), \quad [3.1.8]$$

with the integration over the volume of the unit cell. In more physical terms, the coherent position locates the fluorescing atoms relative to the origin, measured along the \mathbf{H} direction in units of the diffraction-plane spacing. See Figure 3.1.2 for a graph of fluorescence yield as a function of coherent position. The coherent fraction is a measure of the spread about this mean location and is usually split into three factors,

$$f_H = C a_H D_H, \quad [3.1.9]$$

each factor presenting a contribution to the spread in position. Each factor ranges from zero to unity. The ordered fraction C is a measure of what fraction of the atoms are coherently located, as opposed to distributed randomly in or above the crystal. The geometrical factor a_H accounts for the possibility of more than one preferred lattice site for the atoms. For example, assuming that the origin is on the diffraction planes, if all the atoms were at a point halfway between the diffraction planes, then the coherent position would be 0.5 and the geometrical factor would be 1. However, if the atoms were equally distributed between a pair of sites at 0 and 0.25, the coherent position would be 0.125, but the geometrical factor would be $1/\sqrt{2}$. Finally, to account for thermal vibrations, there is a Debye-Waller factor,

$$D_H = e^{-2\pi^2 \langle u_n^2 \rangle / d_n^2}, \quad [3.1.10]$$

where $\langle u_H^2 \rangle^{1/2}$ is the RMS value of the time-averaged displacement about the mean position.

Given several different non-colinear and higher order harmonic (hkl) reflections, information from the coherent positions and coherent fractions can be used to triangulate the positions and determine the vibrational amplitudes of atoms in or above the crystal. The combination of this method with intense synchrotron sources has allowed for the structural determination of many systems.

3.2 Thin-Film X-ray Standing Waves

X-ray standing waves have been used for the past two decades to determine the locations of impurities in bulk crystals and adsorbates on crystal surfaces. However, one limitation on the XSW technique is the need for near-perfect crystal substrates to generate the XSW field. A handful of crystals (Ge, Si, GaAs, etc.) can be grown in bulk perfectly enough to generate rocking curves that match the arc second wide curves that are calculated by dynamical diffraction theory. Deviations from calculations based upon perfect crystals are problematic and do not give clear results. However, many materials can be grown as high-quality thin films that cannot be grown as bulk crystals. These thin films can be used to generate an x-ray standing wave field that in turn can be used to probe the structure of the materials of interest.

A traditional XSW experiment uses the substrate crystal as a "generator" for an XSW field. When a suitable Bragg reflection is found, the incident plane waves interfere

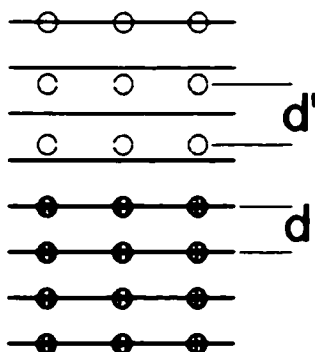


Figure 3.2.1 Use of an XSW field generated by a reflection from the substrate to probe a thin film. Since the lattice spacing of the substrate does not match that of the film, the antinodes of the x-ray standing wave field fall upon different regions of the film unit cell. Over many layers of film, the XSW measurement will see the film as being random in nature rather than structured. An XSW field with the same periodicity as the film is needed to properly probe the film.

with the diffracted plane waves, and an XSW field is created. As the crystal is rocked through its reflection, the antinodes of the XSW, which have the same periodicity as the diffraction planes that created the reflection, sweep through the crystal lattice. By monitoring the fluorescence of the atomic species in the system, structural information can be distilled from the experiment. Suppose this method was used to probe the structure of a film grown on top of a substrate. In most cases, the lattice parameters of the film would be different from those of the substrate. For a film that is a few layers thick, models can be made to account for the fact that the antinodes of the XSW field are incommensurate with the crystalline planes of the film. Figure 3.2.1 shows the case for thicker films. The XSW probe results in a measurement that indicates a film with a coherent fraction of zero. The solution is to examine the film with an XSW field that has the same periodicity as that of the film. The way to achieve this is to use the film itself

as an XSW field "generator" by rocking through one of the film's diffraction peaks. This technique was first demonstrated by Kazimirov and coworkers in 1997 [6].

When a film thinner than the extinction length undergoes diffraction, a very weak reflection is observed. The interference between the incident plane waves and the diffracted outgoing plane waves still creates an XSW field. This field, while weak, can be used to probe the position of atoms within the film or above the film surface. Inspection of equation [3.1.7] shows that the term containing structural information scales as the square root of the reflectivity. Therefore, even a reflection on the order of 0.01% will exhibit a 1% modulation in the characteristic fluorescence yield. To observe this weak modulation in a reasonable time frame, a high-intensity x-ray source is needed. See Chapter 4 for experimental details.

The expression used to describe traditional XSW experiments, equation [3.1.7], is valid in the case of thin films only for fluorescing atoms near the top of the film. As the reflected intensity, and therefore the strength and phase of the XSW field, are depth-dependent (Fig. 3.2.2), an integration over the thickness of the film is required to properly fit collected XSW data from atoms within the film. The formulae used to simulate the XSW field intensity through the depth of the film are discussed in the following section.

In traditional XSW measurements, the two fitting parameters are the coherent position and the coherent fraction. Inspection of equation [3.1.7] reveals the role of the coherent fraction; it acts as an amplitude parameter on the \sqrt{R} interference term in the fluorescence yield. In the case of an XSW field probing impurities or adsorbates, the

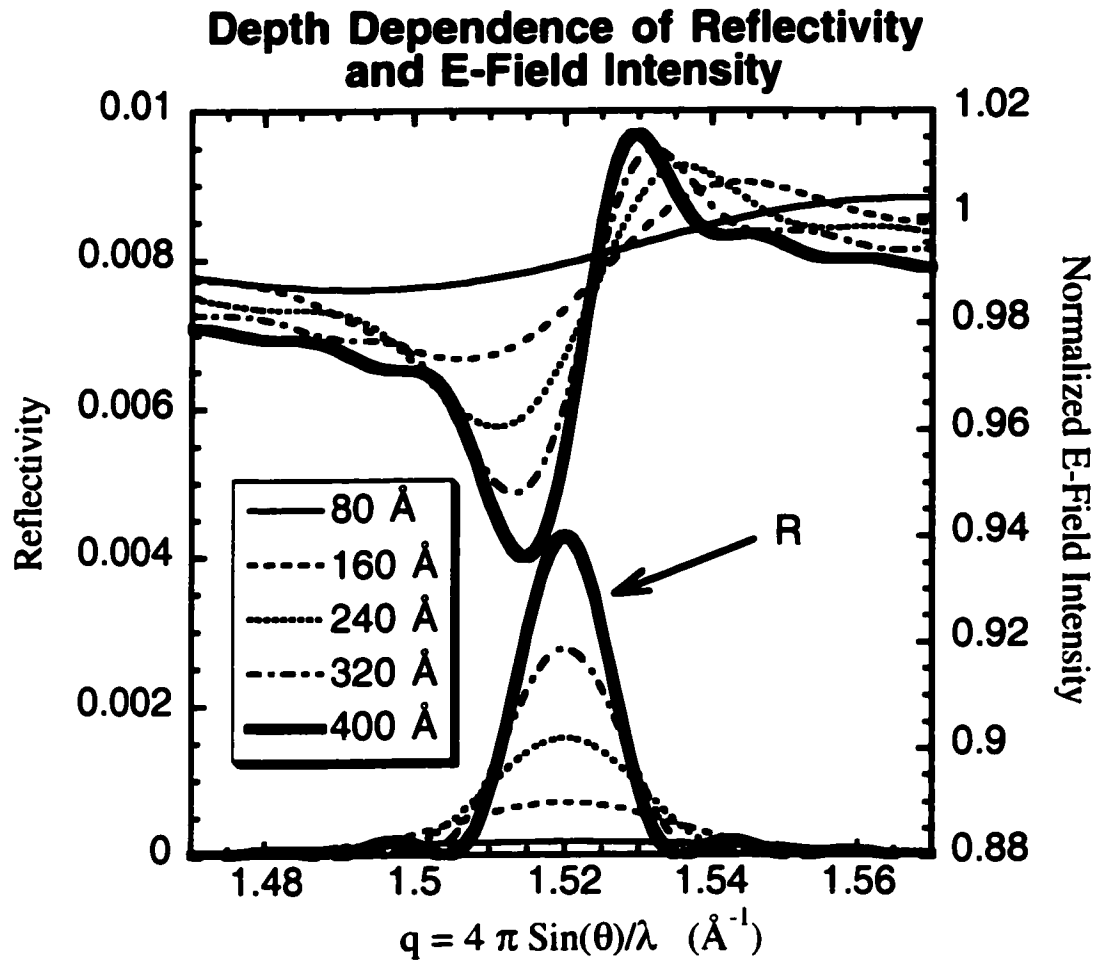


Figure 3.2.2 Profile of reflectivity and E-field intensity at the Pb site as a function of depth. The simulation is for the (001) reflection from a 400 Å film of PTO in the up orientation. The incident photon energy is 13.5 keV. The different lines correspond to 80, 160, 240, 320 and 400 Å above the bottom of the PTO film.

monitored atoms being excited by the field and fluorescing are an insignificant part of the structure that actually generates the field. This is not the case in the thin-film XSW experiment described in this thesis. The structure that is being examined also generates the XSW field, and hence a model that assumes that the coherent fraction and the reflectivity are independent is internally inconsistent. Take for example the extreme case, a film with a coherent fraction of zero. This film would not have the required structure to

diffract x-rays, but if equation [3.1.7] was applied, a nonzero reflectivity would be used. For a structure with only one site (where the geometric factor is unity), instead of using the coherent fraction, a static Debye-Waller factor can be used to modify the structure factor. This static Debye-Waller factor, which measures structural disorder, is an analog of the thermal Debye-Waller factor, which measures vibrations about a mean lattice position. When the static Debye-Waller factor is applied to the structure factor of the crystal, it reduces the reflectivity, consistent with the notion that the atoms have a distribution spread about the ideal lattice positions. The distribution is assumed to be Gaussian. In addition, the static Debye-Waller factor is substituted for the coherent fraction in equation [3.1.7]. This gives an internally self-consistent model of reflection and the modulation in the fluorescence signal. In this thesis, it is assumed that the static Debye-Waller factor is the same for all the ions in the crystal structure. In the future, experiments that measure the static Debye-Waller factor in each of the atomic sub-lattices could give further insight into the details of the crystalline lattice.

3.3 Dynamical Diffraction from Thin Slabs

3.3.1 Introduction

In the traditional XSW measurement, the total E-field intensity from the interference between the incident plane waves and the strongly diffracted outgoing waves is simulated in order to properly fit the experimental data. In a thin-film XSW experiment, the intensity of the XSW field needs to be calculated throughout the thickness of the film.

Therefore, it is necessary to have a method to calculate this quantity at any point in the film.

In the 1960s, Takagi [7] and Taupin [8] independently developed a theory for diffraction from crystals under strain perpendicular to the surface. Realizing that this theory could be generalized for crystals that have different reflection properties at different depths, Bartels applied the work to multilayers and superlattices [9]. Bartels' extension applies to the reflected amplitude ratio, and this section will follow his discussion and the further developments derived by Lee [10].

3.3.2 The Takagi-Taupin Equations

Takagi and Taupin developed a generalized theory of diffraction in the 1960s [7,8], the main component being the description of the incident and diffracted plane waves as a pair of first-order differential equations. Taupin showed that these equations could be combined to give a single differential equation for the "modified" D-field amplitude ratio at the top surface of a thin isolated slab of diffracting material. This is described by

$$-i \frac{d\chi}{dT} = \chi^2 - 2\eta\chi + 1. \quad [3.3.1]$$

Note that $\chi(t,z,\theta)$ is not strictly the D-field amplitude ratio $X=D_H/D_O$. Instead it is defined by the following relation,

$$\chi = \left(\frac{F_H}{F_H} \right)^2 \left| \frac{\gamma_H}{\gamma_O} \right|^2 \frac{D_H}{D_O}, \quad [3.3.2]$$

using

$$\psi_H = \sqrt{|b|} \left(\frac{F_H}{F_H} \right)^{\frac{1}{2}} \quad [3.3.3]$$

and $b = \gamma_O/\gamma_H$, where γ_O and γ_H are the direction cosines of the incident and diffracted beams,

$$X = \psi_H \chi. \quad [3.3.4]$$

Note that

$$\psi_H = \psi_H^{-1}. \quad [3.3.5]$$

This leaves two more quantities to be defined. The first is the normalized angle parameter familiar from diffraction [11],

$$\eta = \frac{-b(\theta - \theta_B) \sin 2\theta_B - \frac{1}{2} \Gamma F_O (1 - b)}{|b|^{\frac{1}{2}} \Gamma (F_H F_H)^{\frac{1}{2}}}. \quad [3.3.6]$$

The final quantity is a function of the thickness of the film, t , and the structure factor,

$$T = \frac{\pi \Gamma (F_H F_H)^{\frac{1}{2}} t}{\lambda |\gamma_O \gamma_H|^{\frac{1}{2}}}, \quad [3.3.7]$$

and is a measure of the diffracting strength of the film.

If the composition of the film is uniform, then η is not a function of t , and equation [3.3.1] can be solved via direct integration to get

[3.3.8]

$$\chi_t = \eta + \sqrt{\eta^2 - 1} \frac{(\chi_b - \eta) \cos \alpha - i \sqrt{\eta^2 - 1} \sin \alpha}{-i(\chi_b - \eta) \sin \alpha + \sqrt{\eta^2 - 1} \cos \alpha} ,$$

with

$$\alpha = T(\eta^2 - 1)^{\frac{1}{2}} . \quad [3.3.9]$$

Thus, in a uniform slab, given the modified reflectivity amplitude ratio χ_b at one point, the ratio χ_t can be calculated at a position a distance t above that point inside the slab. One result of interest that can be calculated immediately is the reflected amplitude ratio from an isolated thin slab. Since there is no diffracting material beneath the slab, χ_b is equal to zero. In this case, equation [3.3.8] reduces to

[3.3.10]

$$\chi_t = \frac{i \sin \alpha}{Q} ,$$

where

$$Q = (\eta^2 - 1)^{\frac{1}{2}} \cos \alpha + i \eta \sin \alpha . \quad [3.3.11]$$

As we are dealing with a homogeneous structure, $X_t = \psi_H \chi_t$ for the thin isolated slab.

3.3.3 Recursion Formulae for the Reflected Amplitude Ratio

The solution of the Takagi-Taupin equations can be recast with the examination of Figure 3.3.1, which is a comparison of the two cases of an isolated slab with a semi-infinite crystal and a substrate with an epitaxial thin film. In the first case, we have an isolated thin slab. It has a reflected amplitude ratio of X_{HR} and a transmitted amplitude ratio of

X_{HT} . In addition, we have a semi-infinite crystal that has a reflected amplitude ratio of X_b . When the two crystals are combined to form a substrate with an epitaxial layer, the transmitted beam from the thin film plays the role of the incident beam on the substrate. In the second case, the quantities X_h , D_{Hb} and D_{Ob} can be expressed in terms of X_{HR} , X_{HT} and X_b :

$$X_h = X_{HR} + D_{Hb} X_{HT} , \quad [3.3.12]$$

$$D_{Ob} = X_{HT} + D_{Hb} X_{HR} , \quad [3.3.13]$$

$$D_{Hb} = D_{Ob} X_b . \quad [3.3.14]$$

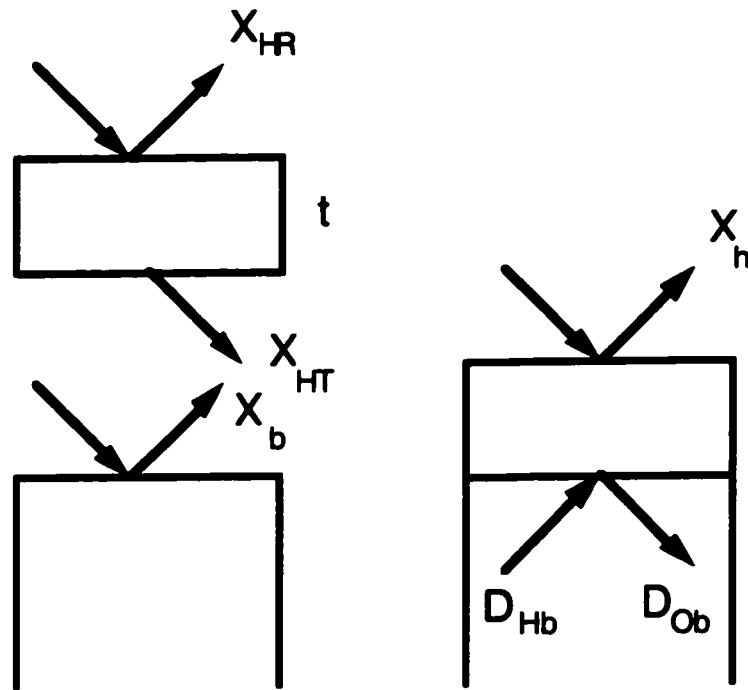


Figure 3.3.1 Reflected and transmitted amplitude ratios from a thin slab. Shown are ratios from an isolated thin slab, a substrate, and a substrate with an epitaxial layer.

Elimination of D_{Ob} and D_{Hb} results in

$$X_h = \frac{X_{HR} - X_b(X_{HR}X_{HR} - X_{HT}X_{HT})}{1 - X_bX_{HR}}. \quad [3.3.15]$$

Here some substitutions can be made. The term X_{HR} , the reflected amplitude ratio from an isolated thin film, was solved in the previous section and can be expressed as

$$X_{HR} = \psi_{Hf}\chi_{HR}. \quad [3.3.16]$$

Using this and equation [3.3.5], the reflected amplitude ratio can be recast as

$$X_h = \frac{\psi_{Hf}\chi_{HR} - X_b(\chi_{HR}^2 - X_{HT}X_{HT})}{1 - X_b\psi_{Hf}^{-1}\chi_{HR}}. \quad [3.3.17]$$

Note that X_h does not take the simple form $X_h = \psi_{Hf}\chi_H$. To properly calculate the reflected amplitude ratio through a varying crystal structure, X_b needs to be calculated for the substrate crystal, and then X_h needs to be calculated at each interface, with X_h from the previous interface replacing X_b at each iteration.

All that remains is the calculation of the transmitted amplitude ratio from the bottom of an isolated slab, X_{HT} . To derive this quantity, assume a virtual slab on top of a substrate. In other words, take a semi-infinite crystal and treat the top few layers as a slab grown perfectly on the crystal. As the diffracting materials are the same, $X_{HR} = \psi_H\chi_{HR}$, and equation [3.3.8] can be utilized to give

$$X_h = \psi_H \left[\eta + \sqrt{\eta^2 - 1} \frac{(X_b\psi_H^{-1} - \eta)\cos\alpha - i\sqrt{\eta^2 - 1}\sin\alpha}{-i(X_b\psi_H^{-1} - \eta)\sin\alpha + \sqrt{\eta^2 - 1}\cos\alpha} \right]. \quad [3.3.18]$$

Using equation [3.3.10],

$$X_h = \psi_H \left[\eta + \sqrt{\eta^2 - 1} \frac{(X_b \psi_H^{-1} - \eta) \cos \alpha - i \sqrt{\eta^2 - 1} \sin \alpha}{Q(1 - X_b \psi_H^{-1} \chi_{HR})} \right], \quad [3.3.19]$$

$$X_h = \psi_H \left[\frac{\chi_{HR} - X_b(2\eta \psi_H^{-1} \chi_{HR} - \psi_H^{-1})}{1 - X_b \psi_H^{-1} \chi_{HR}} \right], \quad [3.3.20]$$

which in turn reduces to

$$X_h = \frac{X_{HR} - X_b(2\eta \chi_{HR} - 1)}{1 - X_b X_{HR}}. \quad [3.3.21]$$

When this expression is compared to equation [3.3.15], it is discovered that

$$X_{HT} X_{HT} = \chi_{HR}^2 - 2\eta \chi_{HR} + 1 = \frac{\eta^2 - 1}{Q^2}, \quad [3.3.22]$$

hence,

$$X_{HT} = \frac{\sqrt{\eta^2 - 1}}{Q}, \quad [3.3.23]$$

which is in agreement with Bonse & Graeff [12]. More importantly, a parallel argument can be made by replacing ψ_H with ψ_{Hf} (replacing the slab of similar material with a slab of different material) in order to arrive at an equation for X_h in a thin film:

$$X_h = \psi_{Hf} \left[\eta + \sqrt{\eta^2 - 1} \frac{(X_b \psi_{Hf}^{-1} - \eta) \cos \alpha - i \sqrt{\eta^2 - 1} \sin \alpha}{-i(X_b \psi_{Hf}^{-1} - \eta) \sin \alpha + \sqrt{\eta^2 - 1} \cos \alpha} \right]. \quad [3.3.24]$$

3.3.4 Total Amplitude

Up to this point, this chapter has concentrated mainly on calculations of the reflected amplitude ratio at an arbitrary point in the thin film, in other words, the relationship between the incident plane waves and the diffracted plane waves at a given depth. However, the quantity that is needed for thin-film XSW is more than just the ratio between those quantities. The total intensity for each position needs to be calculated. For example, consider the case of a heterolayer structure consisting of a substrate, a thin strongly diffracting film, and a very thick weakly diffracting single crystal top layer. While the reflected amplitude ratio of the strongly diffracting layer might be much larger than that of the top layer, if the x-ray beam has suffered from significant attenuation upon reaching the strongly diffracting layer, then the top layer could dominate the XSW data. Therefore, not only is the ratio between the incident and diffracted beams needed, but also the incident amplitude.

Referring back to Figure 3.3.1, the quantity in question is D_{Ob} , which is defined by equation [3.3.13]. This time, solving the three relations for D_{Ob} , the following result is obtained:

$$D_{Ob} = \frac{X_{HT}}{1 - X_b X_{HR}} = \frac{X_{HT}}{1 - X_b \psi_{Hr}^{-1} \chi_{HR}}. \quad [3.3.25]$$

The attenuation of the incident beam is usually described with the absorption coefficient μ . For a film of thickness t , at a height h above the interface, the coefficient can be expressed as

$$\mu(t, h, \theta) = -\frac{1}{t-h} \ln |D_{\text{ob}}|^2 = -\frac{1}{t-h} \ln \left| \frac{X_{\text{HT}}}{1 - X_{\text{b}} \psi_{\text{HR}}^{-1} \chi_{\text{HR}}} \right|^2. \quad [3.3.26]$$

3.4 The Evanescent-Wave Emission Effect for Probing Thin Films

Most of the XSW measurements performed for the thin-film work in this dissertation took place at an incident beam energy of 13.5 keV, which allowed for the observation of the Pb L α fluorescence signal from the ferroelectric thin films. However, the XSW measurement of the Ti K α fluorescence can be more sensitive to the film's polarization. Figure 3.4.1 shows the Pb and Ti fluorescence for both the up and down film orientations. However, the

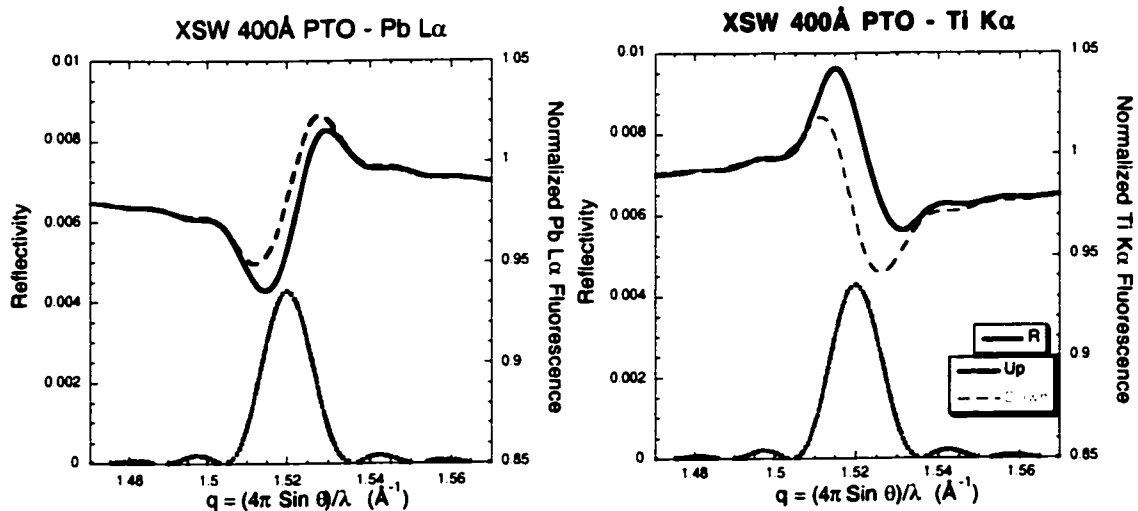


Figure 3.4.1 Theoretical XSW results using Pb L α and Ti K α as the observed fluorescence signal while scanning through the (001) Bragg reflection (R) of a 400 Å thick PTO film. The difference between the up and down film orientations is more drastic in the case of the Ti fluorescence. The Pb simulation is at 13.5 keV and the Ti at 8.0 keV.

Ti signal from the film is difficult to measure because of the presence of Ti in the SrTiO_3 substrate. In order to isolate the film Ti signal from the substrate Ti signal, a surface-sensitive method must be employed. The evanescent-wave effect is utilized to separate the signal of the film from the bulk signal.

The evanescent-wave effect was demonstrated by Becker *et al.* [13] and was applied to XSW experiments by Lee *et al.* [14]. As emitted x-rays leave the crystal, they are refracted at the surface. If the takeoff angle is below the critical angle for total external reflection, then the real part of the internal angle is zero, and radiation from deep in the crystal cannot escape. However, a small region near the surface does contribute to emission. To analyze the fluorescence yield from the crystal below the critical angle, Becker used the principle of microscopic reversibility to recast the problem. Reversing the direction of time, the problem becomes a familiar one from optics, that of total internal reflection. In Figure 3.4.2 two experimental cases are diagrammed. The first has an incident x-ray impinging on a crystal at an oblique angle. The fluorescence that is collected by the detector is below the critical angle. This corresponds to the evanescent-wave emission case. The second case has an x-ray striking the crystal at below the critical angle, generating

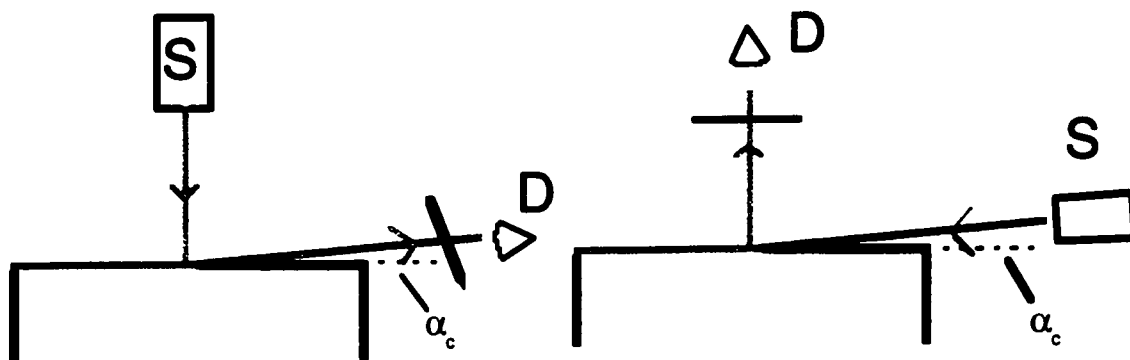


Figure 3.4.2 Two experiments, illustrating the evanescent-wave effect. The first has x-rays incident on a sample, and the fluorescence is being observed at below the critical angle by the detector. In the second, the x-rays strike the crystal at below the critical angle and undergo total external reflection.

fluorescence. If the incident x-ray in the second case is the same energy as the emitted x-rays in the first case, then by time reversal, the results concerning the two cases are the same. As the emission case is not trivial, it is easier to treat the problem from the other direction, as total external reflection.

Total internal reflection is a familiar optics problem for visible wavelengths [15]. In the case of x-ray frequencies, since the frequency of the incident x-ray exceeds the frequency associated with the binding of the electrons in the crystal, the index of refraction of the crystal is slightly smaller than unity, and hence the crystal is optically less dense than air. An x-ray coming from air to the crystal will be refracted into a smaller angle. Below the critical angle, total external reflection will take place. Total external reflection and total internal reflection are the same phenomena; the naming difference arises from the fact that in the x-ray case, the fields do not propagate into the crystal; hence, external reflection. The incident wave creates a refracted wave that travels along the boundary and an exponentially damped transmitted wave that penetrates into the crystal. The intensity of the field inside the crystal can then be described as

$$I_{\text{out}}(\alpha, z) \propto I_s(\alpha) e^{-\mu(\alpha)z}, \quad [3.4.1]$$

where I_s is the E-field intensity at the surface of the crystal. The field at the surface can be determined from Fresnel theory [16],

$$I_s = 4 \left[1 + \frac{|\xi(\alpha)|^2}{\sin^2 \alpha} + \frac{2 \operatorname{Re}(\xi(\alpha))}{\sin \alpha} \right]^{-1}, \quad [3.4.2]$$

where

$$\xi(\alpha) = \sqrt{\sin^2(\alpha) - 2(\delta + i\beta)}. \quad [3.4.3]$$

The exponential decay of the evanescent field inside the crystal can be described by

$$\mu(\alpha) = \frac{4\pi}{\sqrt{2}\lambda_2} \left\{ [(2\delta - \alpha^2)^2 + 4\beta^2]^{1/2} + 2\delta - \alpha^2 \right\}^{1/2},$$

where β and δ are related to the index of refraction by $n = 1 - \delta - i\beta$. Figure 3.4.3 plots the surface intensity, escape depth and I_{out} for PTO at a low angle.

From Snell's law, the critical angle is defined as $\sqrt{2\delta}$, which is 0.66° in the case of Ti $K\alpha$ photons escaping from PTO. In the region of the critical angle, the escape depth, μ^{-1} , drops rapidly to its minimum of 18 \AA . To control the takeoff angle, a motorized slit is used.

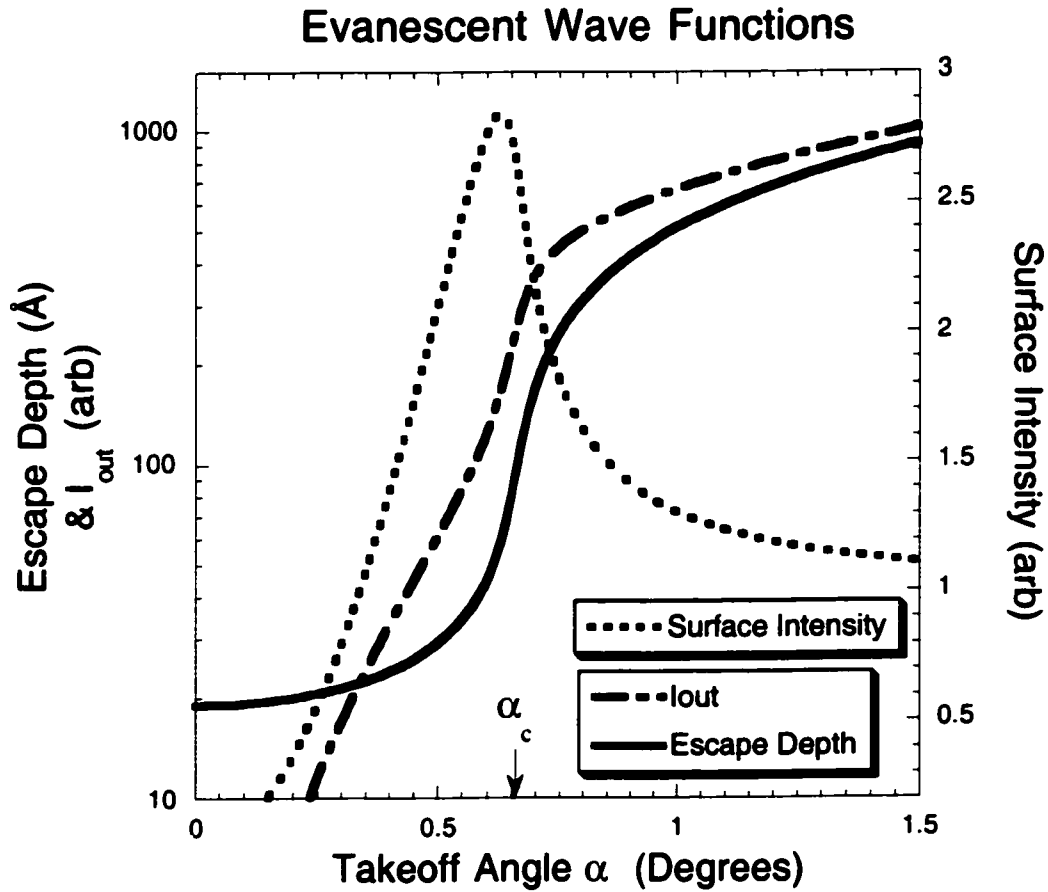


Figure 3.4.3 Evanescent-wave effect near the critical angle, Ti $K\alpha$ photons with an energy of 4.51 keV emitted from PTO. Three quantities are displayed. The surface intensity peaks near the critical angle, then drops. The escape depth quickly drops to its final value of 18 \AA . The quantity I_{out} is given as the product of surface intensity and escape depth.

This will eliminate fluorescence from the substrate, leaving fluorescence from the Ti ions in the film. Note that for the evanescent-wave effect to work, a reasonably sharp interface (roughness $\sigma < 10 \text{ \AA}$) is required.

3.5 Crystal Truncation Rod Measurements

In 1988, Ian Robinson and coworkers demonstrated that careful measurements of the interference between the crystal truncation rod (CTR) of a substrate and the diffraction pattern from a thin film could be used to describe the details of the interface [17]. In this method, the reflected amplitude from the substrate is calculated separately from the reflected amplitude of the thin film. The amplitudes are summed at the level of fields, with one of the terms multiplied by a phase factor to account for the interface separation. Carol Thompson and coworkers applied this technique to thin films of PbTiO_3 [18]; the data analysis software used for the CTR studies in this dissertation is based upon her paper.

The program, written in MATLAB, generates amplitude reflectivity (E/E_0) independently for both the substrate and the film. The structure factor for the substrate is calculated as a function of q at the start of the program and is not modified by any of the fitting parameters. The atomic form factors are a function of q and are generated from linear fits performed by Waasmaier & Kirfel [19]. The structure factor for the film is dependent upon the fitting parameters of the program, and hence needs to be generated at each iteration.

Reflected amplitude from the substrate is calculated using the semi-infinite crystal kinematical expression,

[3.5.1]

$$R = \frac{i4\pi r_e}{a^2 q} F_{sub}(q) \{1 - \exp[-a(iq + \epsilon_{sub} q^{-1})]\}^{-1},$$

where r_e is the classical radius of the electron, a is the lattice parameter of the substrate, and ϵ is related to the linear absorption coefficient (μ) by $\epsilon = 4\pi\mu/\lambda$. Hence, the ϵ term accounts for absorption. This expression is corrected for extinction by the equation [3.5.2]

$$R_{SUB} = \frac{2R}{\left\{1 + \left[1 + (2R)^2\right]^{1/2}\right\}}.$$

Before this term is added to the reflectivity term corresponding to the film, it is multiplied by an exponential damping factor,

$$D_{Sub} = \exp\left[-\frac{1}{2}\sigma_s^2(q - q_{001})^2\right], \quad [3.5.3]$$

to account for roughness at the film/substrate interface.

Reflectivity from the film is calculated using the following kinematical formula for a finite-thickness crystal,

$$R_{FILM} = \frac{i4\pi r_e}{a^2 q} F_{FILM}(q) \frac{1 - \exp[-cN(iq + \epsilon_{film}q^{-1})]}{1 - \exp[-c(iq + \epsilon_{film}q^{-1})]}, \quad [3.5.4]$$

where a and c are lattice parameters of the film and N is the thickness of the film measured in layers of unit cells. To account for roughness, the reflectivity of the film is modified by an exponential factor D_{Film} , which is similar in form to D_{Sub} .

The contributions of the substrate and film are summed, with a phase factor accounting for the interface separation between the two, giving a total amplitude reflectivity of

$$R_{Total} = R_{Sub} D_{Sub} + R_{Film} D_{Film} \exp[-c(N + \delta)(iq + \epsilon q^{-1})], \quad [3.5.5]$$

where δ measures the separation between substrate and film as a fraction of a film unit cell.

Finally, the possible variation in film thickness was fitted by applying a Gaussian distribution to the thickness. A weighted sum dictated by the mean number of layers and the standard deviation in the number of layers is used to generate a theory curve. This sum

ranges over the mean thickness, plus and minus five unit cells. As this sum is truncated, a large standard deviation implies a near-uniform distribution in the number of layers about the mean rather than a large spread about the mean.

The variables that are fitted by the program are σ_f (film roughness), σ_s (substrate roughness), δ , c , N_{mean} , N_{sigma} , and an overall scaling factor. The fraction of the film that is in the up orientation is held as a constant during each fit. MATLAB's minimization routines are used to perform a least-squares fit upon the data.

The program is executed from the GUI.M routine, written in MATLAB for analyzing data for this thesis (see Appendix A). Here the user can enter starting values for the variables and either "probe" to perform a zero-iteration fit, graph it against the data, and return a Chi-squared difference, or "fit" to perform a Chi-squared fit.

Chapter 4 - Experimental Setup

4.1 Optics and Detectors for X-ray Measurements

The XSW experiments were conducted at the 5ID-C undulator beamline at DND-CAT and the 12ID-D undulator beamline at BESSRC-CAT, both at the Advanced Photon Source. For the experiments in this dissertation, the experimental setups used at these beamlines can be considered to be identical. A schematic of the beamline is presented in Figure 4.1.1. The thin-film XSW experiments placed a pair of demands on the experimental setup. A small beamsize was needed in order to examine regions measuring hundreds of microns in each direction, and in order to properly characterize a small modulation in the fluorescence yield, on the order of 10^6 counts were needed at each step in angle. Given these constraints, it was necessary to use an undulator beamline for the thin-film XSW measurements in order collect data in a reasonable amount of time.

A high heat load liquid nitrogen-cooled Si(111) double-crystal monochromator is the first optical element downstream from the undulator. Higher-order harmonics can be rejected from the spectrum by tuning the second crystal relative to the first. Typically, the monochromator is detuned to about 80% intensity on the low-angle side of the Si (111) reflection. From the high heat load monochromator, the beam travels down an evacuated beampipe into the experimental hutch. In the hutches at the two beamlines, additional optical elements are used to condition the beam (Fig. 4.1.2); these elements sit on an optical table that features X-Y-Z motion. Small adjustments in theta and chi can be made by adjusting the three different Z stages supporting the kinematical table. In addition, each element also has X-Z motion independent of the table. All of these

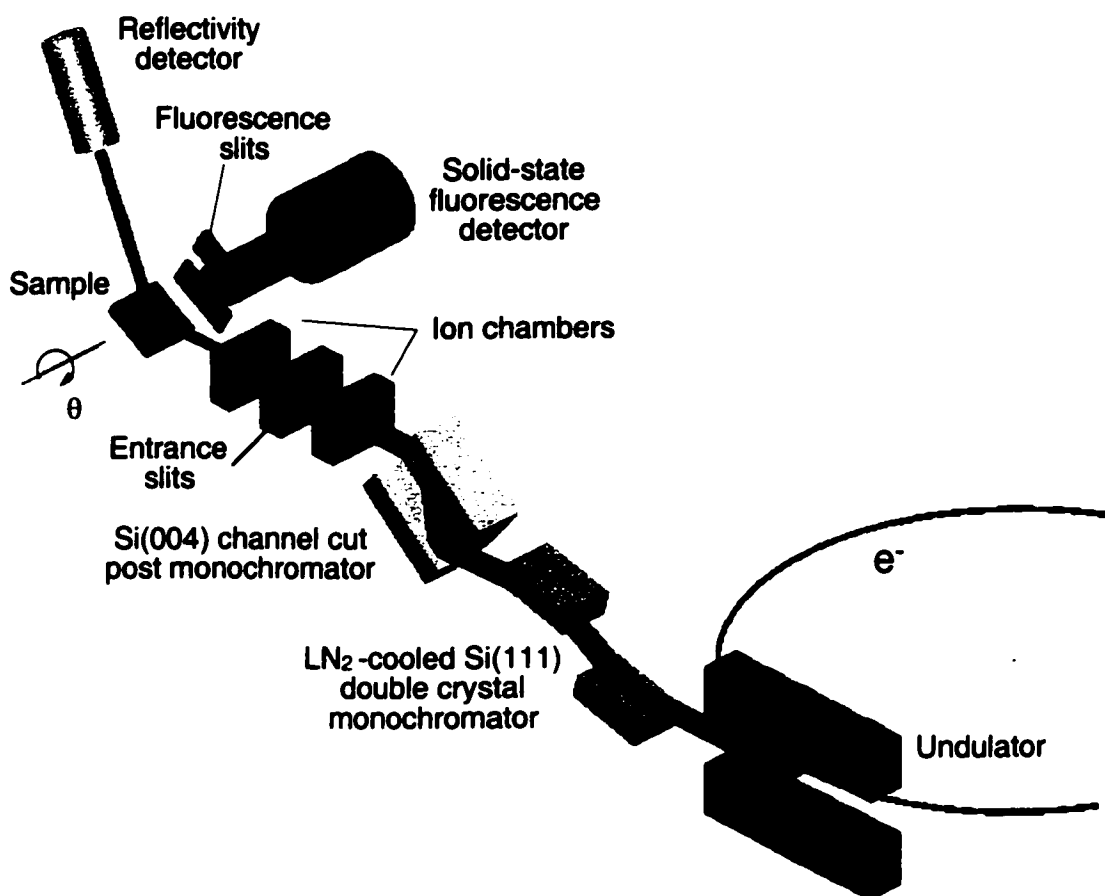


Figure 4.1.1 Setup of an XSW experiment at an undulator beamline at the Advanced Photon Source. Synchrotron radiation is produced as the electron bunches travel through the magnets of the undulator. The radiation generated in each oscillation of the beam in the undulator interferes constructively, creating peaks in the undulator x-ray spectrum. The undulator x-ray beam is then energy-selected by a high heat load Si(111) monochromator, and further conditioned by downstream optics [a single Si(004) channel-cut crystal is shown in this diagram]. The intensity of the beam is monitored by ion chambers, and the size is controlled by a pair of entrance slits. The beam strikes the sample, and the reflected intensity and fluorescence are monitored by detectors as the sample is scanned in angle through its Bragg diffraction rocking curve.

motions are driven by computer-controlled stepper motors so movements can be performed while there is beam in the hutch.

The intensity of the beam as it enters the hutch is monitored by an ion chamber, IC1. The beam is reflected off a pair of Si channel-cut crystals, PM1 and PM2. Using the initial ion chamber and ion chambers between and after the paired channel-cut crystals, IC2 and IC3, the angular width of the beam can be fine-tuned by a feedback mechanism

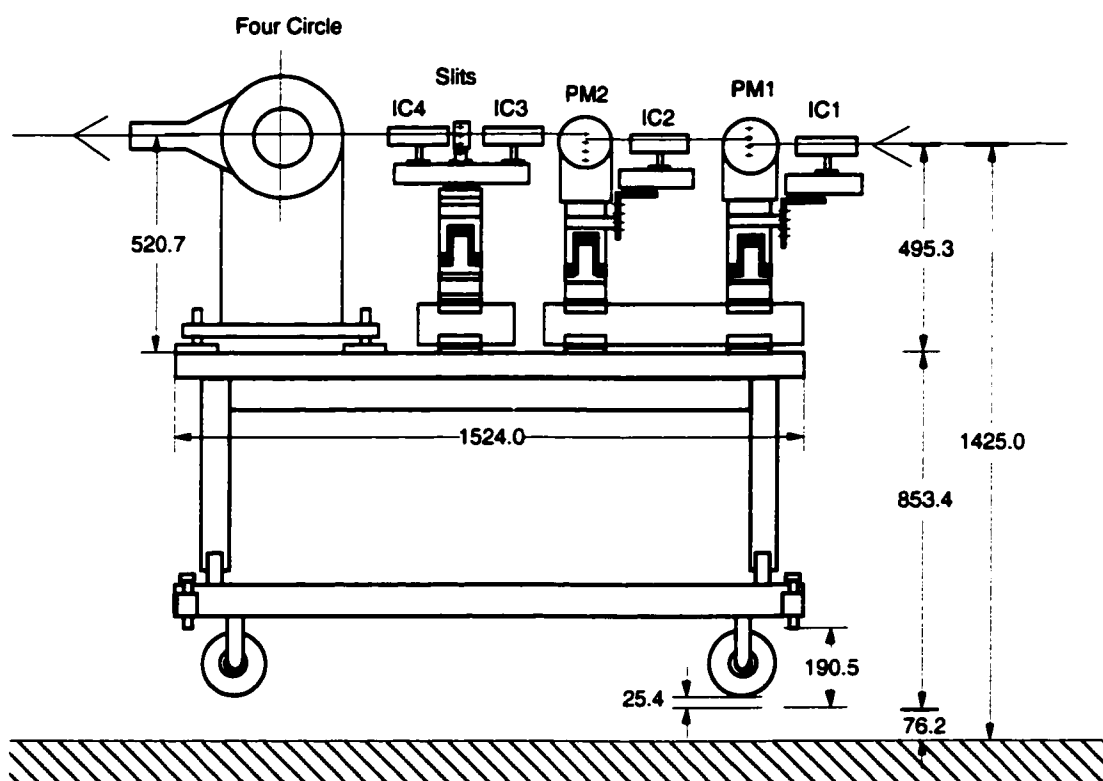


Figure 4.1.2 Side-view of the post-mono table. This motorized optical table allows for the diffractometer and all of the x-ray optics to be moved in X, Z, chi and theta with respect to the beam. Shown here, right-to-left (the direction of the beam) are the elements used to condition and characterize the beam from the high heat load monochromator: two stages that hold ion chambers and channel-cut monochromator crystals, a stage that has ion chambers and a defining slit, and a four-circle monochromator. The channel-cut and slit stages can move in X and Z independently of the table motions, and the channel-cut stages have both a microstepped theta motion and a finer piezo drive to properly set the angles for the channel-cut crystals.

controlled by a MOSTAB unit [1]. This feedback loop adjusts the angle of the channel-cut crystal with sub-microradian precision by the use of piezo transducers and a torsion-bearing stage. The transducers are Physik Instrument model P840.20 and are controlled by a Physik Instrument P864.10 driver/amplifier and a Physik Instrument E-808 controller. The feedback allows adjustment of the angular width of the reflection from the channel cut crystals, and the contribution of higher-order harmonics can again be reduced. See Figure 4.1.3 for a DuMond diagram for the x-ray optics. The channel cuts are mounted on piezo-torsion-bearing stages mounted on Huber 410 rotation stages. The

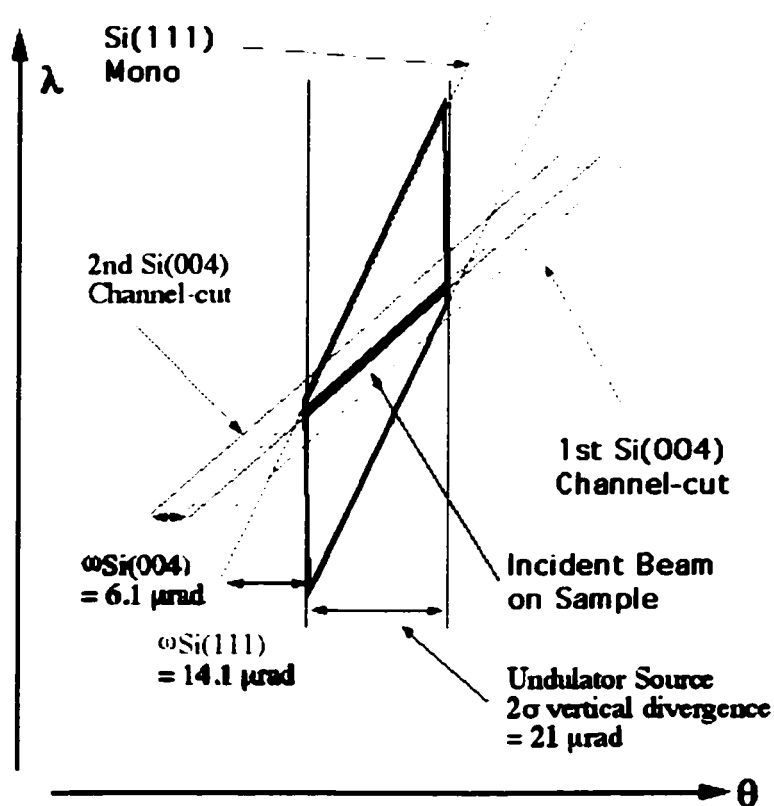


Figure 4.1.3 λ vs. θ DuMond diagram for the x-ray optics at the APS undulator beamlines at 18.5 keV. Shown are the angular divergence from the undulator, the Si(111) reflection from the LN₂-cooled high heat load monochromator, the Si(004) reflection from the first channel cut and the Si(004) reflection from the second channel cut, detuned to 25%.

Huber rotation stages are mounted to translation stages that allow them to move in the X and Z directions. By moving the Huber stages in the X direction, different channel cuts can be moved in and out of the beam. This allows for remote rapid switching of the in-hutch monochromator between the Si(004), Si(111) and Si(022) channel cut crystals. This is useful, as due to dispersion, one always wants to closely match the d-spacing of the channel cuts to the d-spacing of the sample. After the channel-cut crystals, the beam is defined in size by a slit, and its intensity is measured by an ion chamber, IC4. This ion chamber is used as a monitor for normalization purposes.

For the thin-film XSW measurements the paired channel-cut crystals were not utilized. Since the Bragg peak from the thin film had a much larger angular width in comparison to the peak from the beamline optics, no further conditioning was necessary. The thin-film experiments were performed in open air on four-circle diffractometers. The sample stages on the diffractometers have motorized X-Y-Z motions to aid in sample alignment. A reflectivity detector was mounted on the two-theta arm of the diffractometer to monitor the scan through the Bragg reflection, and an energy-dispersive fluorescence detector was used to observe the spectrum from the sample. The output of the fluorescence detector was sent to both the data-collection software and to a cascade of single channel analyzers (SCAs). The SCAs allowed us to monitor fluorescence signals in real time, a feature that greatly facilitated alignment. In experiments where Ti fluorescence was measured, a slit was mounted between the sample and the fluorescence detector in order to define the takeoff angle. The SPEC software package with in-house macros written by Tien-Lin Lee was used to control and record the XSW experiments.

4.2 Ultra High Vacuum Chamber

The Sr/Si(001) samples examined in this dissertation were grown and measured in an ultra high vacuum (UHV) chamber located at the 12ID-D undulator beamline at BESSRC-CAT at the APS. This chamber has a base pressure of better than 1×10^{-10} Torr. A schematic diagram is given in Figure 4.2.1. The central chamber is an R2-P2 design from Vacuum Generators LTD. This chamber has a sample manipulator that can access ports arranged in a radial fashion. Connected to the R2-P2 system are a load-lock chamber, a sample storage area, a surface science analysis area, a growth chamber and an x-ray chamber. The vacuum in the R2-P2 chamber is maintained by a 400 liter/sec ion pump and a titanium sublimation pump. The entire 1700 pound UHV system is supported by a frame that rests on three z-motion translation stages. Using stepper motors, the chamber has a range of 80 mm in the X direction (horizontal motion in the plane perpendicular to the beam) and 100 mm in the Z direction. Due to the kinematical mounts of the Z-motion stages, the entire chamber can perform a small rotation about the theta axis in the x-ray chamber; this is the mechanism used for rocking curve scans. Steps as small as 2×10^{-5} degrees in theta can be achieved.

Up to six samples at a time may be introduced into the vacuum chamber via a load-lock system. The pressure in the main chamber rises into the 10^{-9} torr range for several minutes after sample introduction. There is space in the other two chambers to protect two samples behind isolation gate valves if the samples have surfaces sensitive to this pressure. Inside the main chamber, there is a carousel that allows for the storage of up to six samples; reducing the number of times the load-lock needs to be operated.

Multi-Chamber UHV System at APS/12ID-D

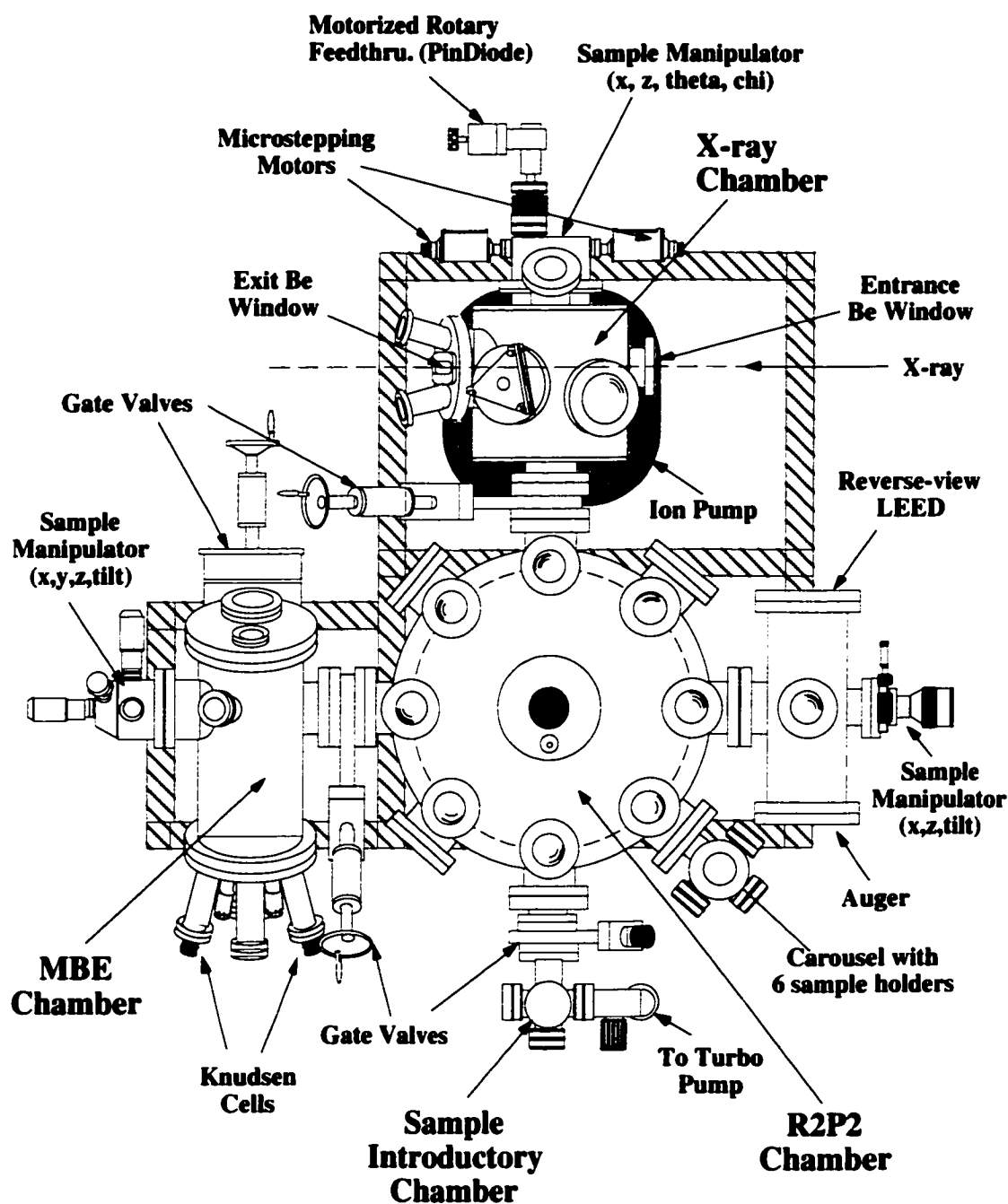


Figure 4.2.1 Top view of the UHV system at the BESSRC 12ID-D undulator beamline.

These features allow for continual UHV conditions inside the chamber, with no need to vent to atmosphere except for repair.

The growth chamber features a Perkin-Elmer 10-320 sample manipulator that can move in X,Y,Z and chi. The manipulator is also equipped with a heater filament that can heat samples to over 1000° C (see Fig. 4.2.2). There is a thermocouple for temperature measurement, but as it is not located directly on the sample, in practice a better value is obtained by an optical pyrometer. The range of motion of the manipulator allows it to be

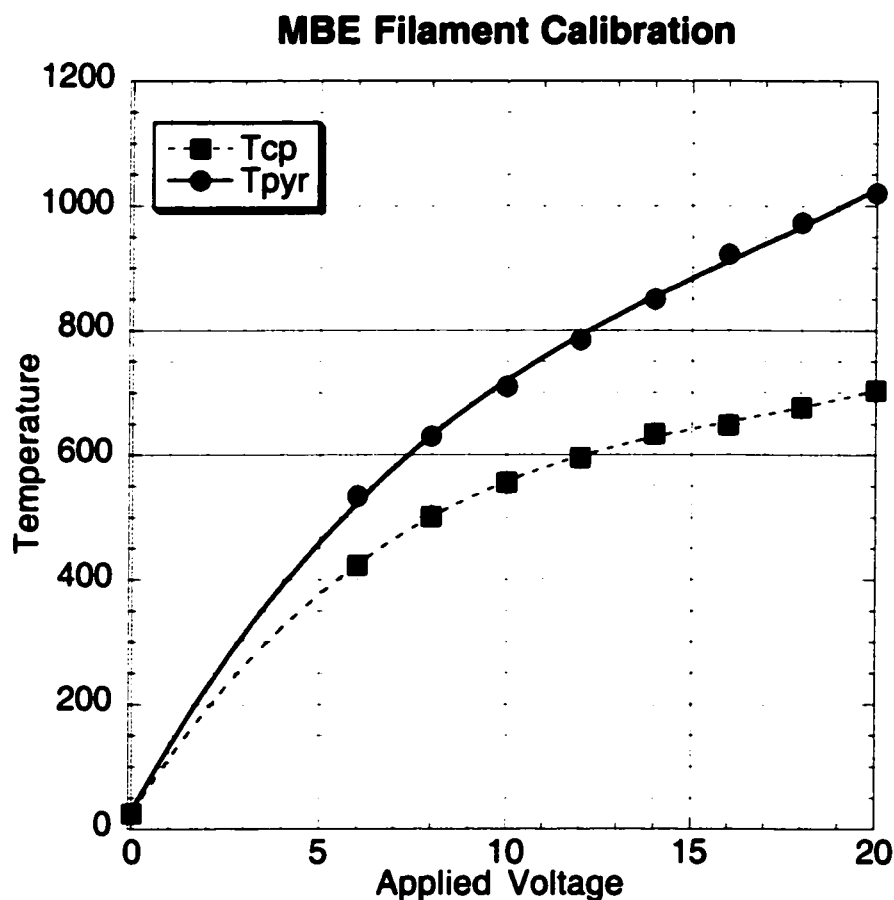


Figure 4.2.2 Filament calibration for the heater in the MBE chamber. Temperature was measured with both a built-in thermocouple T_{cp} and an optical pyrometer T_{pyr} observing a silicon sample. The emissivity setting on the pyrometer was 0.67.

exposed to a number of sources, including Knudsen cells from Perkin-Elmer and an Omicrom EFM 3T triple e-beam evaporator. A quartz-crystal oscillator can be used to calibrate growth rates from the Knudsen cells. The vacuum in the growth chamber is maintained by a cryopump, except during x-ray scans, when the vibrations from the pump's compressor compromise the rocking curve. At such times, the gate valve to the R2-P2 chamber is left open, and both chambers are evacuated by the ion pump on R2-P2.

The sample LEED-Auger chamber has a Perkin-Elmer 283-8550 sample manipulator capable of X-Z motion, plus a rotation. This allows the sample surface to be analyzed by both reverse-view LEED and a cylindrical mirror analyzer for Auger spectroscopy. The LEED is a Perkin-Elmer PHI RVL 8-120, with a PHI 11-020 controller. The Auger unit is a Perkin-Elmer PHI 10-155, with a Perkin-Elmer PHI 11-

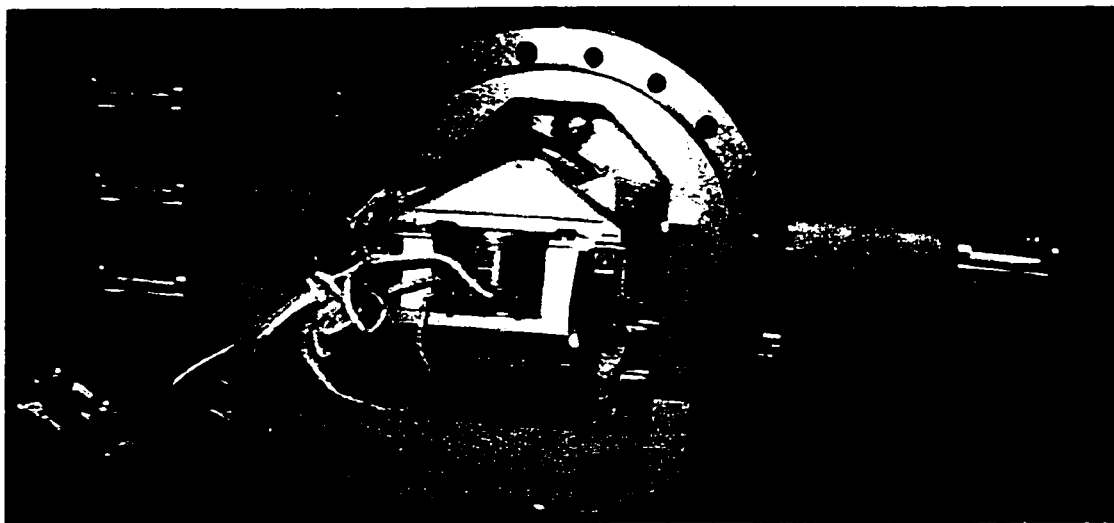
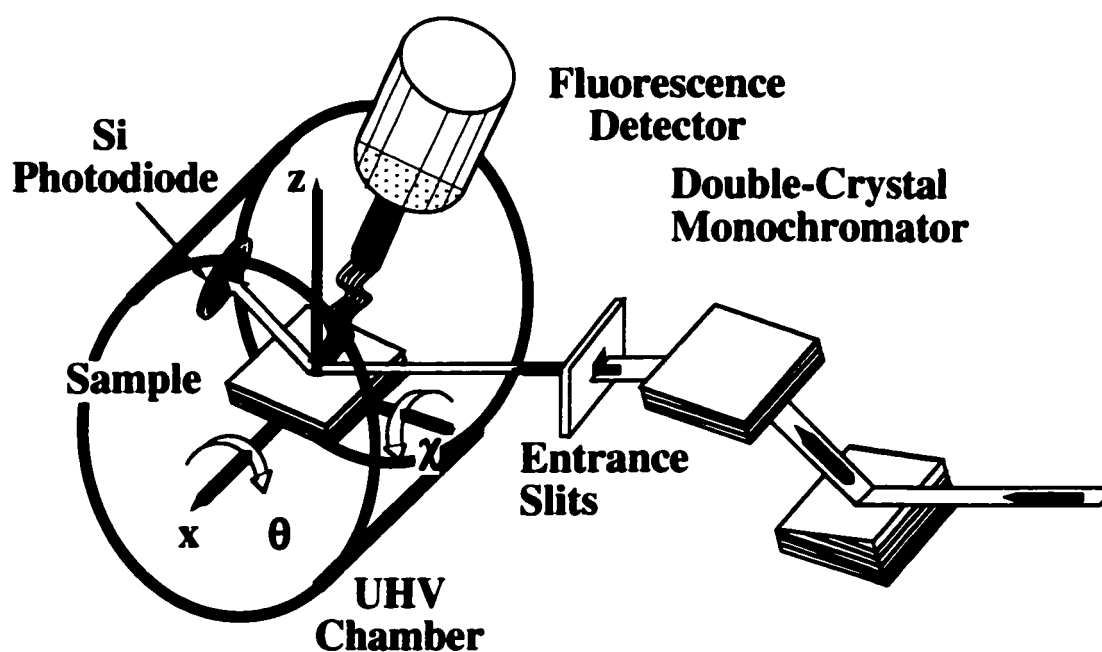


Figure 4.2.3 Sample manipulator from the x-ray chamber (shown removed from UHV chamber). Stepper motors and feedthroughs allow for motion in the X, Z, theta and chi directions for the sample, and two theta for the pin diode used to collect reflected intensity. A filament and thermocouple allow for *in situ* sample heating.

010 electron gun controller and a Perkin-Elmer PHI 11-500A AES system controller. This pair of tools gives information on the crystallographic long-range structure and cleanliness of the surface. Note that this chamber, unlike the others in the system, is not isolated from the main chamber by a gate valve.

The x-ray chamber is separated from the R2-P2 chamber by a gate valve. The vacuum is maintained by a 400 liter/sec ion pump and a titanium sublimation pump. The sample manipulator in the x-ray chamber is a Perkin-Elmer 15-630, which provides for



4.2.4 Geometry for UHV XSW. The white beam is monochromated by a pair of LN₂-cooled Si(111) crystals. A post-monochromator set of channel-cut crystals (not shown here) can be used to get a narrower peak in energy. The beam is then defined by a set of entrance slits and is admitted to the UHV chamber through a Be window. After diffracting from the sample, the reflected intensity is measured by an internal pin diode. An external fluorescence detector monitors secondary radiation through a 10 mil Be window on a snout that extends into the UHV chamber. While the sample has a theta motion, for rocking curve measurements the entire chamber is scanned through theta.

theta and chi motion in addition to X,Y and Z translation. A photograph of the x-ray chamber sample manipulator can be found in Figure 4.2.3. The motions allowed by the sample manipulator, coupled with a pin diode mounted to a two-theta arm, allow for x-ray diffraction measurements to be made. The x-ray beam is reflected through the beamline optics to a 10 mil Be window on the x-ray chamber. For coarse adjustments, the sample theta motion is used to find Bragg reflections, but for actual scans, the entire vacuum chamber is rocked through theta via upstream and downstream Z-motion motors to transverse the rocking curve. A specially built fluorescence detector from PGT is used to collect fluorescence data for XSW measurements. See Figure 4.2.4 for a diagram of the XSW setup in the UHV chamber.

Chapter 5 - XSW Measurements of the Sr/Si(001) Surface Structure

5.1 Background

5.1.1 Introduction

The interest in growing thin films of perovskite materials on Si is driven by possible applications in computer memory and logic devices. Hence, issues of integration with semiconductors are important in the progression of microelectronics technology. One goal along this path that has proven to be difficult is the growth of SrTiO_3 (STO) on Si(001) [1]. In addition to acting as a template for the growth of additional layers of perovskites, the relatively high dielectric constant of STO makes this material an attractive candidate to replace SiO_2 as the gate dielectric in field-effect transistors [2]. STO thin films have also been used as effective compliant buffer layers in the integration of GaAs on Si [3].

The growth of STO(001) on Si(001) should be facilitated by the small lattice mismatch between Si(110) and STO(100), only 1.8% [4]. While there have been several reports of epitaxial STO films grown on Si [5], atomically sharp STO-Si interfaces have only been reported when film growth was initiated by the formation of an ordered Sr/Si(001) surface phase [1]. The atomic-scale details of these interfaces are not well known. Additional knowledge of the Sr/Si(001) system could lead to insight into the surface science involved in growing high-quality epitaxial films of STO on Si(001). A better understanding of alkaline-earth metal / Si surface interactions should also aid in the integration of ferroelectric BaTiO_3 and high T_c superconductors on semiconductors.

5.1.2 Previous Studies of Sr/Si(001)

The first study of the Sr/Si(001) surface was published by Fan and coworkers in 1990 [6]. In their UHV chamber they used Ar^+ -ion bombardment followed by a high-temperature anneal to clean Si(001) surfaces. LEED analysis revealed the well-known (2x1) dimerized surface. A piece of Sr wound in tungsten was used as a deposition source, and the deposition rate was calibrated with a crystal quartz thickness monitor. Sr deposition took place at room temperature, and no long-range ordering could be determined by LEED. However, after a 1 minute anneal to 800°C, LEED patterns were revealed. Fan and coworkers were able to observe (3x2), (2x1), (5x1) and (3x1) phases. The periodicity of the surface structures was coverage dependent, as seen in Figure 5.1.1

Fan *et al.* also noted that the history of the sample had a significant effect on the

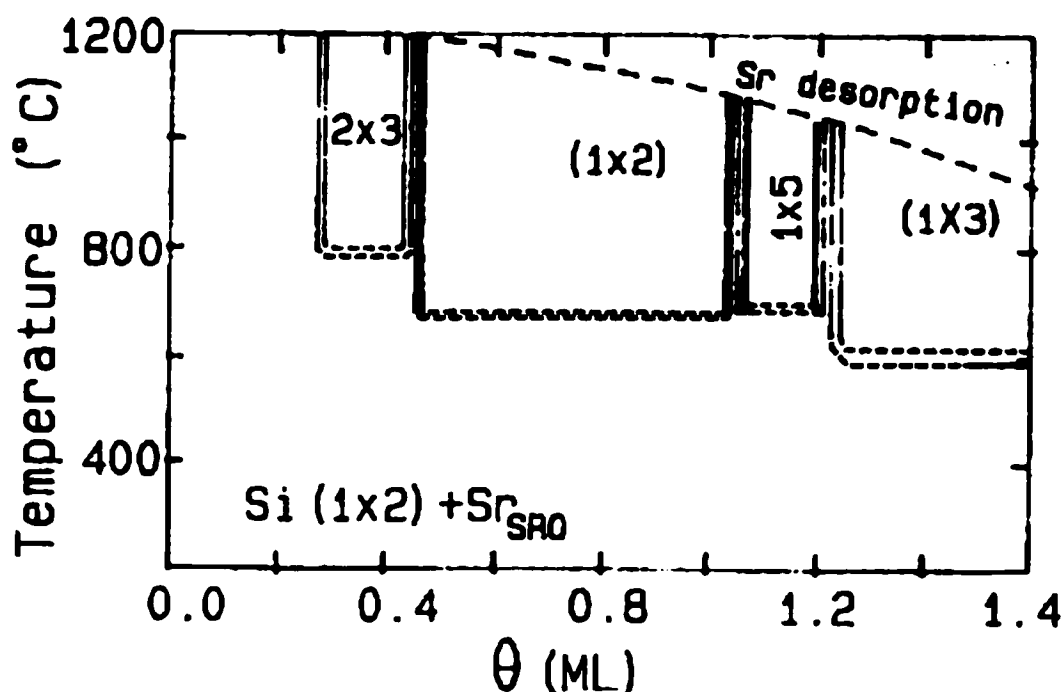


Figure 5.1.1 Phase diagram of the Sr/Si(001) system, and LEED results as a function of deposited coverage and annealing temperature. From Fan *et al.* [6].

growth of well-ordered structures; a Si substrate that had previously undergone Sr deposition and annealing would upon further deposition develop long-range order at an annealing temperature lower than a similar coverage on a virgin sample. They postulated that the initial cycle might serve to break Si dimer bonds and hence create a smoother surface, leading to greater Sr mobility.

LEED-intensity studies were undertaken in order to better understand the different phases. Based on observations of the relative intensity of the one-half and one-third order beams in the low-coverage (0.3 - 0.5 ML) (3x2) phase, it was proposed that the (3x2) pattern is due to the substrate (2x1) phase combined with a (3x1) Sr overlayer. There appeared to be two types of (2x1) ordering, one for low coverage, and one for high coverage. These (2x1) phases were not believed to be due to the Si(001) (2x1) reconstruction.

Fan *et al.* proposed atomic chains of Sr to explain the LEED results. For the (3x2) phase, (3x1) chains perpendicular to the Si(001) (2x1) were suggested. The Sr chains would lie along both the pedestal and valley-bridge sites. These locations are shown in Figure 5.1.2. The low coverage (2x1) reconstruction was also explained by Sr atoms on pedestal and valley-bridge sites, and the high coverage (2x1) by chains of Sr dimers, again occupying the pedestal and valley-bridge sites. The atomic-scale models proposed for reconstructions above 1 ML, the (5x1) and (3x1) surfaces, required decreased spacing between the chains.

In 1995 Bakhtizin and coworkers complemented Fan's LEED work on the Sr/Si(001) system with a LEED and STM study [7,8]. The Si surface was cleaned by a

on Si-(2x1) on Si-(1x1)

Valley Bridge Cave Hollow Bridge

Pedestal Bridge Antibridge On-top

●—● Ad-dimer ⊗ Top layer Si ○ Bulk Si

[110] [110] [001]

Figure 5.1.2 Si(001) surface and possible Sr occupation sites. Fan *et al.* [6] proposed atomic chains of Sr perpendicular to the Si(2x1) dimers on both the pedestal and valley-bridge sites for the (3x2), and both (2x1) reconstructions. Bahktizin [7,8] proposed occupation of the cave sites at 2/3 ML for the (3x2) surface reconstruction, and claimed that at 1 ML the chains ran parallel to the Si dimers. Hu *et al.* [4] claims that the (3x2) reconstruction took place at 1/3 ML rather than Bahktizin's 2/3 ML.

the LEED pattern increased, but the (2x1) reconstruction went unmodified, suggesting that the substrate dimers were unbroken. Low-coverage ($\theta < 0.12$ ML) STM studies showed that the Sr atoms were distributed randomly on the Si(001) surface.

At coverages above 0.12 ML, the Sr atoms formed chains that ran perpendicular to the Si(001) dimer rows, even at room temperature. When the Sr coverage increased to above 0.2 ML, a (3x2) surface reconstruction was observed after a 1 minute anneal to 800°C. From the STM images, Bakhtizin claimed that the (3x2) reconstruction could be explained by a unit cell twice as large as that of unreconstructed Si between the Si dimer rows, and 3 times as large along the rows. Bakhtizin proposed a model with Sr atoms occupying the cave sites between neighboring Si dimers. However Bahktizin stressed that the exact model for (3x2) reconstruction has not been determined. In passing, Bakhtizin noted that for coverages above 1 ML, a (3x1) phase exists, and that in this case the atomic Sr chains were observed to run parallel to the direction of the Si dimers.

Recently, Hu and coworkers studied the Sr/Si(001) surface via LEED and STM [4]. Si(001) samples were cleaned in UHV via a series of high-temperature anneals, and Sr was deposited on the Si(2x1) reconstructed surface at room temperature via a Knudson cell. The method employed was to deposit ~8 ML of Sr and then to anneal at a given temperature to desorb a portion of the Sr. At 8 ML a 12 spot hexagonal pattern was observed, but this disappeared when the sample was annealed above 200° C. No LEED pattern could be observed for coverages between 2.5 and 7 ML, and between 1.5 and 2.5 ML spots were seen on LEED, but no periodicity could be established. At 1.5 ML the (5x1) reconstruction reported by Fan, but not Bahktizin, appeared. However, the high-

coverage (3x1) reconstruction reported by both Fan and Bahktizin went unseen. At lower coverages, the (5x1) pattern was accompanied by some ($n \times 2$) components. The (2x1) reconstruction was observed at 0.5 ML, along with the ($n \times 2$) behavior.

At low coverages (~ 0.3 ML), the (3x2) surface was reported. Hu claims that STM images show that the (3x2) coverage saturates at $1/6$ ML, and promises to provide details in a yet unpublished article. No surface models were proposed to explain the findings of this study.

Hu and coworkers also deposited Sr onto hot Si (500°C) substrates. These results and also the growth of Sr silicides following the work of McKee [1] will not be discussed, as they are outside the scope of the experiments performed in this dissertation. However, these directions should be pursued in future work.

5.2 Sample Preparation

Custom-cut and Syton polished Si(001) single crystals were used as substrates in this experiment. These samples were rinsed with organic solvents and etched following a modified version [9] of the Shiraki etch [10] in order to clean the crystals and protect them with a thin oxide layer. The samples were then mounted in a strain-free manner [11] and introduced to the UHV chamber at the 12-ID-D undulator beamline at BESSRC, described in Chapter 4. The samples and their holders were outgassed at 600°C for 12 hours. Following outgassing, the samples were annealed to 850°C for 10 minutes to clean the surfaces. The expected two-domain Si (2x1) reconstruction was observed.

Auger analysis revealed surface contamination of O and C to be no greater than 0.03 monolayers.

Sr was deposited via a Knudsen cell operating at 350°C on the clean Si(001) samples at room temperature for 10 minutes. Figure 5.2.1 shows the deposition of Sr as a function of time. After deposition, the samples exhibited a diffuse (3x1) LEED pattern. The Sr coverages of the samples were measured by comparing the off-Bragg Sr fluorescence yield to that of a standard measured by RBS. One sample was measured prior to a post-deposition annealing; the coverage was 0.66 ML. See Figure 5.2.2 for the LEED patterns of clean Si(001) and the surface covered with Sr.

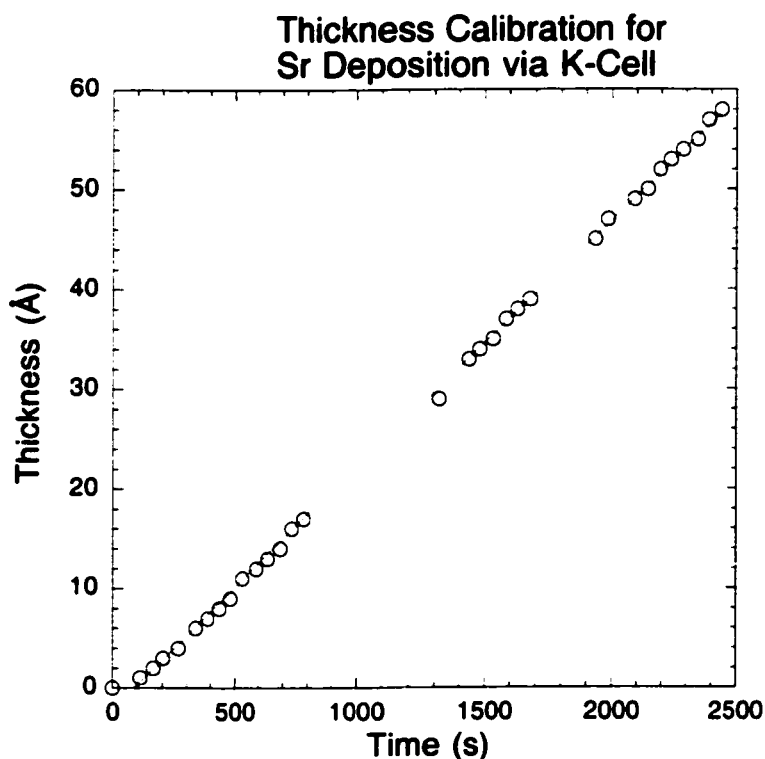


Figure 5.2.1 Thickness of Sr on Si(001) substrate as a function of time, measured by quartz crystal thickness monitor. The K-cell was at 380° C, slightly higher than the deposition temperature of 350° C.

Once a (3x1) reconstruction was observed, various post-deposition anneals were used to partially desorb Sr and create ordered surface phases. By annealing the (3x1) phase, we were able to observe both the (2x1) and (3x2) phases. The temperature was typically raised at roughly 7°C/min and decreased at roughly 27°C/min in the annealing process. The LEED patterns are shown in Figure 5.2.3. A chart in the next section details the deposition time, annealing time and temperature, coverage, LEED pattern and XSW structural details for the samples studied in the two beamtimes devoted to the Sr/Si (001) project. The LEED and XSW data were collected at room temperature.

5.3 Sr/Si(001) XSW Results

X-ray standing wave experiments were performed on sub-monolayer surfaces of Sr grown on Si(001) in November of 2000 and February of 2001 at the 12ID-D BESSRC-CAT undulator beamline. See Figure 4.1.1 for a diagram of the experimental setup.

The experiments were performed at an incident photon energy of 18.5 keV in order to excite Sr K α fluorescence. See Figure 5.3.1 for the measured fluorescence spectrum. The undulator third harmonic was tuned to 18.5 keV. The high heat load Si(111) monochromator was detuned to 80% intensity, as was the first Si channel-cut crystal in the post-monochromator. The second Si channel cut was detuned to 25% intensity. The incident slit size was typically 0.1 mm high by 0.3 mm wide.

For both experimental runs we experienced problems with the pulser electronics. This affected the measurement of the live time fraction, making normalization of the Sr signal impossible for some of the data that were collected. Careful inspection of the data

led to the rejection of some of the measured reflections. Factors that were considered were the stability of the measured coherent fraction and position through the time the data were collected, the position of the pulser in energy as a function of time, and the coherent fraction and position of the Si signal from the substrate. Typical Si fluorescence signals for accepted samples are shown in Figure 5.3.7. For one reflection [the low coverage (2x1) 022 surface] an asymmetric reflection was assumed to aid in fitting [12]. The results of the XSW measurements with proper dead time correction are summarized in Table 5.3.1.

Table 5.3.1 Sample, annealing history, LEED pattern, coverage and XSW data for the Sr/Si(001) surfaces examined in this study.

Sample	Annealing History	LEED	Sr Coverage ± 0.05 (ML)	Reflection hkl	P_H ± 0.02	f_H ± 0.02	Fig.
A	No Anneal	3x1	0.66	004	0.85	0.20	5.3.2
B	1 min 750°	2x1	0.57	004	0.84	0.25	5.3.3
B	1 min 750°	2x1	0.57	022	0.42	0.34	5.3.3
C	10 min 700°	2x1	0.31	004	0.73	0.42	5.3.4
C	10 min 700°	2x1	0.31	022	0.39	0.45	5.3.4
B	1+10 min 750°	3x2	0.15 ± 0.02	022	0.45	0.44 ± 0.03	5.3.6
B	1+10 min 750° +1 min 800°	3x2	0.13 ± 0.02	004	0.86	0.55	5.3.5
C	10 min 700° +1 min 800°	3x2	0.09 ± 0.02	004	0.88	0.39	5.3.5

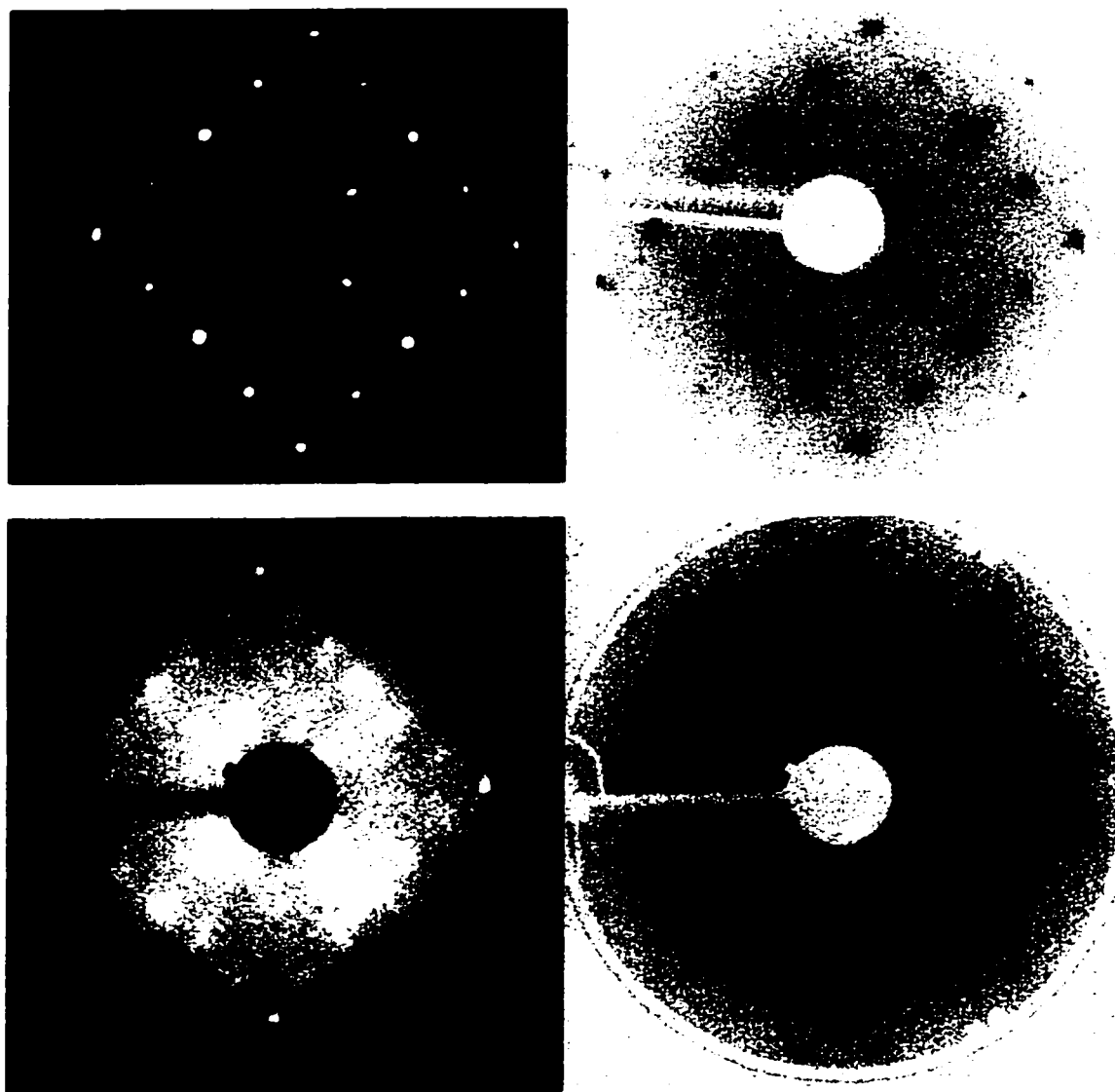


Figure 5.2.2 LEED diffraction patterns from the Sr/Si(001) surface. Top row shows clean Si, exhibiting the (2x1) surface reconstruction at a LEED bias of 49.9 Volts. The real image and inverse image are shown. The second row shows LEED images (real and inverted) taken at a bias of 49.8 Volts of a Sr layer grown on Si at room temperature by MBE, 30 minutes exposure to a Knudsen cell at 350°. A (3x1) reconstruction is revealed. The fractional-order LEED spots are not sharp, as the surface has some degree of disorder, it was not annealed. The Sr coverage was 0.66 ML.

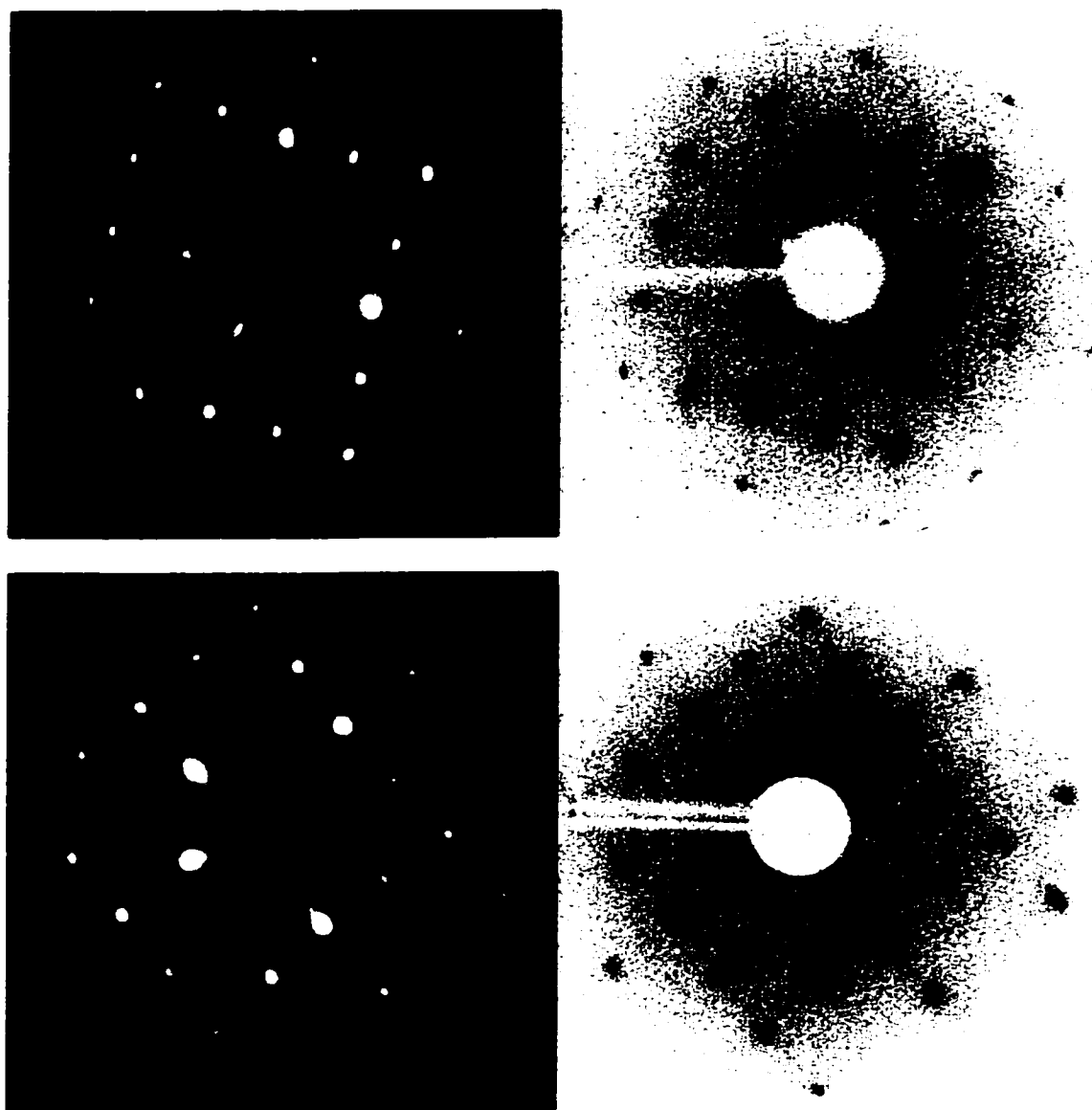


Figure 5.2.3 LEED images and inverted LEED images for the (2x1) surfaces. The top row shows a sample annealed for 1 minute at 750°C, for a Sr coverage of 0.57 ML. The bias voltage was 52.4 Volts. The bottom row shows a sample annealed at 700°C for 10 minutes, for a Sr coverage of 0.31. The bias voltage was 50.0 Volts.

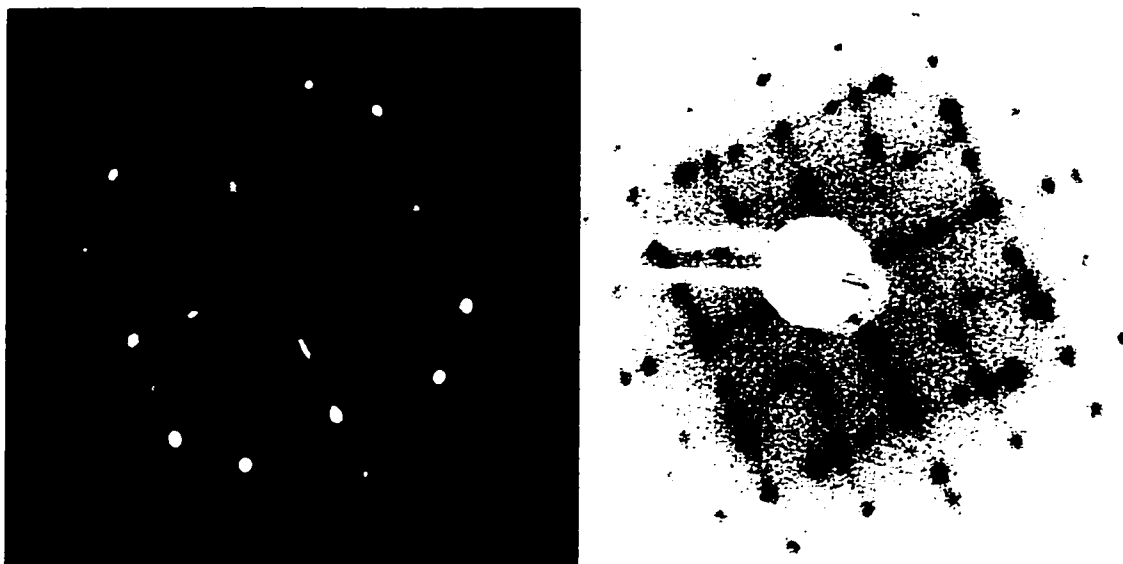


Figure 5.2.4 LEED images and inverted LEED images for a (3x2) surfaces. The sample was annealed for 10 minutes at 700°C and then 1 minute at 800°C, for a Sr coverage of 0.09 ML. The bias voltage was 50.0 Volts.

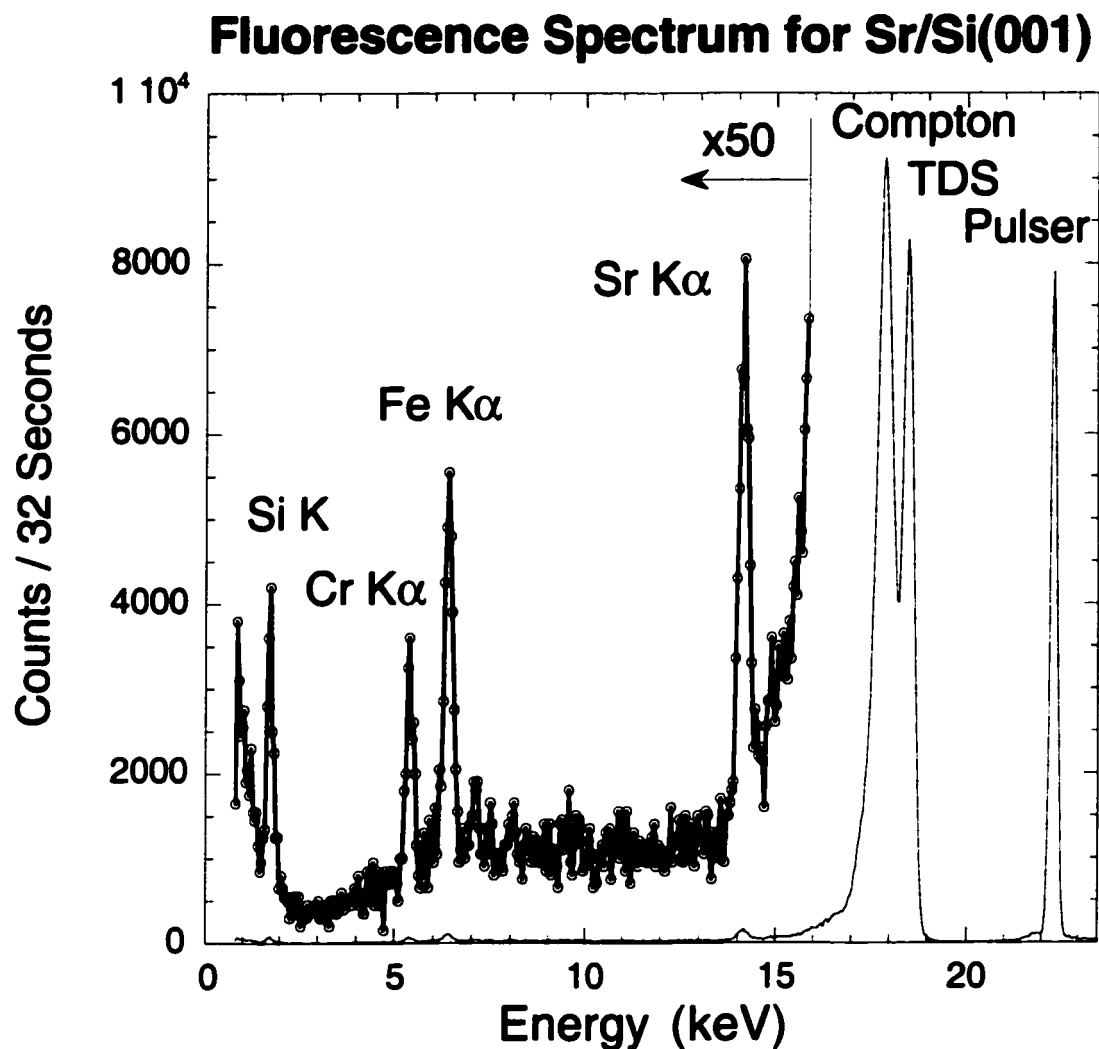


Figure 5.3.1 The x-ray fluorescence spectrum recorded by a Si(Li) solid-state detector from a 0.6 ML Sr/Si(001) surface. The incident photon energy was 18.5 keV. The Cr and Fe signals are from scattered x-rays that have excited steel components of the manipulator and x-ray chamber. The x-rays pass through two Be windows of 0.125 and 0.008 mm in thickness.

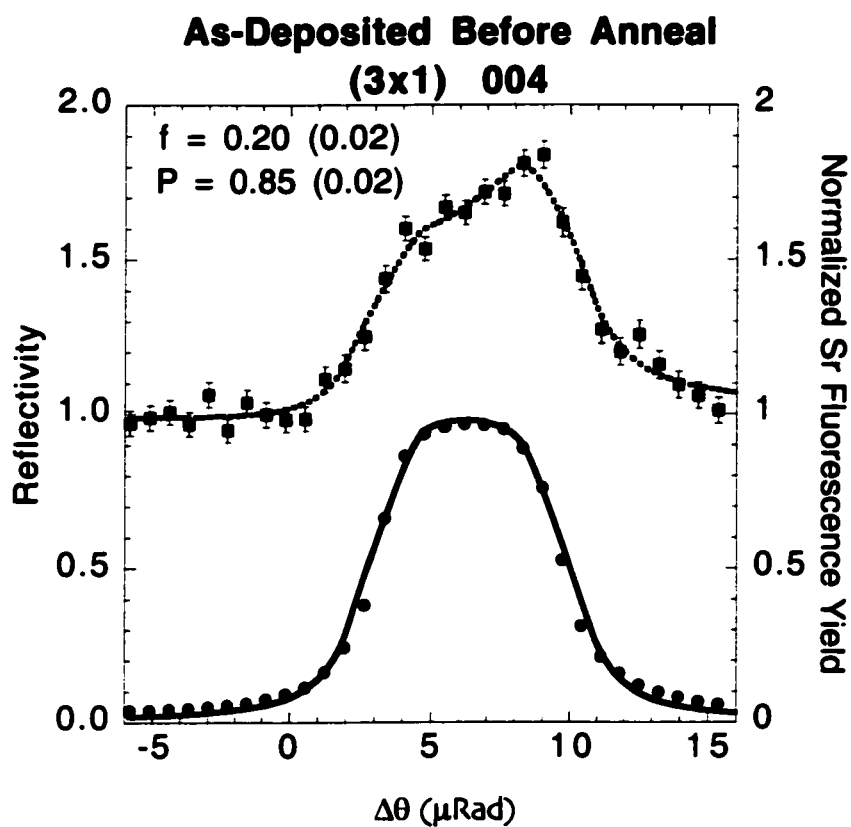


Figure 5.3.2 XSW measurement of the as-deposited unannealed Sr/Si(001) surface. Sr coverage is 0.66 ML.

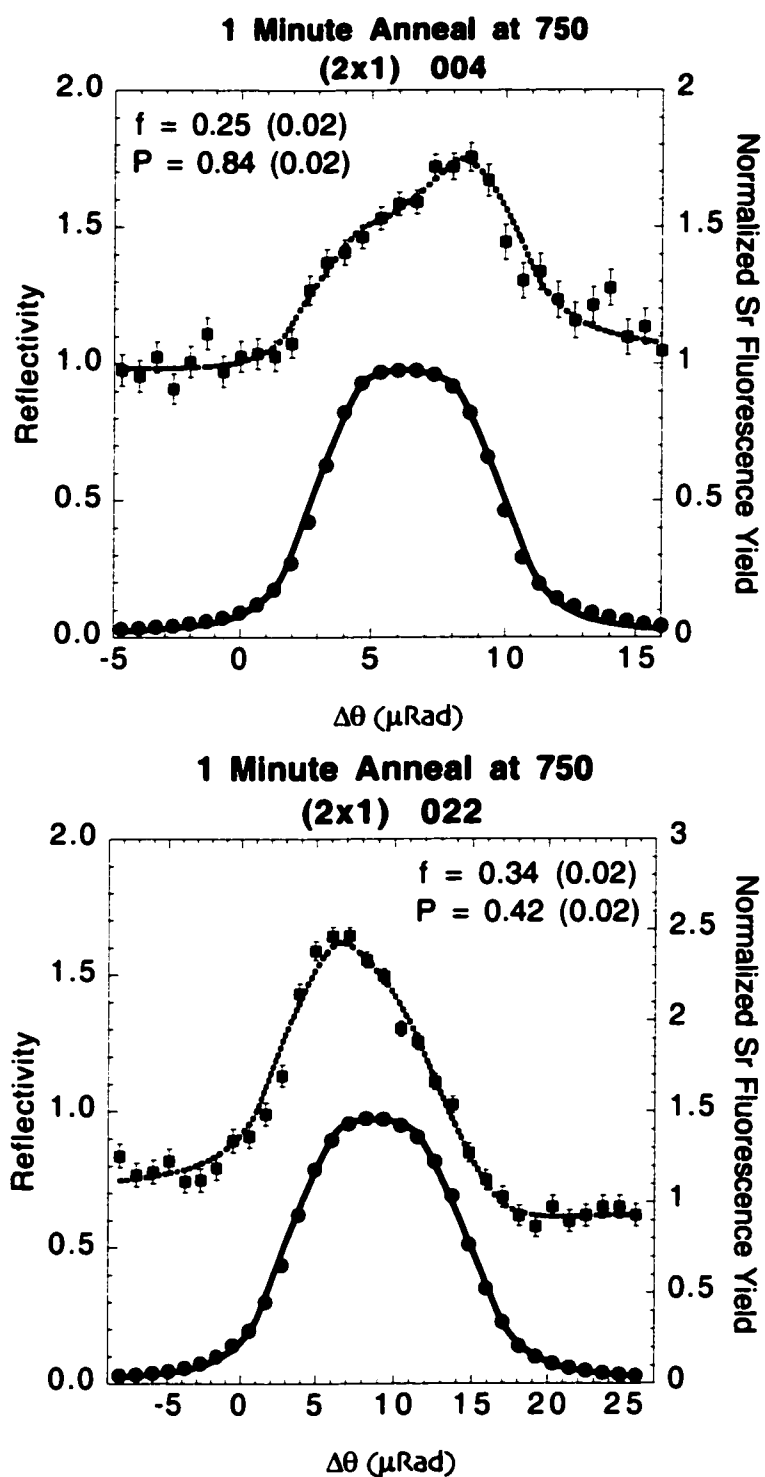


Figure 5.3.3 The XSW results of the 1 minute 750°C (2x1) surface. The Sr coverage is 0.57 ML.

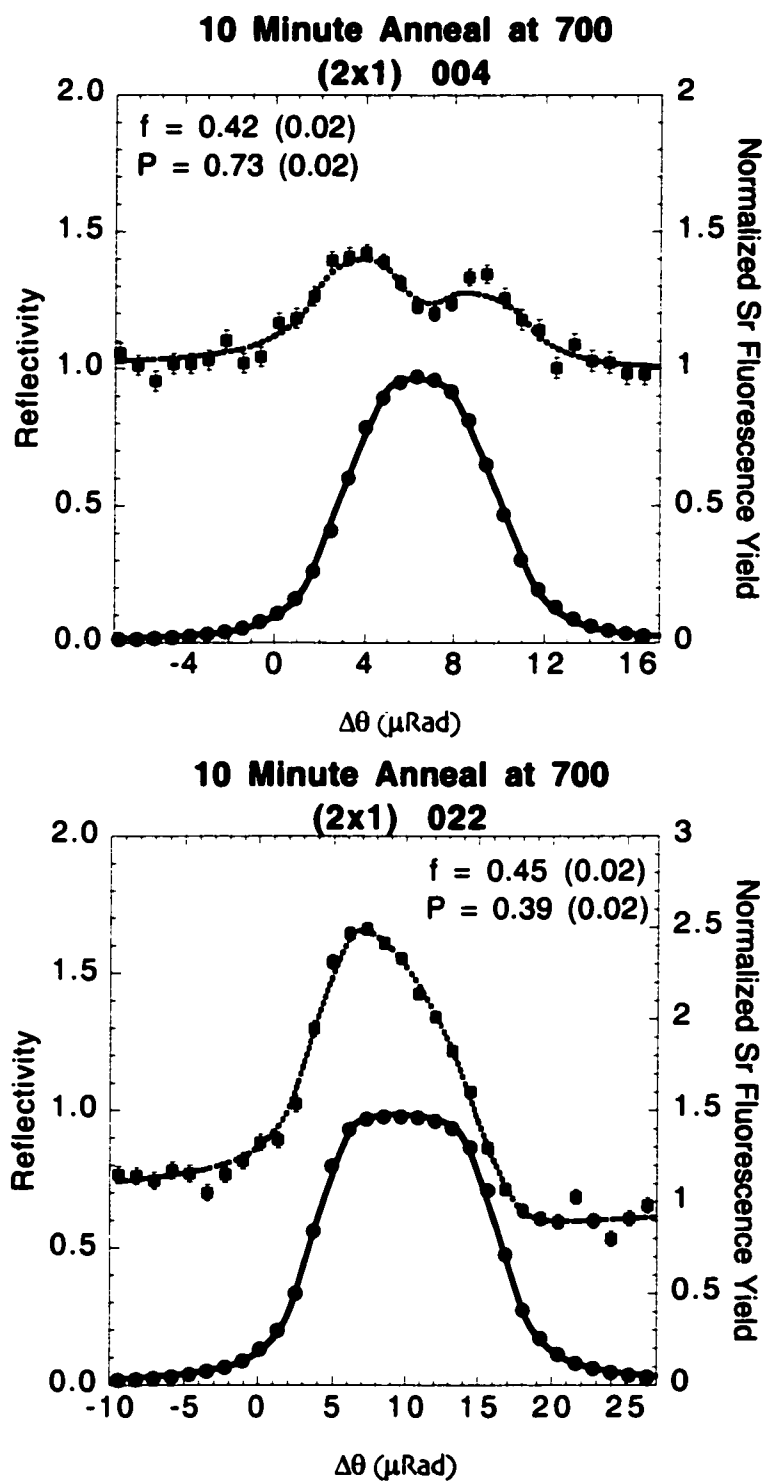


Figure 5.3.4 The XSW results of the 10 minute 700°C (2x1) surface. The Sr coverage is 0.31 ML.

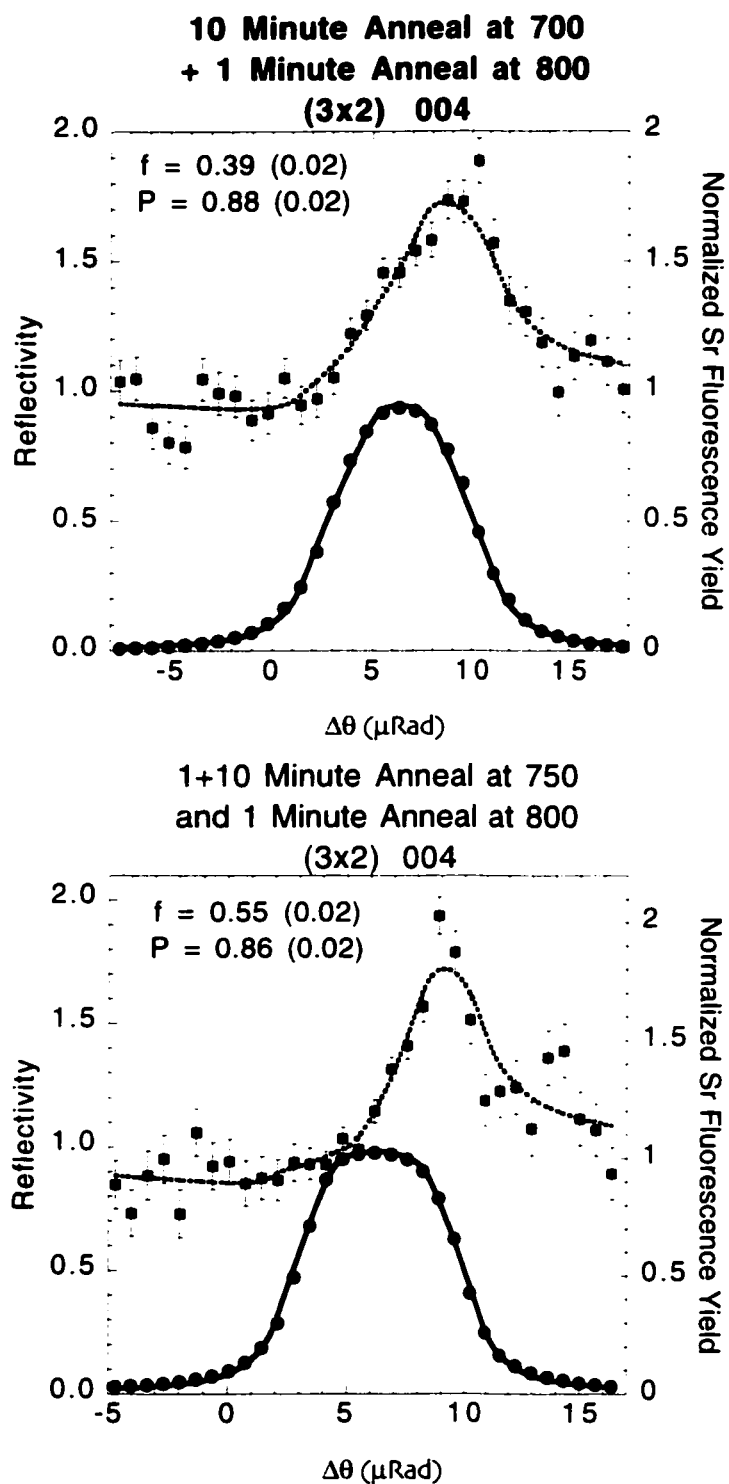


Figure 5.3.5 The XSW results of the (3x2) 004 surfaces. The Sr coverages are 0.13 and 0.09, respectively. These are two completely separate but similar surface preparations that give similar LEED, coverage and XSW P_{004} values.

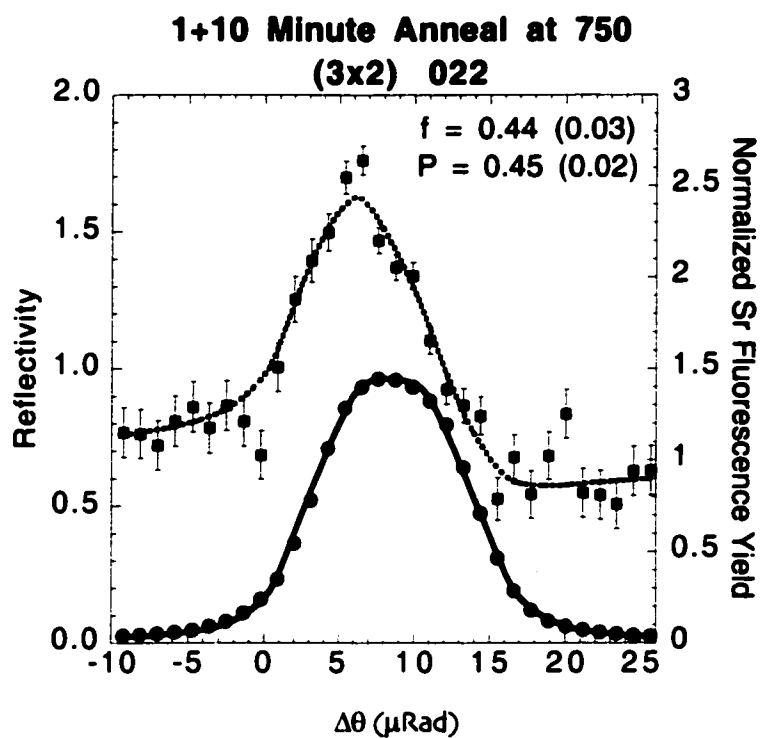


Figure 5.3.6 The XSW results of the 022 reflection of the (3x2) surface. The Sr coverage is 0.15 ML.

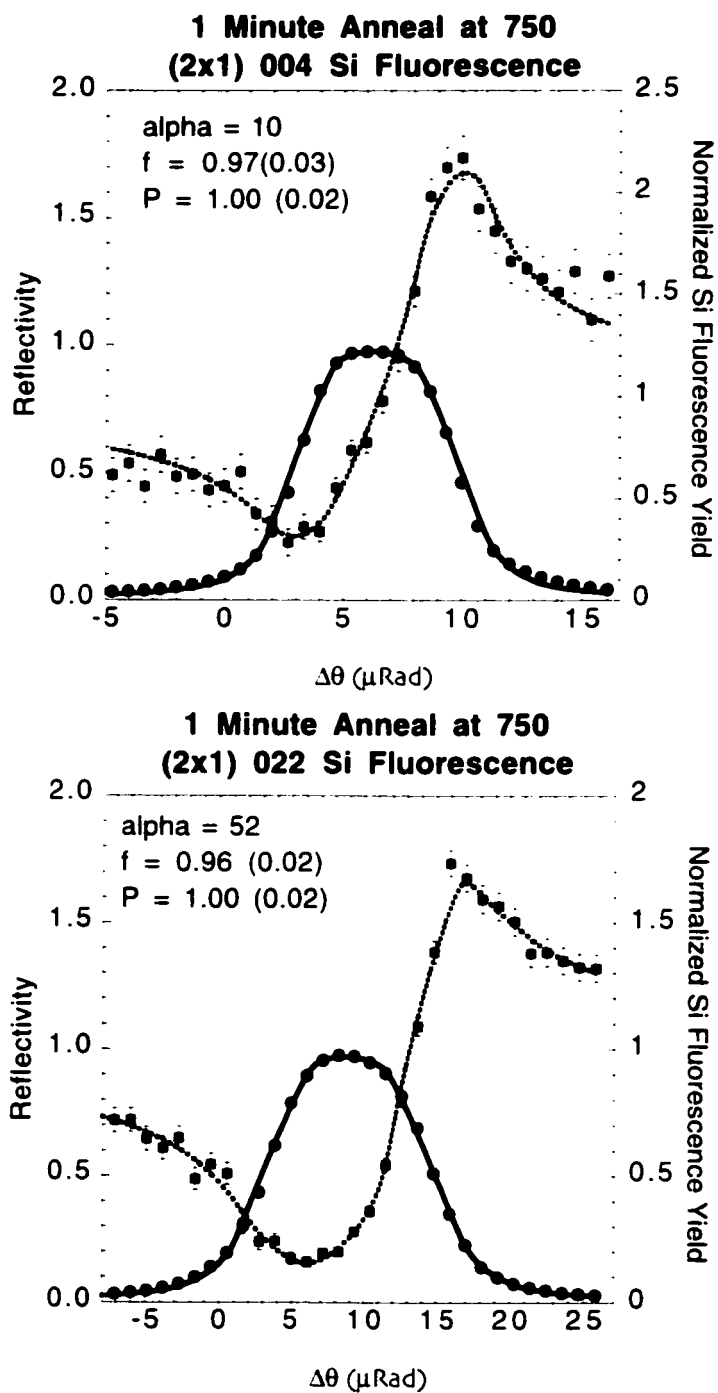


Figure 5.3.7 The XSW results of the substrate Si $K\alpha$ fluorescence signal for the high Sr coverage (2x1) sample. Coherent fraction, position and take off angle α are at expected nominal values, proving that the experimental system and data analysis are working properly.

5.4 Discussion of Sr/Si(001) Results

Before examining the structural information revealed by the XSW measurements, the relationship between coverage and surface phase will be discussed. Figure 5.1.1 is the phase diagram as explored by Fan *et al.* The Sr coverages in both Fan's and Bakhtizin's studies were established by depositing a known amount of Sr on to the clean Si(001) (2x1) reconstructed surface and then annealing to a given temperature. As no post-annealing coverage measurements were presented, this opens the possibility that some of the Sr deposited by Fan desorbed in the annealing process.

Fan observed a (3x1) reconstruction after annealing deposited surfaces of above 1.2 ML. We measured a diffuse (3x1) LEED pattern on an unannealed sample that had a coverage of 0.66 ML. Bakhtizin also reported the (3x1) reconstruction above 1 ML, but Hu, who measured coverage after post-deposition annealing, did not observe a (3x1) phase.

Between 0.45 and 1.05 ML deposited coverage, Fan observed a (2x1) Sr reconstruction. While Bakhtizin did not report this phase, Hu reported that it existed between 0.3 and 0.5 ML, measured after annealing. We found (2x1) reconstructions at 0.31 and 0.57 ML, measured after annealing. The first measurement is consistent with Hu, and the second is discussed with the XSW results.

The low-coverage (3x2) reconstruction was observed between 0.25 and 0.45 ML by Fan, and between 0.2 and 1.0 ML by Bakhtizin. Hu reports the (3x2) reconstruction at a local coverage of 1/6 ML. We were able to observe (3x2) reconstructions at coverages of 0.09, 0.13 and 0.15, consistent with Hu.

One measurement was taken of an unannealed (3x1) surface. The absence of an anneal, combined with the high background of the LEED pattern, supports a surface with some structure, but with a large number of disordered atoms. This is confirmed by the (004) XSW measurement that places the coherent fraction at 0.2. The vertical (004) coherent position of the Sr adatom is 0.85, which is consistent with the results of the high-temperature anneals leading to the (3x2) reconstruction. Due to the low coherent fraction from the (004) measurement and the diffuse LEED pattern, no (022) measurement was made of this surface, and hence the three-dimensional position of the Sr adatom in the (3x1) reconstruction was not triangulated.

The (2x1) surface was measured on a pair of samples. The first sample was annealed at 700°C for 10 minutes. The measured coverage after annealing was 0.31 monolayers. The coherent position in the (004) and (022) measurements were 0.73 and 0.39, respectively, with coherent fractions of 0.42 and 0.45, respectively. The coherent positions are consistent within the error bars of 0.02 with the symmetry relationship $P_{022} = P_{004} / 2$. By symmetry, this indicates that the Sr adatoms occupy either the cave or bridge sites on the Si(001) (2x1) surface. The second surface was annealed at 750°C for 1 minute. The coverage after annealing was 0.57 ML. The (004) XSW measurement gave a coherent position of 0.84 and a coherent fraction of 0.25, while the (022) measurement revealed a coherent position of 0.42 and a coherent fraction of 0.34. Again, the coherent positions are consistent with the symmetry required for the cave or bridge sites. The coherent fractions are low, which would imply a large degree of randomness on the surface. While a (2x1) reconstruction was observed by LEED, it would appear

that the short anneal and the lack of desorption left a lot of disordered atoms on the surface. Note that at 0.57 ML, this sample was outside the range of (2x1) surfaces observed by Hu. This also lends credence to the assumption that a good portion of the atoms on this surface did not contribute to the (2x1) reconstruction. The two measurements on the (2x1) surface gave two different positions, each consistent with a bridge or cave site. The two different heights agree with Fan's belief that two different (2x1) phases exist.

XSW measurements were performed on three samples exhibiting the (3x2) surface. The first was grown by annealing the surface at 700°C for 10 minutes, cooling, and then annealing at 800°C for 1 minute. The other (3x2) samples were grown by annealing the surface at 750°C twice, once for 1 minute, then again for 10 minutes. The surface was measured, and then annealed at 800°C for 1 minute. The measured coverages were 0.15, 0.13 and 0.09 ML, respectively. Due to pulser difficulties and time constraints, a pair of analyzable (004) and (022) reflections was not taken on any (3x2) surface. However, the measured coverages for all three reflections are close, and as a group the XSW data form a consistent model.

Data for the (004) reflection were taken at the 0.13 and 0.09 ML coverages. The coherent positions were 0.86 and 0.88, respectively. The coherent fractions for these measurements were 0.55 and 0.39. The (022) reflection yielded a coherent position of 0.45 with a coherent fraction of 0.44. Like the atomic positions for the (2x1) surface reconstructions, these locations obey the symmetry rules that place the Sr in the cave or bridge site. This position is consistent with the (3x1) (004) position and also the high

coverage (0.57 ML) (2x1) positions. See Figure 5.4.1 for a comparison of the atomic positions of the three different Sr coverages.

By combining STM, coverage, and structural information, the Sr/Si(001) (3x2) surface can be solved. Bakhtizin's STM results suggested cave site occupation for the (2x3) reconstruction, with Sr coverage at 1/3 of a monolayer. This agrees with the XSW results. The relationship between the coherent positions for the (004) and (022) reflections is consistent with either a cave or bridge site. However, in both our work and in Hu's, the (3x2) reconstruction is revealed at low coverage, 1/6 of a monolayer for Hu,

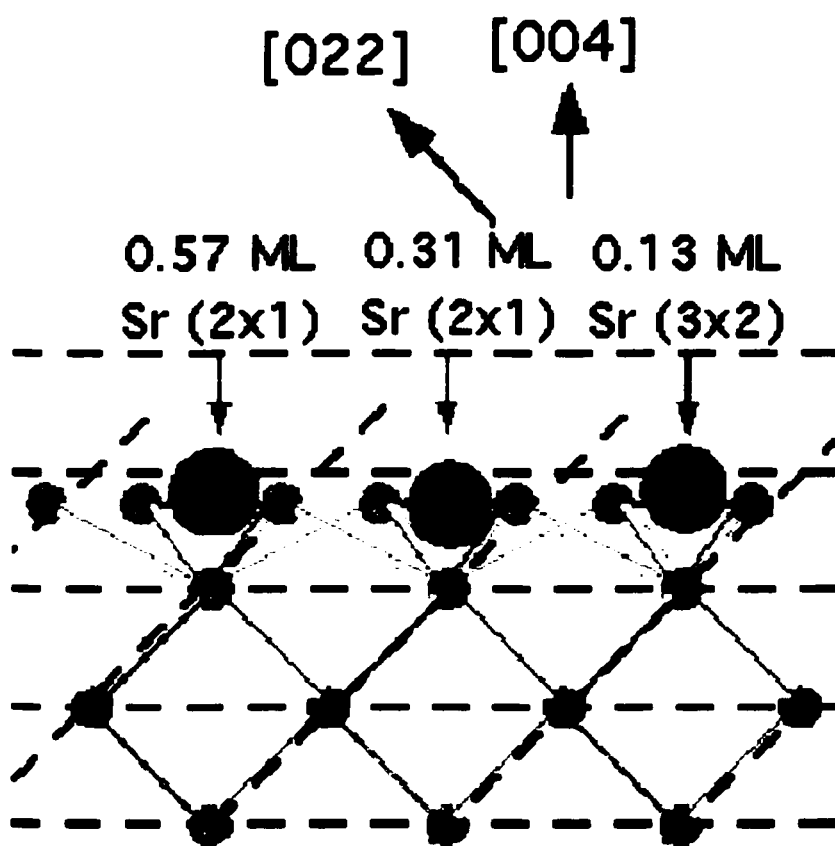


Figure 5.4.1 The positions of the Sr atoms as determined by XSW for the three different measured coverages.

and at $\theta = 0.15, 0.13$ and 0.09 for our samples. With this in mind, a model with an Sr atom occupying every third cave site is proposed, with chains of Sr running parallel to the direction of the Si dimers bonds (see Fig 5.4.2).

The Sr/Si(001) (2x1) XSW data is also consistent with a cave or bridge site. We found that the (2x1) reconstruction existed up to 0.57 ML after annealing, whereas Hu found it up to 0.5 ML. If the preferred Sr adsorption site for the (2x1) surface is the same as the (3x2) surface, then the reconstruction consists of Sr occupying every cave site (see Fig 5.4.2). We also found that at 0.31 ML the position of the Sr atom was slightly lower

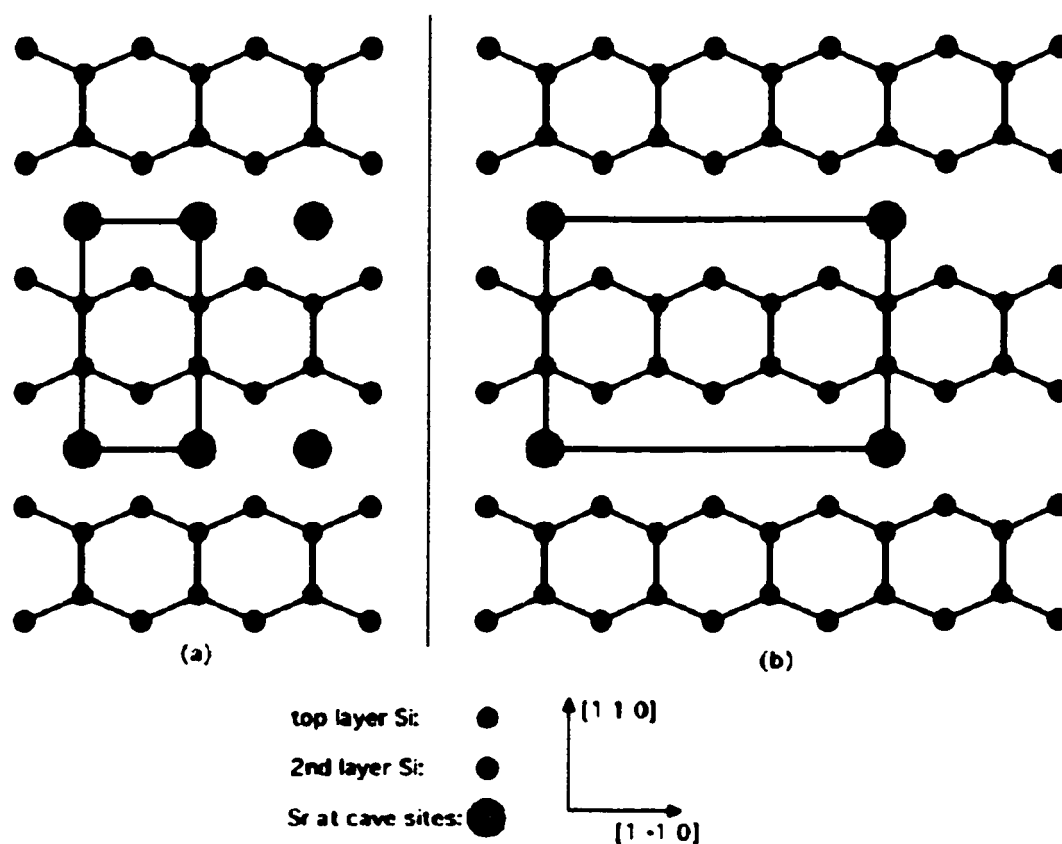


Figure 5.4.2 Proposed models for the (2x1) and (3x2) reconstructions. The model on the left shows a Sr atom in every cave site, corresponding to a (2x1) surface. The model on the right has a Sr atom at every third cave site for a (3x2) reconstruction.

than at 0.57 ML. This is consistent with Fan's finding of two different (2x1) phases.

In summary, three different surface reconstructions were observed in the Sr/Si(001) experiments. A diffuse (3x1) sample was observed to exist at 0.66 ML. It had a coherent position normal to the Si (001) surface matching that of high-temperature anneal (3x2) reconstructions. A pair of (2x1) surfaces were examined. One, at a coverage of 0.57 ML, was consistent with a cave or bridge site, and was found at a position that matched the (3x1) and (3x2) reconstructions. The other, with a coverage of 0.31 ML, was also in the cave or bridge site but was lower than either the (3x1) or (3x2) positions. The (3x2) surface was measured by taking data on three different surfaces with different annealing histories but near identical coverages. The coherent positions from the (004) and (022) measurements suggest by symmetry the cave or bridge sites. Combining STM, coverage and XSW data, a model for the Sr/Si(001) (3x2) surface is proposed; the Sr atoms occupy every third cave site, in chains that run parallel to the direction of the Si dimers. Extending Bakhtizin's STM results from the (3x2) case to the (2x1) reconstruction leads to a surface in which Sr occupies every cave site.

Chapter 6 Thin Film X-ray Standing Wave Measurements of MOCVD-Grown PbTiO_3 / SrTiO_3

6.1 PbTiO_3 Structure and Growth

Due to its ferroelectric and piezoelectric properties, $\text{Pb}(\text{Zr}_x\text{Ti}_{1-x})\text{O}_3$ (PZT) is of much interest in the ferroelectric community, however, our first experiments on ferroelectrics with thin-film standing waves were on the simpler system PbTiO_3 (PTO), grown epitaxially on the (001) surface of SrTiO_3 (STO). This was a simple case of a film grown on a surface, as opposed to a capacitor structure that would have involved both top and bottom electrodes. The drawback of this structure is that the films could not be electrically switched, and only the as-grown polarity could be measured.

Both PTO and STO are perovskites. STO is centrosymmetric simple cubic at room temperature, whereas PTO is noncentrosymmetric tetragonal and features slight shifts of the Pb^{2+} and Ti^{4+} sublattices relative to the O^{2-} sublattice (Fig. 6.1.1). At room temperature, the lattice parameter for STO is 3.905 Å. For PTO, $a = 3.905$ Å and $c = 4.135$ Å. In PTO, the Pb^{2+} ion is displaced along the c -axis from the O plane by 0.480 Å, and the Ti is displaced 0.318 Å in the same direction. The O^{2-} ions occupy the face-centered position of the tetragonal unit cell [1].

The samples were grown via metalorganic chemical vapor deposition (MOCVD) by Chris Foster and G.-R. Bai in the Materials Science Division at Argonne National Laboratories. While many techniques exist for the growth of thin ferroelectric films [2,3,4,5,6,7], MOCVD was utilized because it features good film uniformity, crystalline

quality, compositional control, high deposition rates and can be scaled to commercial production [8]. The films were deposited on $\text{SrTiO}_3(001)$ substrates that were purchased from Coating and Crystal Technology, Inc. The substrates have a miscut of 0.65° , which will be discussed in Section 6.4. Prior to deposition, the substrates were chemically cleaned with acetone and methanol. In the MOCVD reactor, the substrates were heated to 700°C - 750°C , while the pressure of the gas mixture was held at 10 Torr. To grow the PTO, $\text{Pb}(\text{C}_2\text{H}_5)_4$ and $\text{Ti}(\text{OC}_3\text{H}_7)_4$ were used as the precursors. The Pb precursor was maintained at 20°C - 22°C at a pressure of 350 Torr, while the Ti precursor was heated to 28°C - 30°C at a pressure of 80 Torr. The vapors were delivered to the main chamber utilizing ultrapure nitrogen as a carrier gas. The delivery lines were heated to 100°C to avoid condensation of the precursors. Pure oxygen, delivered in a separate line, was used as the oxidant. The film growth rate was 50-70 Å/min [9]. The films that were investigated were 100, 200, 400 and 600 Å thick.

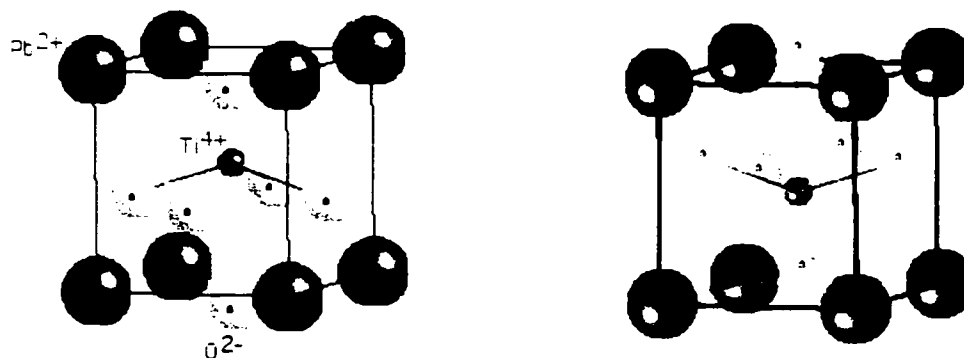


Figure 6.1.1 Room-temperature unit cells of PTO in the "Up" and "Down" orientations, respectively. The tetragonal cell is 3.905 Å along the a -axis and 4.135 Å along the c -axis. With the origin at the site of the Pb ion, the fractional displacement of the O ion from the face-center position along the c -axis is 0.112, and the Ti is displaced 0.039 in the opposite direction with respect to the body-center position.

6.2 PbTiO₃ Thin Film Experimental

X-ray standing wave experiments were performed upon the PTO thin films in July and August of 1997 and January and March of 1998 at the 5ID-C DND-CAT undulator beamline and also April of 1998 at the 12ID-D BESSRC-CAT undulator beamline. In both cases a LN₂ cooled Si(111) monochromator was used. See Figure 4.1.1 for a diagram of the experimental setup.

Thin-film XSW data were collected for films of thickness 100, 200, 400 and 600 Å, although only the 100 and 400 Å cases were investigated in detail. In most cases, the experiments were performed at an incident beam energy of 13.5 keV in order to excite Pb L α fluorescence from the Pb²⁺ ions in the PTO film. For the fluorescence measurements, the incident beam was slitted to 0.4 mm wide by 0.2 mm high, which projected to a 0.4 mm by 1.6 mm footprint on the sample at the (001) Bragg angle. The STO(001) reflection from the substrate was found, but often exhibited two or more peaks within an angular range of 0.04°, most likely due to mosaic structure of the substrate. The sample was laterally translated under the beam until a section of crystal with a single, appropriately narrow STO substrate peak could be found. Standing wave data were then recorded at the PTO film (001) Bragg peak. Several measurements were made at different locations on each crystal.

In addition to recording Pb L α fluorescence yield data, thin-film XSW scans were performed at 8.0 keV on the 400 Å film in order to observe the modulation in the Ti K α fluorescence signal, which is more difficult to collect, but is somewhat more sensitive to the polarity of the film. Due to the presence of Ti in the STO substrate, the Ti

fluorescence from the film had to be separated from the Ti fluorescence from the substrate. A fluorescence slit was placed between the sample and the detector. By using the slit, the takeoff angle of the Ti fluorescence could be controlled and the evanescent-wave effect [10] could be utilized to separate the signal of the film from the bulk Ti signal. The slit was lowered until the fluorescence signal could not be distinguished from $1 + R$ during a rocking curve scan of the STO (001) Bragg peak, meaning that the Ti that was fluorescing was not in registry with the lattice spacing of the substrate. This eliminated fluorescence from the substrate, leaving the Ti ions in the film. A sample fluorescence spectrum can be found in Figure 6.2.1.

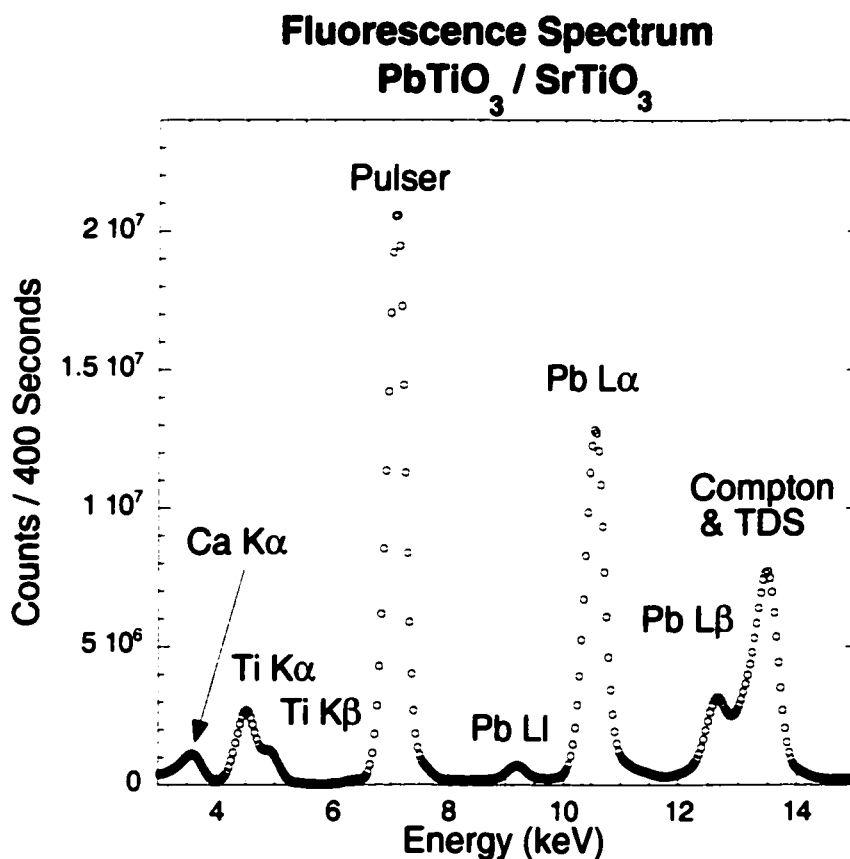


Figure 6.2.1 Fluorescence data collected by the Si(Li) detector for the 100 Å PbTiO₃ film grown on SrTiO₃ (001).

6.3 PTO XSW Results

6.3.1 Overview

A total of 13 reflections were measured and analyzed over the course of our PTO experiments. There was only one sample for each thickness, but different spots on each sample were probed. The results are summarized in Table 6.3.1.

Table 6.3.1 Summary of XSW measurements on PTO/STO reflections. Multiple reflections were recorded at different lateral positions for each sample (except the 200 Å case).

Thickness (Å)	Reflection	%Up	DWF
100	001	100	0.98
100	001	80	1.00
100	001	100	0.94
100	002	0	0.98
100	002	100	0.80
200	002	100	0.84
400	001	100	0.88
400	001	100	0.88
400	002	100	0.90
400	001 - Ti	100	0.78
400	002 - Ti	0	0.68
600	001	50	0.88
600	001	80	0.82

6.3.2 – 100 Å Sample

For the five different lateral positions examined on the 100 Å thick PTO film, three of the five reflections best fit the 100% up case, while one of the reflections best fit 80% up, and the last reflection corresponds to a 100% down best fit. Three observations were made at the (001) reflection. Two of the three fit the 100%, and the other best fits 80%. All three of the reflections have static Debye-Waller factors near unity, suggesting that the films were well grown, free from defects.

The (002) XSW scans show one spot that is 100% up and one that is 100% down. The 100% up case has a static Debye-Waller factor of 80%, the worst for any reflections taken on this sample. The 100% down case had an ideal near-unity static Debye-Waller factor. This same sample was examined independently with CTR by Thompson *et al.* [11]. They reported that it was polarized down.

6.3.3 – 400 Å Sample

On the 400 Å film, three reflections were examined at 13.5 keV, and two more were observed at 8.0 keV, utilizing the evanescent-wave method to collect Ti fluorescence from the film. The three Pb fluorescence spots all registered as up domains. The static Debye-Waller factors for the two (001) reflections were both 0.88, and the (002) reflection was 0.90. The Ti measurements revealed one spot that was 100% up with a static Debye-Waller factor of 0.78 and another that was 100% down with a static Debye-Waller factor of 0.68. The low static Debye-Waller factors for the Ti fluorescence measurements indicate that the takeoff angle was actually above the critical angle. If a

larger takeoff angle is given to the fitting routine, deeper portions of the film are accessed, lower reflectivities are sampled, and a smaller peak-to-peak amplitude is seen in the fluorescence modulation. With the takeoff angle set to the critical angle, the fitting routine adjusts for this smaller modulation by reducing the static Debye-Waller factor.

6.3.4 – 200 Å and 600 Å Samples

Due to time constraints, only one spot was examined on the 200 Å sample. The (002) reflection revealed an up orientation with a static Debye-Waller factor of 0.84.

A pair of reflections were measured for the 600 Å film. Examination of the rocking curve fits compared with the reflectivity data for these reflections shows that the fits for the 600 Å films are not as good as the fits for the thinner films. This suggests that the thicker films most likely have more mosaic spread than the thinner films. The relationship between film thickness and film quality will be discussed in Section 6.5. These 600 Å films also did not exhibit the single-orientation behavior of the thinner films, one being a 50%-50% mix of up and down orientations, and the other being 80% up.

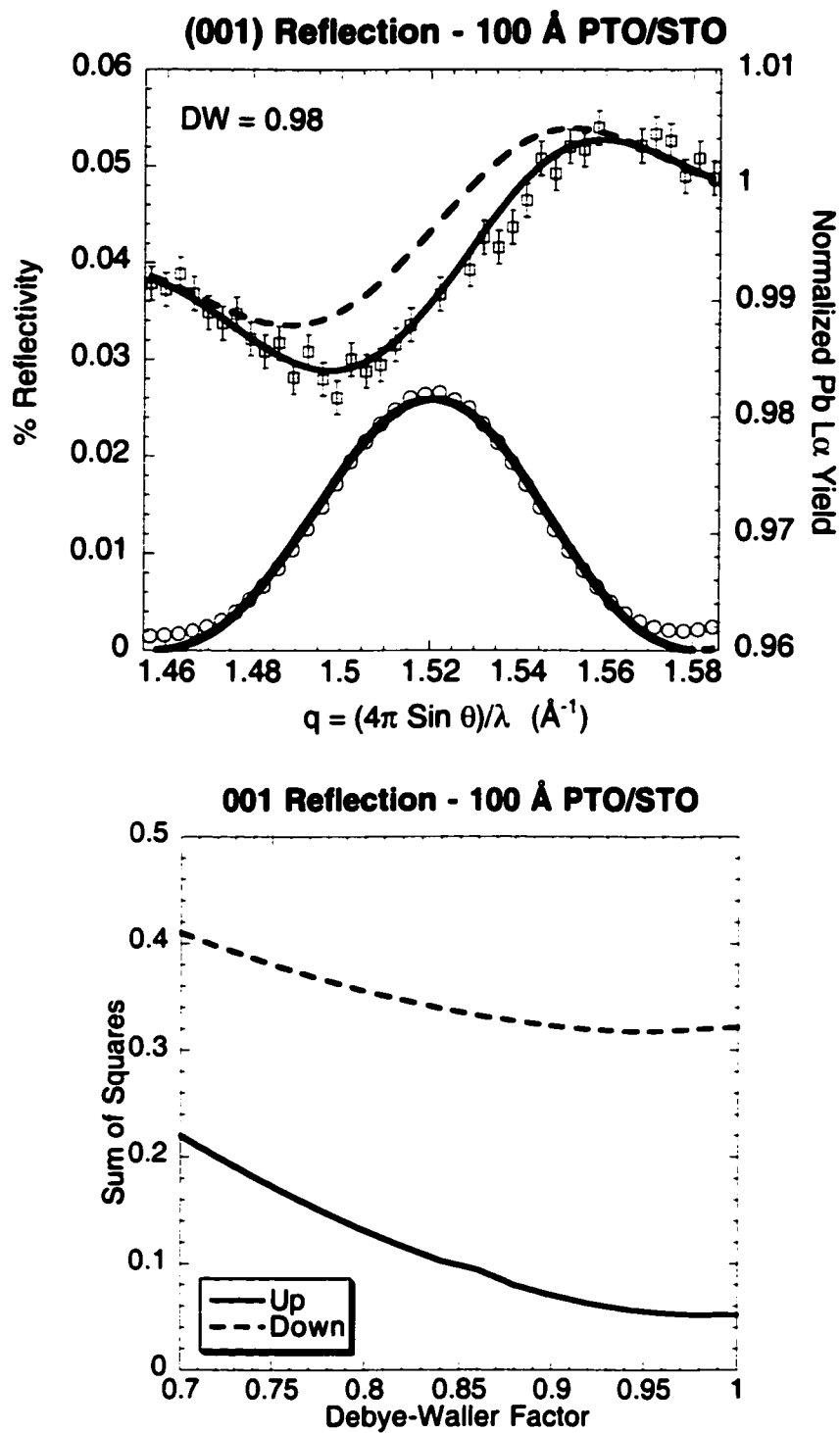


Figure 6.3.1 100 Å film (001) reflection. The film is oriented in the up direction.

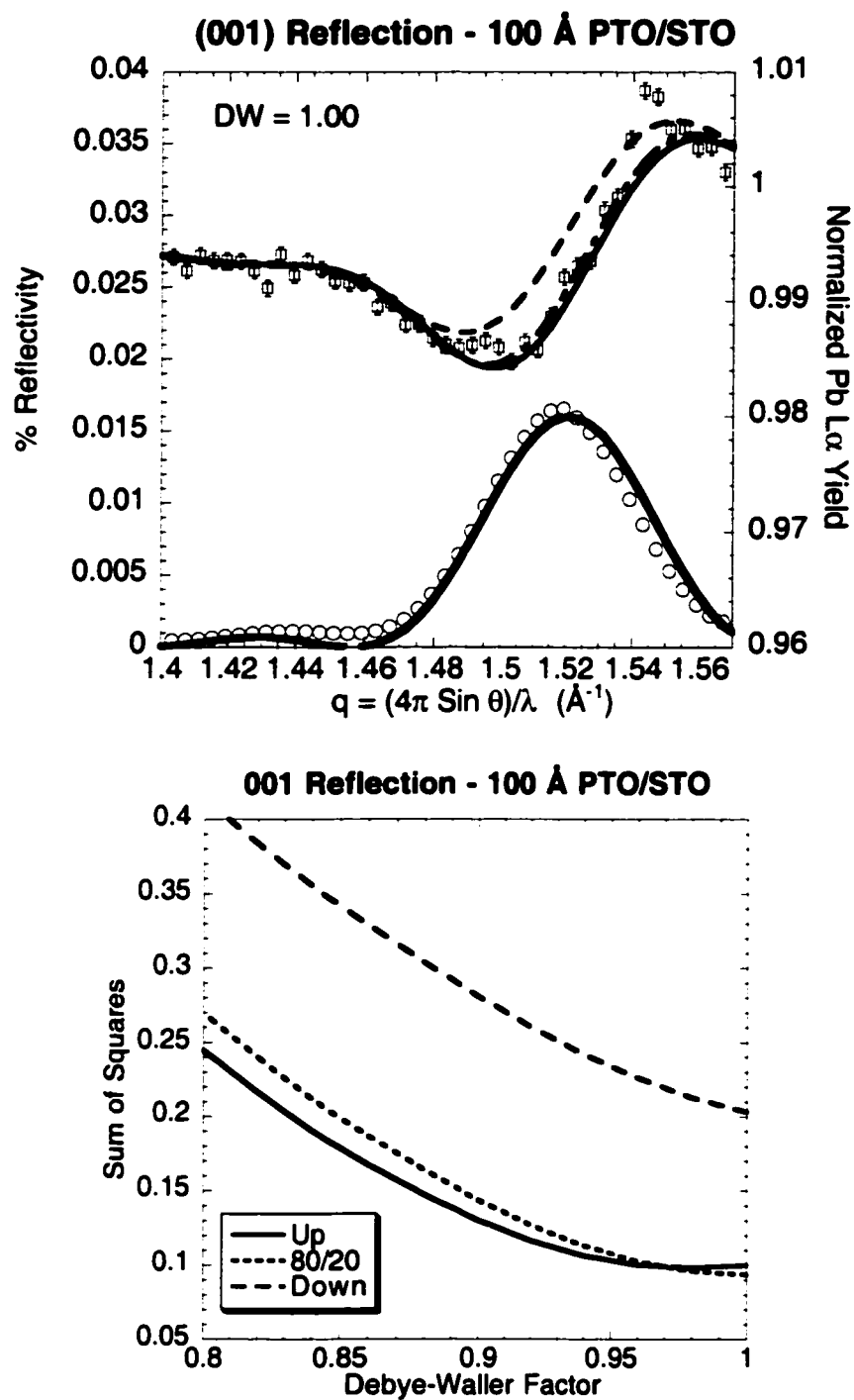


Figure 6.3.2 100 Å film (001) reflection. The film is in a mixed state, 80% up and 20% down.

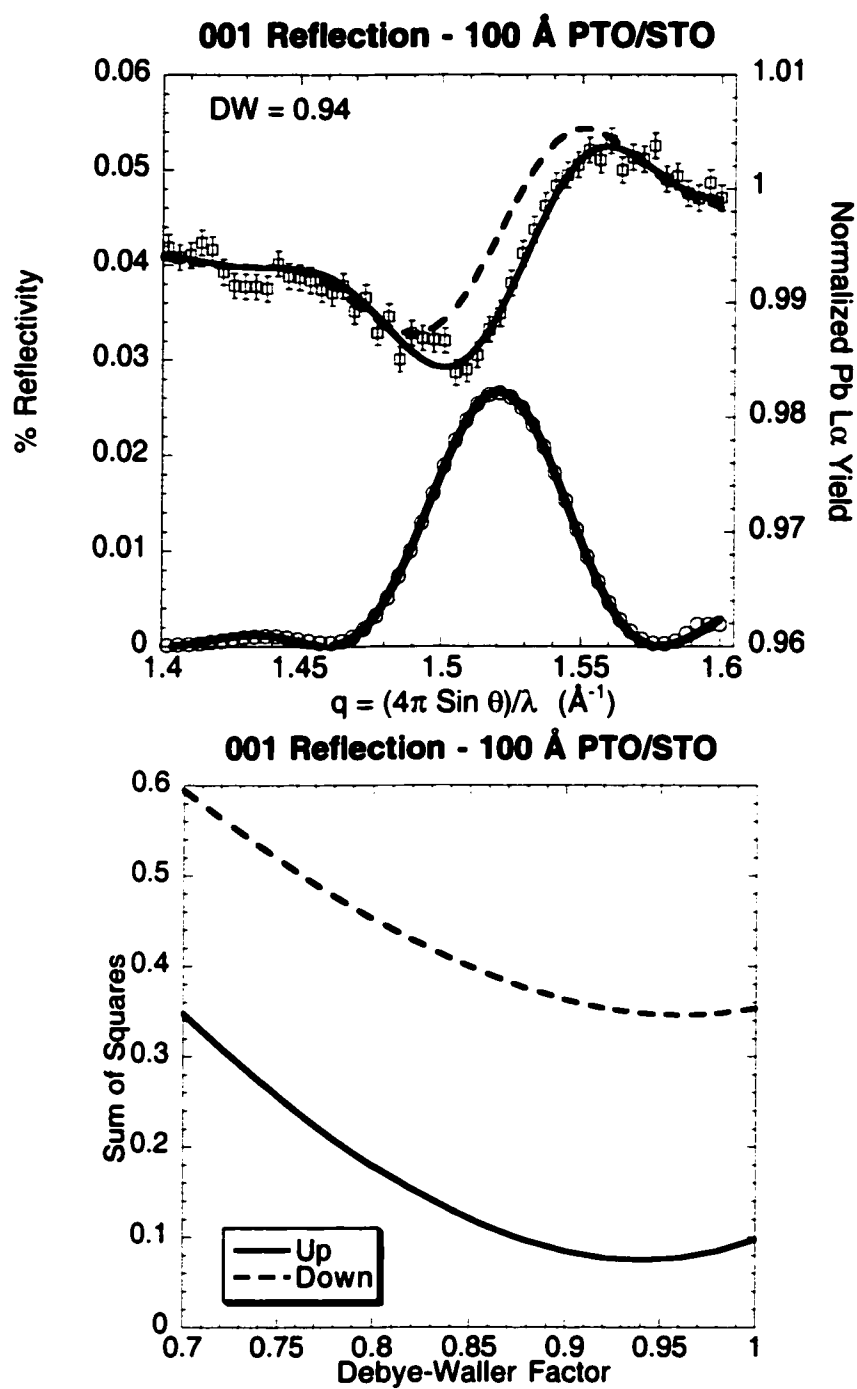


Figure 6.3.3 100 Å film (001) reflection. The film is in the up orientation.

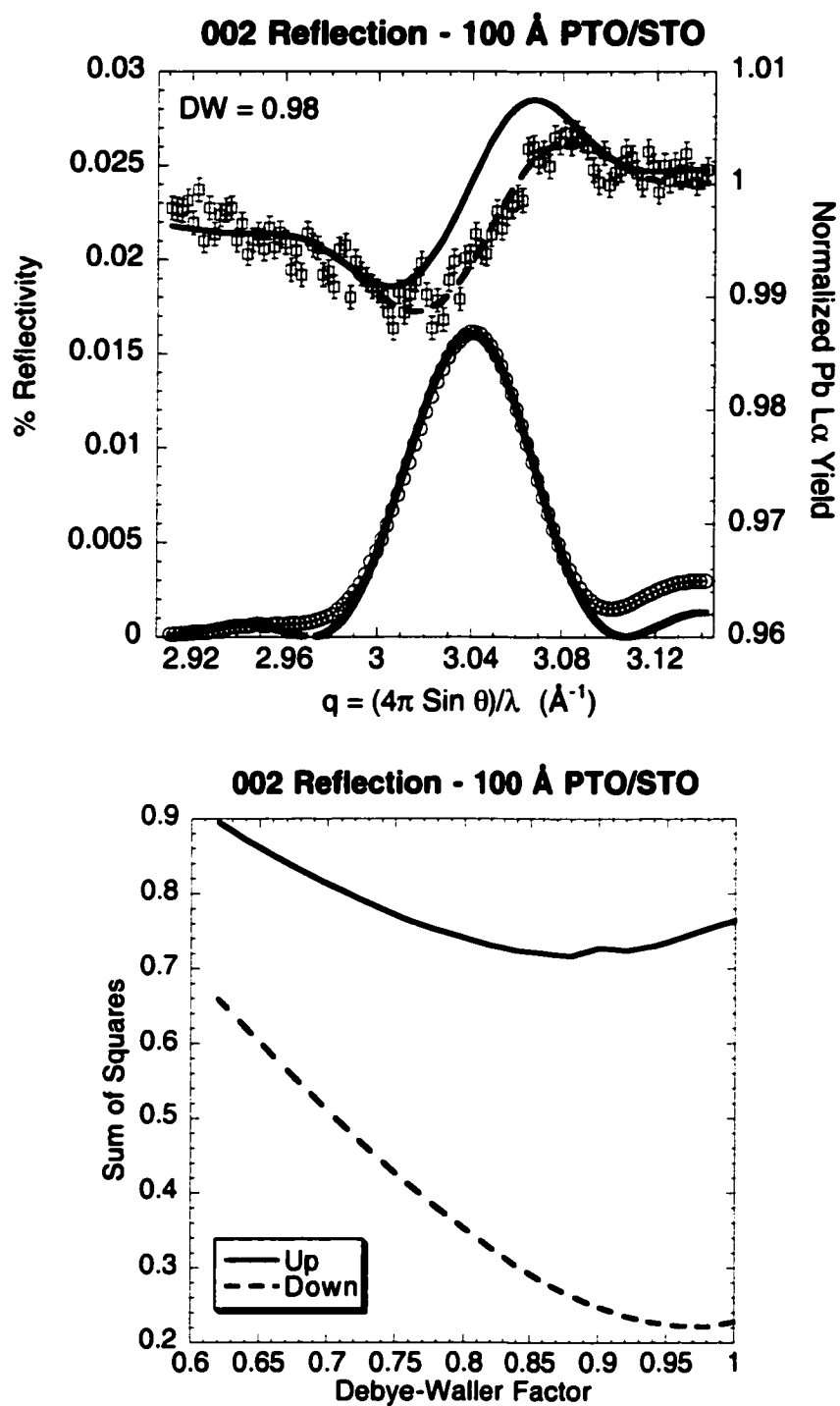


Figure 6.3.4 100 Å film (002) reflection. The film is in the down orientation.

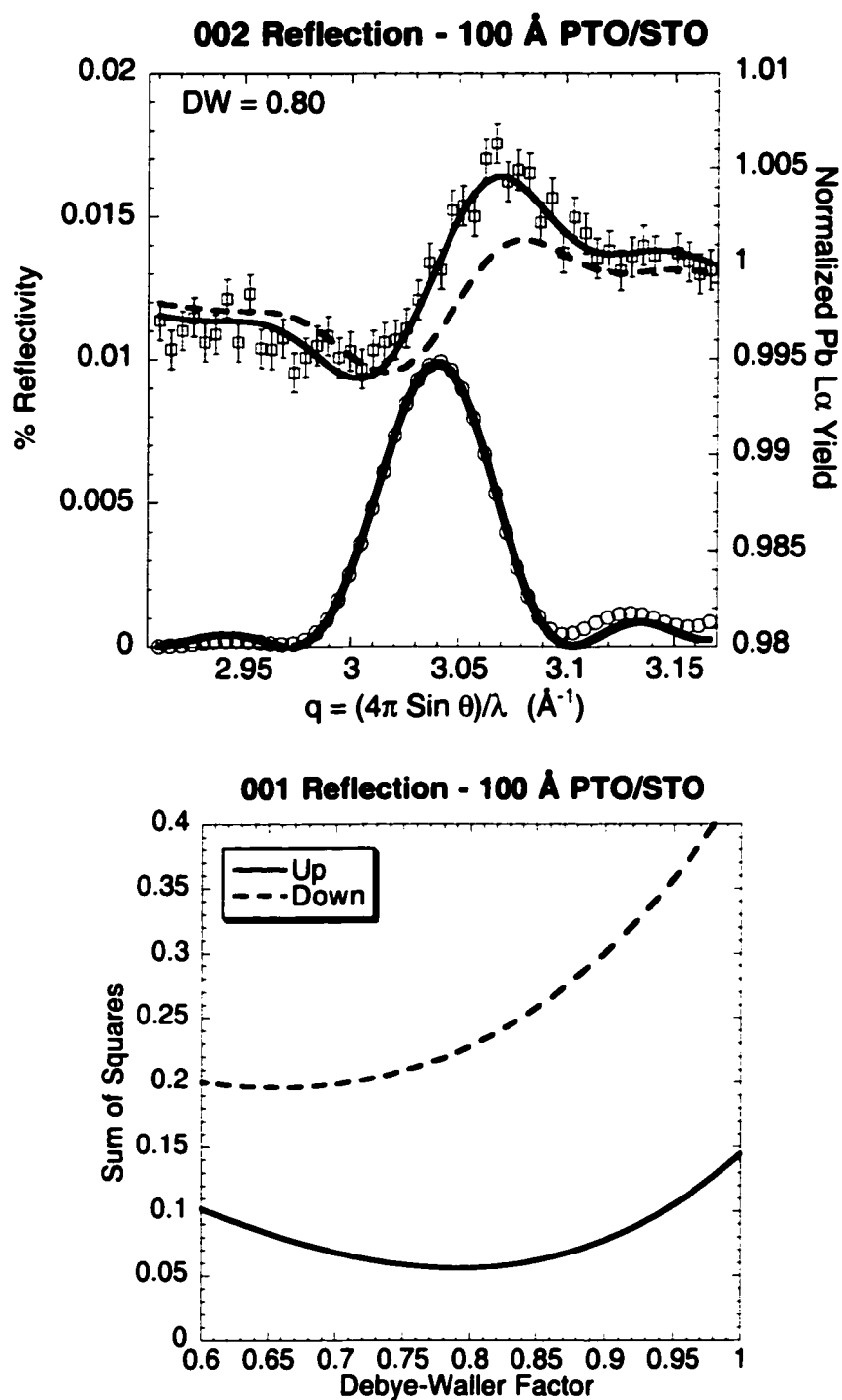


Figure 6.3.5. 100 Å film (002) reflection. The film is in the up orientation.

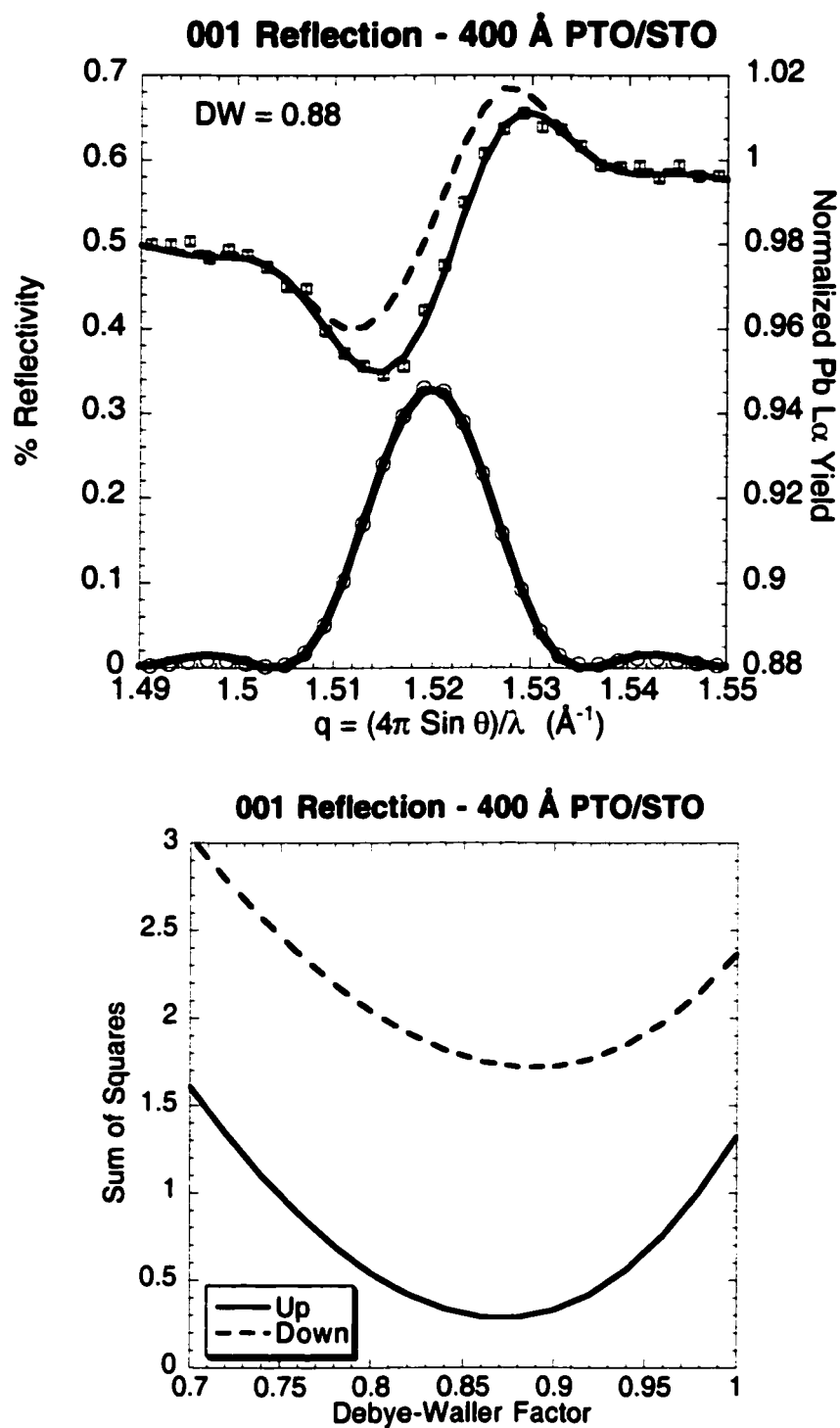


Figure 6.3.6 400 Å film (001) reflection. The film is in the up orientation.

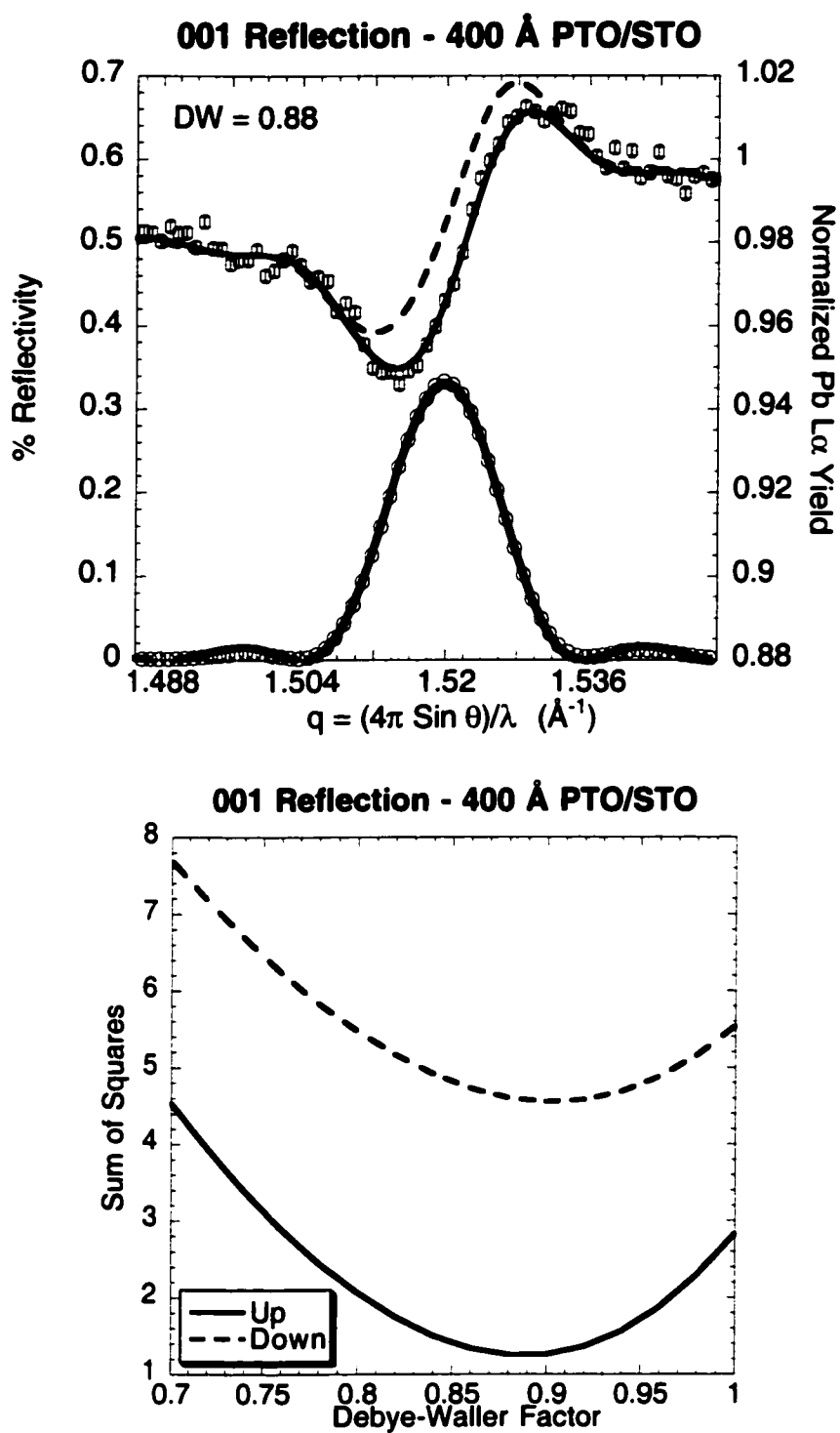


Figure 6.3.7 400 Å film (001) reflection. The film is in the up orientation.

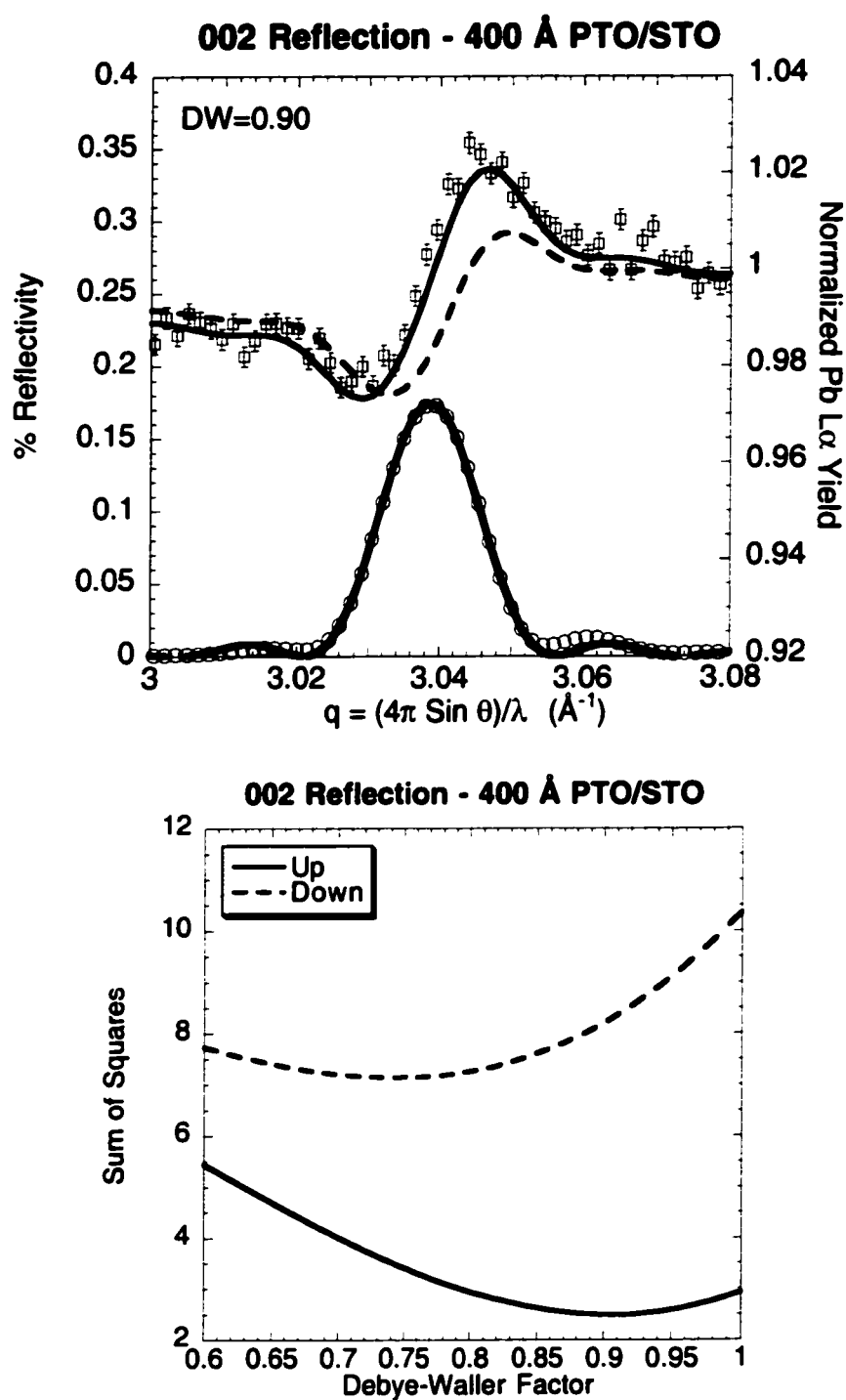


Figure 6.3.8. 400 Å film (002) reflection. The film is in the up orientation.

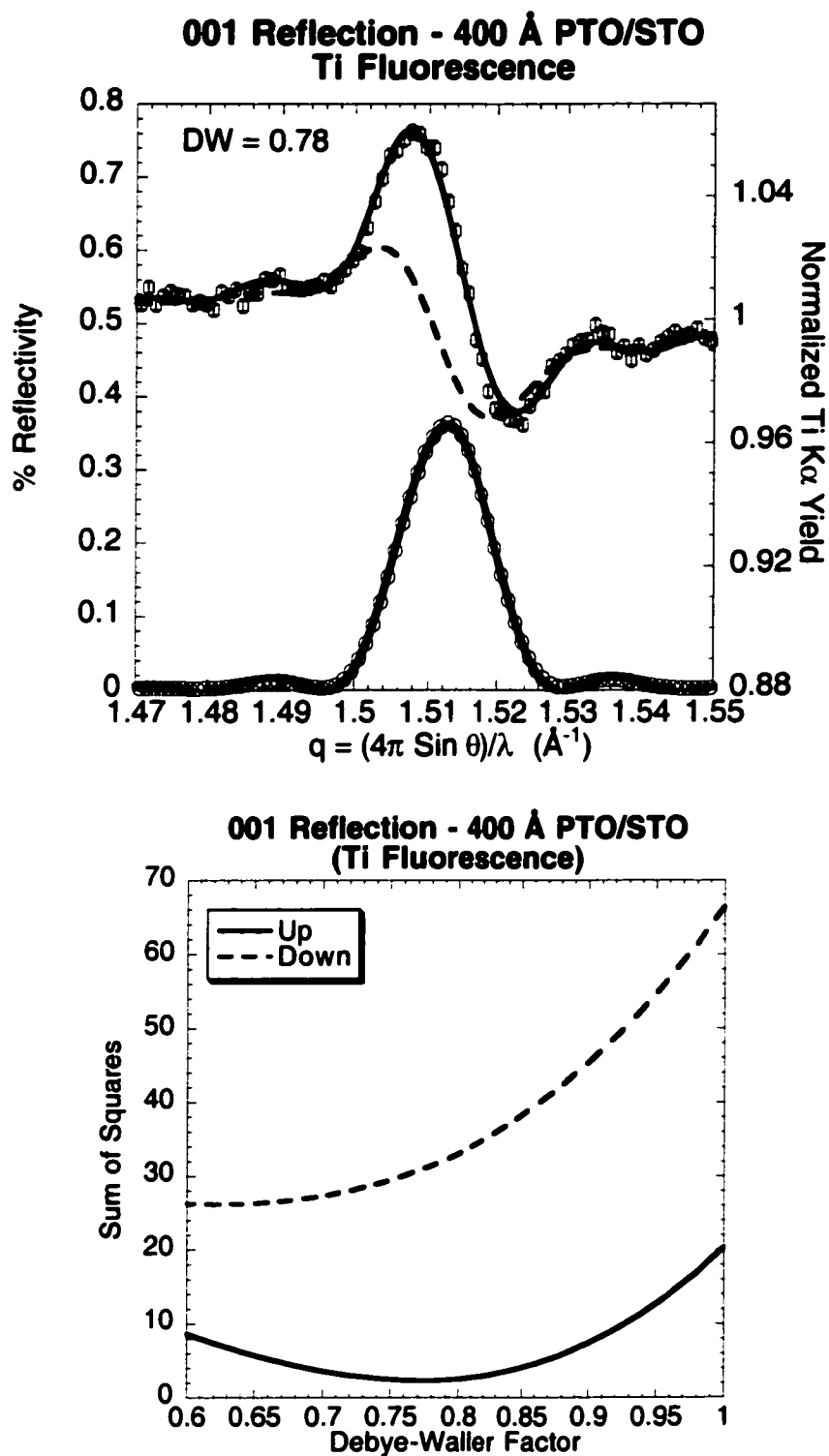


Figure 6.3.9 400 Å film (001) reflection at 8.0 keV for Ti fluorescence. The film is in the up orientation.

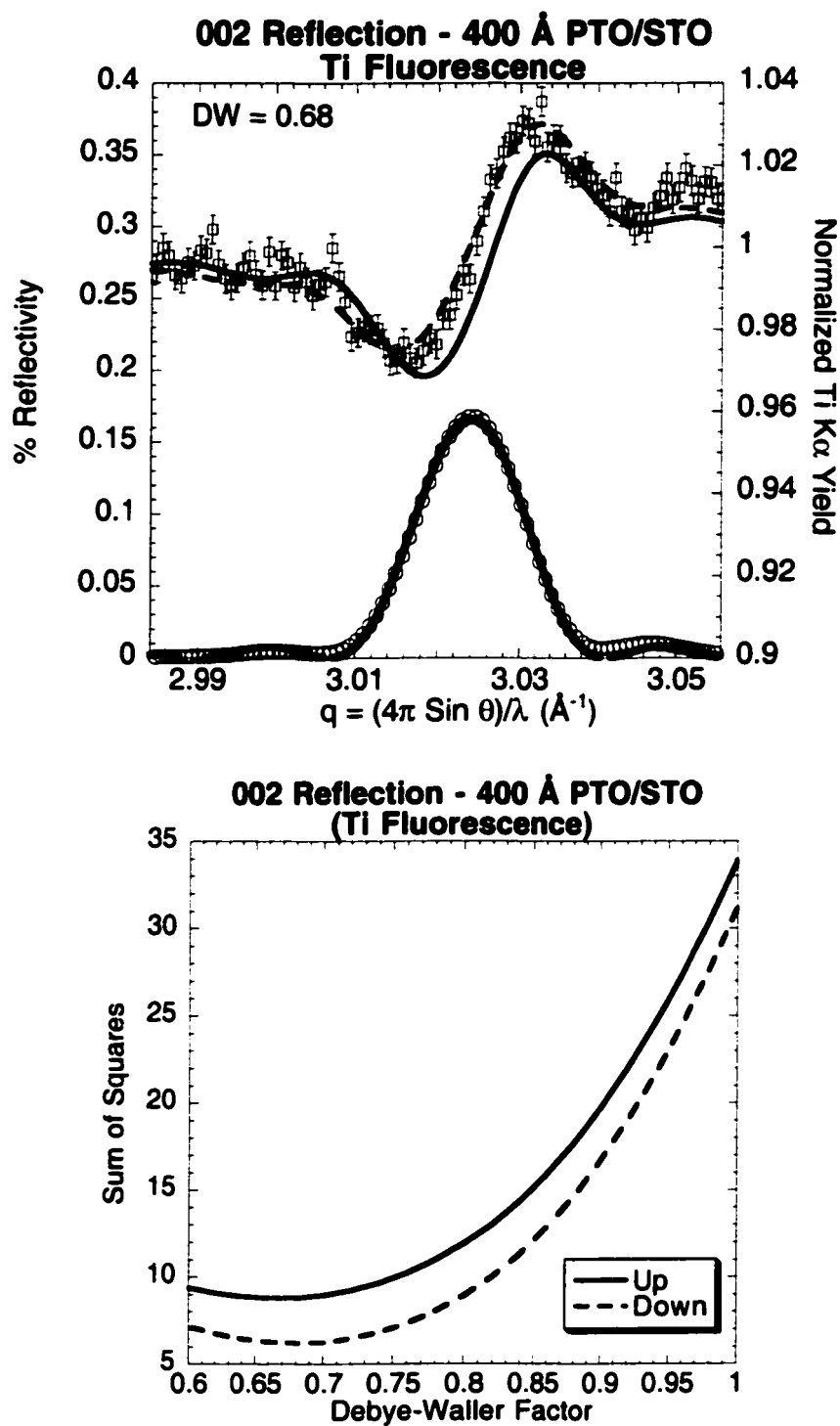


Figure 6.3.10 400 Å film (002) reflection at 8.0 keV for Ti fluorescence. The film is in the down orientation.

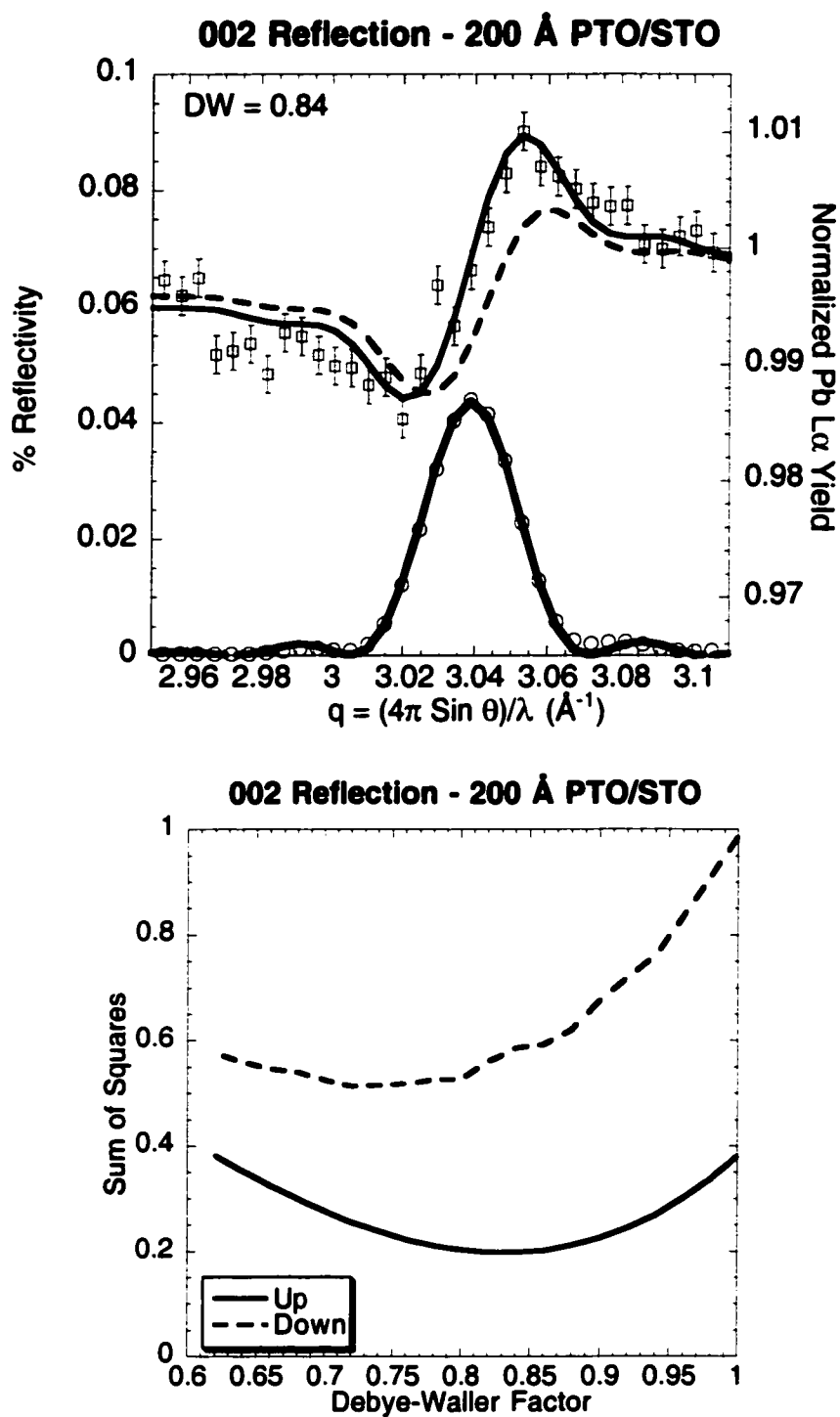


Figure 6.3.11 200 Å film (002) reflection. The film is in the up orientation.

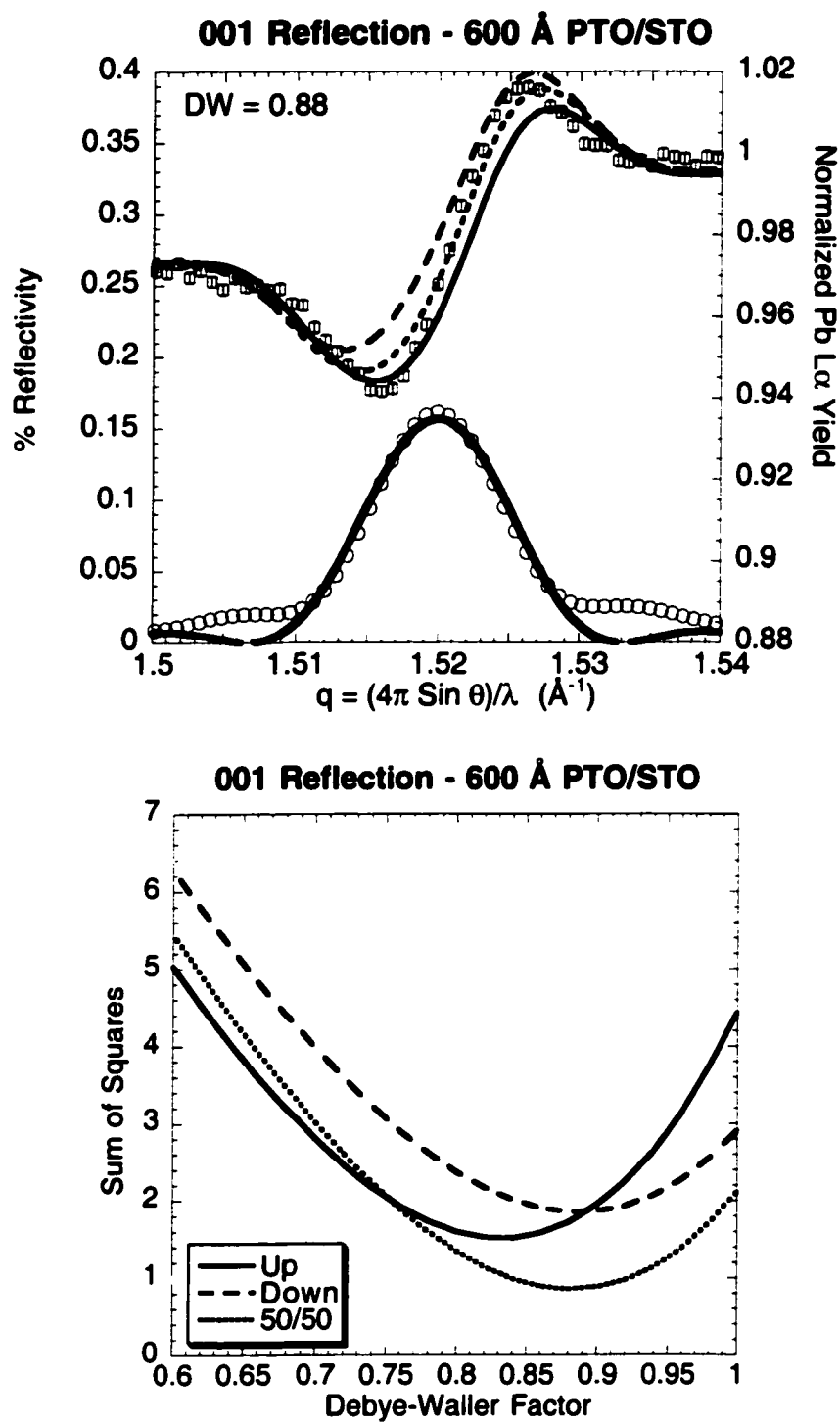


Figure 6.3.12 600 Å film (001) reflection. The best fit is a 50%-50% mix between the up and down orientations. Note the poor match between the reflectivity data (open circles) and the fit (solid line).

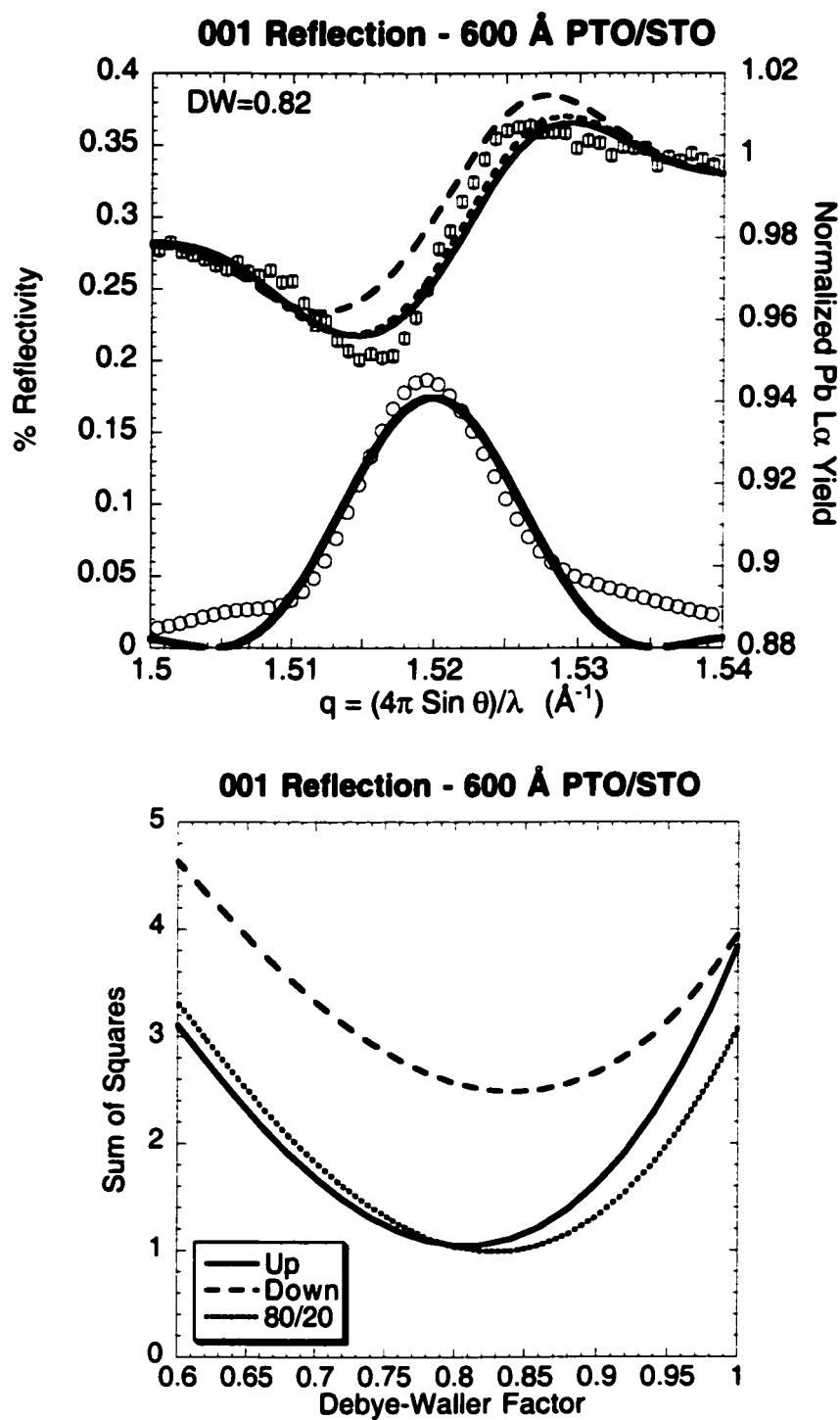


Figure 6.3.13 600 Å film (001) reflection. The best fit reflects an 80% up – 20% down mixture. Note the poor match between the reflectivity data (open circles) and the fit (solid line).

6.4 PbTiO₃ Crystal Truncation Rod Measurements

6.4.1 PbTiO₃ 100 Å CTR Experimental

Crystal truncation rod (CTR) measurements on the 100 Å PTO film were performed in January of 1998. The sample was mounted with a vacuum chuck on the four-circle diffractometer at the 12ID-D beamline at the Advanced Photon Source. The energy of the incident beam was tuned to 13.5 keV by the upstream LN₂-cooled high heat load Si(111) monochromator. Once a good substrate peak was found, the SPEC software that controls the diffractometer and detectors was operated in a mode where the reflection could be scanned in reciprocal space. The quantities h, k and l are in units based on the substrate STO reciprocal lattice. With h set to zero, k scans were made at selected values of l near $l = 1$. The results of the k scans revealed the location of the CTR in reciprocal space, see Fig. 6.4.1. A series of hkl scans, with different thicknesses of aluminum foil

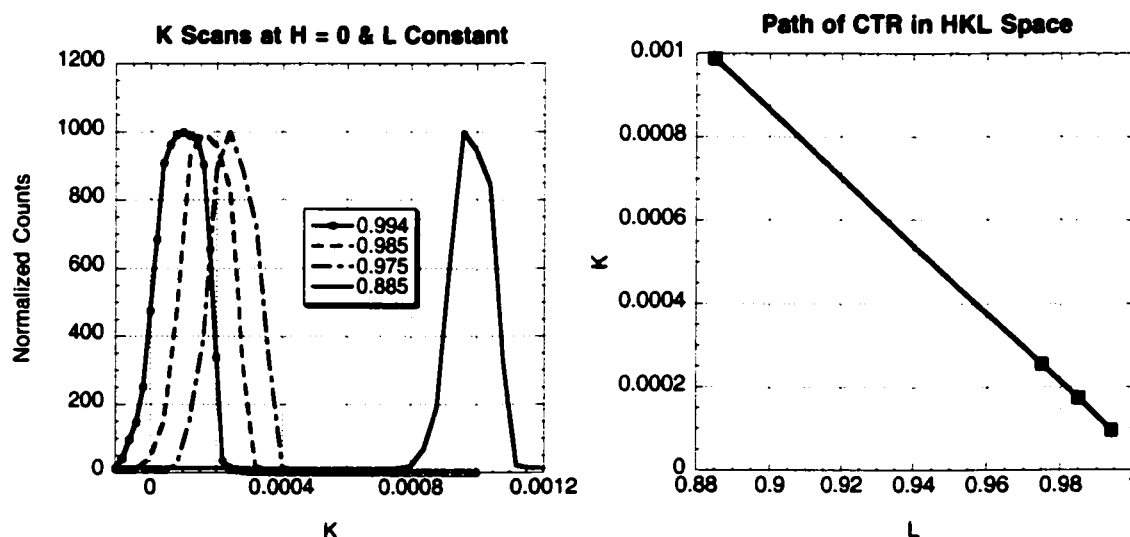


Figure 6.4.1 Determination of the CTR in reciprocal space. After carefully aligning the STO substrate with respect to the beam, k scans were performed at four l values. The center of the peaks in the k scans revealed the location of the CTR. The CTR data were taken on this path in hkl space.

acting as attenuation filters, was used to collect the CTR data from $q = 1.15$ to 1.76 \AA^{-1} .

A pair of background scans was performed at $k \pm 0.001$. These background scans, along with a dark current correction, were subtracted from the CTR data.

The orientation of the CTR rod in reciprocal space is directly related to the miscut of the crystal. The path in reciprocal space was determined to be $k = (1-l) (0.0086)$ by observing the shift of the rocking curve in k space as l was decreased. The angle of miscut from the CTR measurement corresponds to $\arctan(0.0086) = \alpha = 0.49^\circ$. This is close to the experimentally measured miscut of 0.65° , determined by leveling the crystal surface with respect to the beam and then finding the location of the $\text{STO}(001)$ Bragg peak. Following Nagai's work for describing strain relief at a miscut stepped interface [12], this would result in a misalignment between the c -axis directions of the STO substrate and the PTO film of $\gamma \sim 0.03^\circ$ (see Fig 6.4.2).

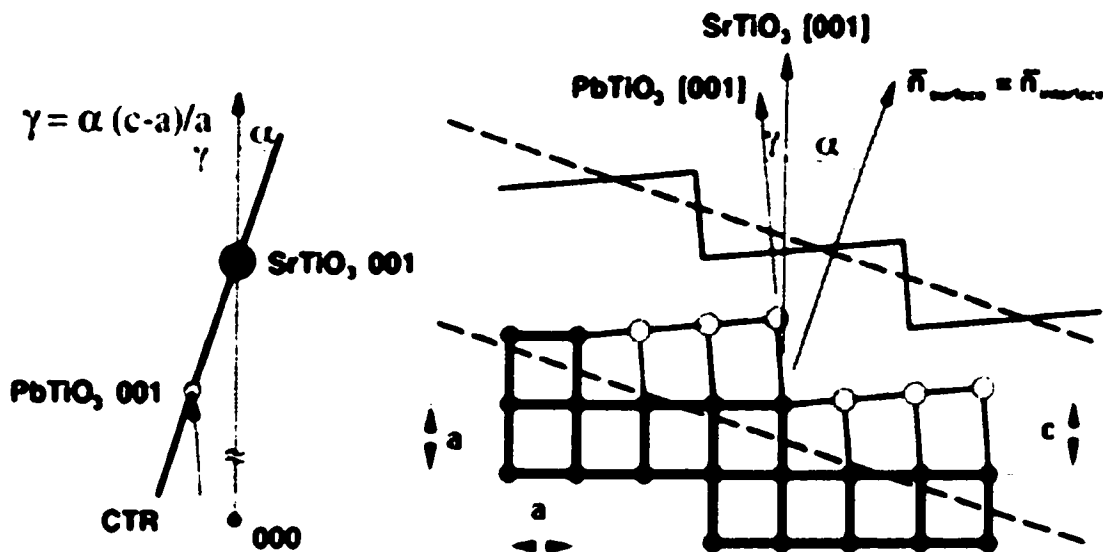


Figure 6.4.2 The relationship between the miscut angle α of the sample surface normal with respect to the substrate (001) vector, the path of the CTR in reciprocal space and the misalignment angle γ between the film and sample lattice.

6.4.2 Results for the CTR Scan of the 100 Å PbTiO₃ Film

The 100 Å PTO/STO (001) CTR data were fit to equation [3.5.5] both over the $q = 1.15$ to 1.76 Å^{-1} range and also from $q = 1.49$ to 1.65 Å^{-1} . The fitting parameters are summarized in Table 6.4.1. The data with the best fit are shown in Figures 6.4.3 and 6.4.5.

The CTR method is very sensitive to the offset between the film and the substrate in the region of the scan where the reflected amplitude from the film and substrate are of comparable strength and therefore can appreciably interfere with each other. Figure 6.4.4 shows the large variation with δ . However, over the wide range of the data taken, since the interference is strong only in the narrow region near the substrate peak, fitting over the entire range may generate a poor result for the value of the offset. To check for this possible problem, a smaller range of data was fit, from $q = 1.49$ to 1.65 Å^{-1} ; this covers the substrate peak, the main film peak, and the first film thickness fringe to the high-angle side of the substrate peak. In this narrower range, the effect of the offset is more pronounced on the fitting. The result was nearly identical to that of the fit over the

Table 6.4.1 Fitting parameters used for fitting equation [3.5.5] to the CTR data of the 100 Å PTO film. The substrate and film roughness are accounted for by σ_s and σ_f , respectively. The quantity δ is the fractional film unit cell offset between the film and the substrate. The lattice parameter of the film is c , and the mean thickness and standard deviation in mean thickness are designated as N and σ_N . R_{scale} is an overall scaling factor to match the data to theory. The quantity %Up is a user-set constant reflecting the fraction of the film that is in the up orientation. For more details, see Section 3.5 and the Appendix.

<i>Range</i>	$\sigma_s (\text{Å})$	$\sigma_f (\text{Å})$	δ	$c (\text{Å})$	N	σ_N	R_{scale}	%Up
1.15-1.76	3.9	6.3	-0.15	4.135	23.5	0.40	9.748e10	100.

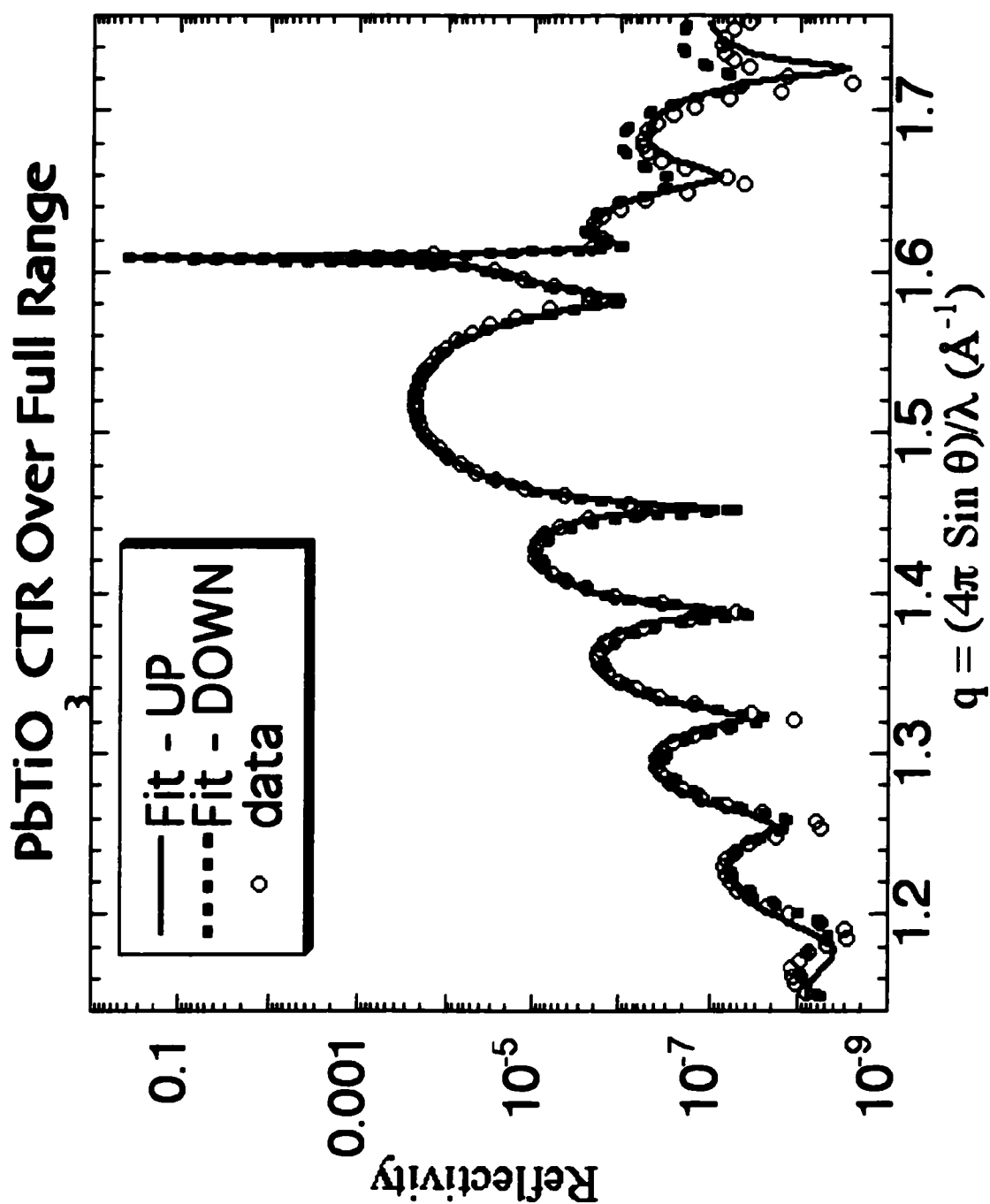


Figure 6.4.3 CTR scan of the PTO/STO (001) system at 13.5 keV, over the full range of the scan. The spike is due to the STO(001) Bragg peak, and the broad peak at $q = 1.52 \text{ \AA}^{-1}$ is due to the PTO film. The thickness fringes surrounding the PTO peak are a result of the 100 \AA film.

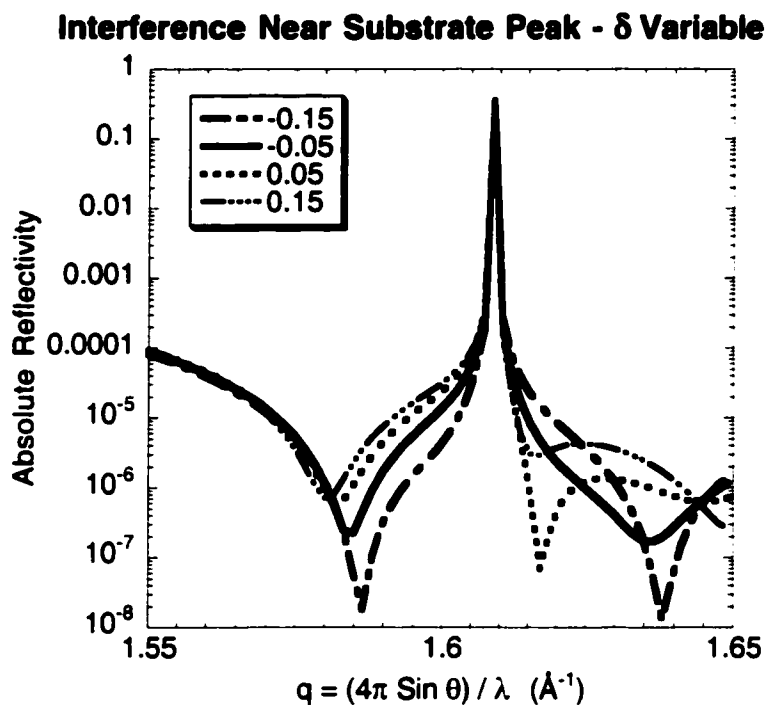


Figure 6.4.4 Simulation using equation [3.5.5] showing the δ dependence of the interference in the PTO/STO CTR near the STO (001) peak. δ values of -0.15 , -0.05 , 0.05 , 0.15 were used.

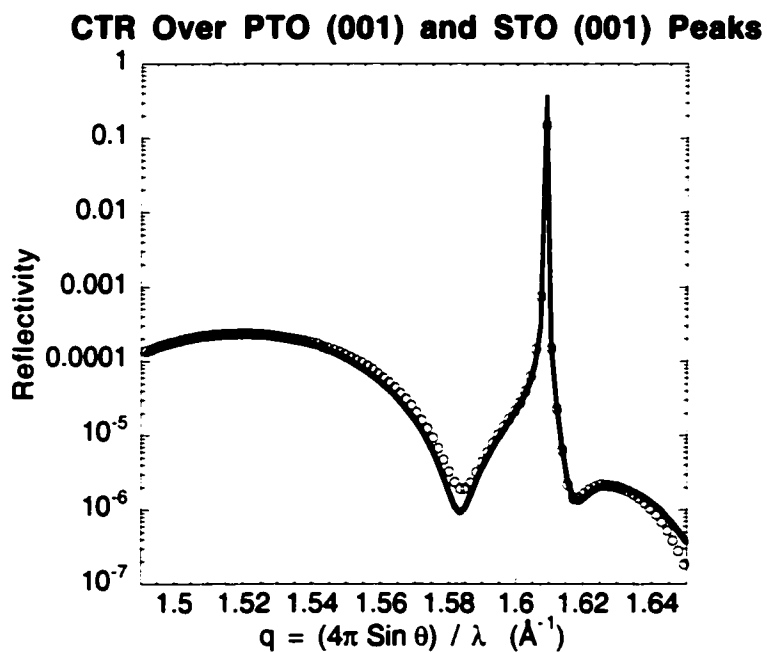


Figure 6.4.5 CTR scan of the PTO/STO (001) system at 13.5 keV, in the region of interference between the PTO and STO (001) peaks.

larger range, with an offset of -0.151 PTO unit cells. The fit over the smaller range is shown in Figure 6.4.4.

For the best fit with a down-polarized film, the offset was $\delta = 0.133$ unit cells; for an up solution, the offset was $\delta = -0.151$ unit cells. The shift in offsets is easy to understand when the details of the amplitude reflectivity are examined. The substrate term is multiplied by an exponential that affects both the phase due to the offset in the lattice and the amplitude due to absorption. Ignoring absorption, the term in the exponential goes as $-iq c (N+\delta)$ (eq. [3.5.5]). At the film peak, the quantity $q c$ is equal to exactly 2π , and varies linearly in q away from the peak. The exponent can then be approximated as $2\pi i (N+\delta)$. As N is always an integer, the phase is $2\pi i \delta$. The phase of the structure factor of the up polarized film is 0.367π radians, and the phase of the structure factor of the down polarized film is -0.237π radians. The difference between the two is 0.604π radians. The difference between the offsets is 0.284 unit cells; when multiplied by 2π , this gives a result of 0.568 radians, a close match to the phase difference between the two structure factors. This is no surprise, as the fitting routine's main mechanism for matching phase is the offset. Therefore to account for the different phases in the two structure factors, the relative difference is reflected in the offset. While the fit for the down polarized film is not as good as the fit for the up polarized film, the shift of Pb^{2+} and Ti^{4+} ions between the up and down cases is partially balanced in the fitting by a shift in δ . Figure 6.4.6 shows a side view of the structures fit for the up and down polarities. Note how similar the position of the Pb^{2+} ions are between the two

cases. This points to the importance of having XSW data to determine the polarity of the film in a way that is insensitive to δ .

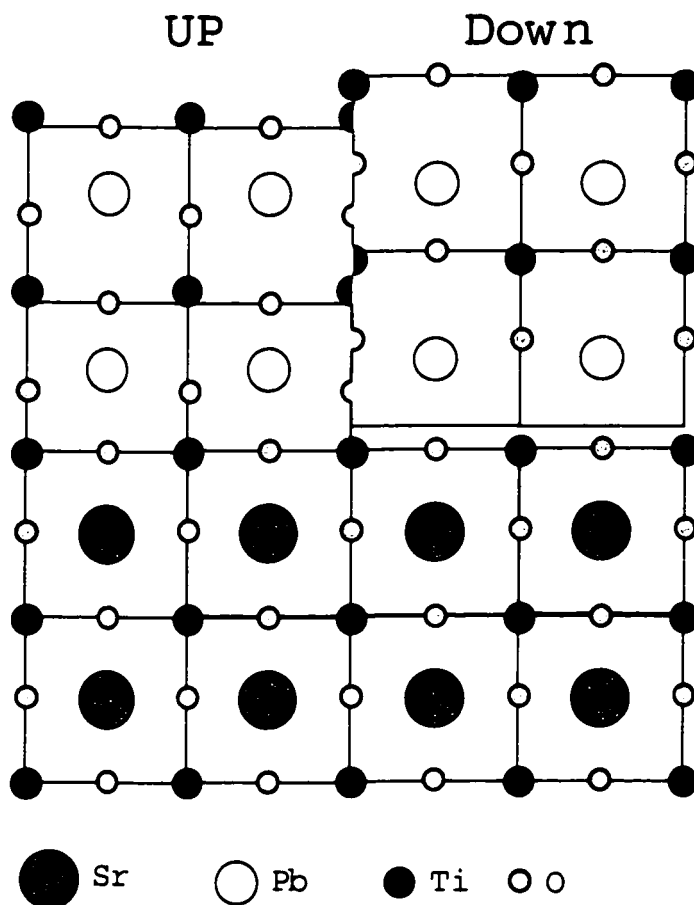


Figure 6.4.6 – Side view lattice depiction for the best-fit up and down orientations of PTO/STO(001) from CTR measurements. The up oriented lattice is shifted down toward the substrate STO(001) crystal by 0.151 PTO unit cells, the down oriented lattice is offset upward by 0.133 PTO unit cells. This is to account for the difference between the phases of the structure factors of the up and down film polarities. Note that in both cases the high-electron density (001) Pb planes take nearly the same position relative to the STO lattice.

6.5 Discussion of X-ray Measurements of the PTO/STO System

The thin-film XSW method was successfully employed to probe the polarity of ferroelectric films. The 100, 200 and 400 Å films favored uniform film polarity in one direction; 10 out of 11 reflections fit either 100% up or 100% down. This is true over large regions, as the x-ray probed the 0.4 mm x 1.6 mm footprint on the sample surface. In comparison, Sakashita grew PZT thin films via MOCVD, with compositions including the degenerate case of PTO. Sakashita's 2 micron thick samples had micron-sized grains [13].

The crystal quality of the films grown up to 400 Å was very high based upon inspection of the reflectivity data. Thickness fringes in both the XSW scans and the more reflectivity-sensitive CTR measurements attest to the uniformity of the film. This is consistent with the finding that the formation of 90° rotated *a*-type domains is suppressed below a critical thickness of 500-700 Å [9]. If the films did contain *a* domains, their contribution to the fluorescence signal would follow $1 + R$ behavior, essentially a flat background because of the small values for *R*, and would act to lower the measured static Debye-Waller factors; instead, the static Debye-Waller factors were generally fairly high. The film roughness, as measured by CTR, corresponds to roughly one and a half unit cells. The CTR measurements also show a uniform film thickness.

For the most part, the films up to 400 Å were oriented in the up direction (9 out of 11 cases). This is an interesting result, as the PTO film is grown at 700° -750°C, well above the transition temperature for bulk PTO (490°C) [1]. As the film cools, it undergoes a structural transition from the centrosymmetric paraelectric phase to the room-

temperature ferroelectric phase. The preferential growth of the up orientation may be due to many factors. One variable is the top surface of the STO substrate. The termination of the substrates is 75%-98% TiO_2 [14]; future studies with controlled STO surfaces should provide insight into the effect of the top layers of the substrate on the as-grown orientation of the film.

With the Ti $K\alpha$ fluorescence data, it is interesting to note that the modulation in the signal is nearly counter-phase to the Pb $L\alpha$ signal at the PTO(001) reflection. This is due to the approximately $d_{001}/2$ separation between the Ti and Pb atomic planes in the PTO unit cell. As shown by Bedzyk and Materlik [15], the XSW phase is linked to the phase β_H of the structure factor F_H . The diffraction planes themselves are located at the position where the real part of the hkl Fourier component of the scattering density is a maximum. As the film is rocked through the PTO(001) reflection, the XSW antinodes move inward by $d_{001}/2$ from a position halfway between the diffraction planes on the low angle side of the reflection to the diffraction planes on the high-angle side. As can be seen in Figure 6.5.1, the diffraction planes, and therefore the XSW antinodes on the high-angle side of PTO(001), are nearly coincident with the position of the Pb atomic planes. Hence, in a measurement of Pb fluorescence at the PTO(001) reflection, a dip followed by a peak is expected. As the Ti atomic plane is out of phase with the Pb plane by nearly π , the opposite behavior can be expected from the Ti fluorescence. In the case of the PTO(002) reflection, the diffraction planes are nearly coincident with both the Pb atomic planes and the Ti atomic planes, and the antinodes will travel from a point roughly halfway between the Pb and Ti atomic planes to roughly on top of the atoms. Hence the

modulation in the fluorescence in the PTO(002) reflection will be roughly in phase, rather than counter-phase as is the case for the PTO(001) case. In addition, note that in the down orientation the XSW antinodes actually intersect the Pb atomic plane, whereas this is not the case in the up orientation. This is accounted for in the fluorescence modulation, the Pb signal on the high-angle side of the rocking curve is stronger in the down oriented case than it is in the up case. See Figure 6.3.3 as an illustration. The opposite is true in

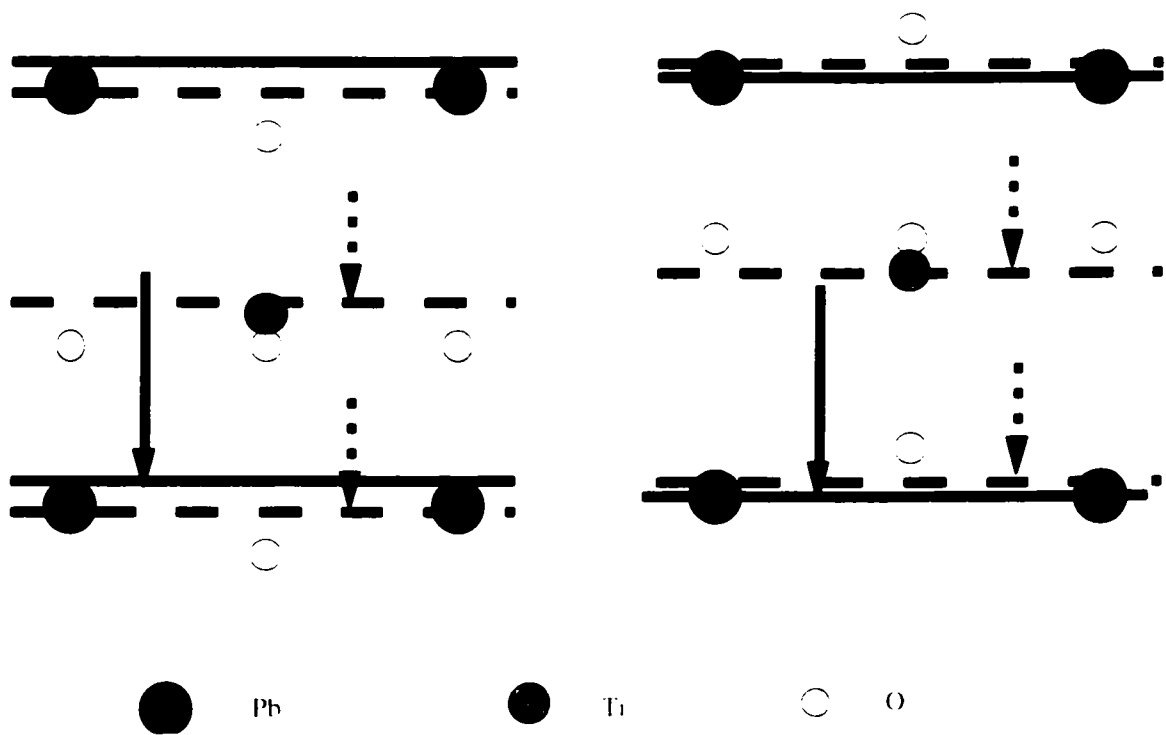


Figure 6.5.1 Side view of PbTiO₃ structure. On the left side is the unit cell atom arrangement in the up orientation, with the Pb and Ti ions displaced from the O sublattice along the positive c direction. The right shows the crystal in the down orientation. The solid line represents the position of the diffraction plane in the (001) PTO reflection, and the dashed, the (002) reflection. The solid and dashed arrows trace the movement of the XSW antinodes through the unit cell in the (001) and (002) reflections, respectively. The positions of the (00 l) diffraction planes are determined from phases of the respective (00 l) PTO structure factors.

the (002) reflection, as shown by the dashed lines representing the (002) diffraction planes in Figure 6.5.1 and the behavior of the fluorescence signal as shown in Figure 6.3.4. The reason that the (00 l) diffraction planes do not have the same mirror symmetry as their respective lattices is due to anomalous dispersion.

The thicker 600 Å film displayed both poor rocking curves and a mix of up and down orientations. Note the poor agreement between the reflectivity data and the fit in Figures 6.4.12 and 6.4.13. This suggests mosaic spread in the film, the beam sampling from regions that are either slightly tilted from one another or have slightly different c -axis lattice parameters. One measurement displays an even 50%-50% mix of film orientations, and the other exhibits an 80%-20% mix. The 600 Å films are in the range where a domain formation starts to occur. The Debye-Waller factor for the second reflection measured is rather low, possibly due to the inclusion of a domains, although an explanation as to why one region has more a domains than the other is difficult to explain. As the inclusion of a domains is a strain-reducing mechanism, perhaps the defects found in the 50%-50% mix of orientations allows for some reduction in the strain of the film.

Chapter 7 Thin-Film X-ray Standing Wave Measurements of MOCVD-Grown $\text{Pb}(\text{Zr}_{0.3}\text{Ti}_{0.7})\text{O}_3$ / SrTiO_3

7.1 PZT Capacitor Structure and Growth

With the success of the thin-film XSW method in analyzing the as-grown polarity of PTO films grown on $\text{STO}(001)$ substrates, the next step was to apply the technique to ferroelectric films grown in a capacitor structure (Fig 7.1.1) in order to study the effects of electrical switching on the film.

In order to promote high-quality single-crystal ferroelectric film growth and to provide for a bottom electrode in the capacitor structure, an epitaxial 1360 Å layer of SrRuO_3 (SRO) was rf-magnetron sputter-deposited at 680°C on the single-crystal SrTiO_3 substrate by C.-B. Eom and R. A. Rao at Duke University [1]. By design, the substrate was miscut at 1.9° from (001) and 12° from the in-plane [010] direction in order to promote highly ordered tetragonal growth of the orthorhombic SrRuO_3 [2]. The SRO film is pseudocubic with an out-of-plane lattice parameter of 3.96 Å, as compared to a lattice constant of 3.905 Å for STO [1].

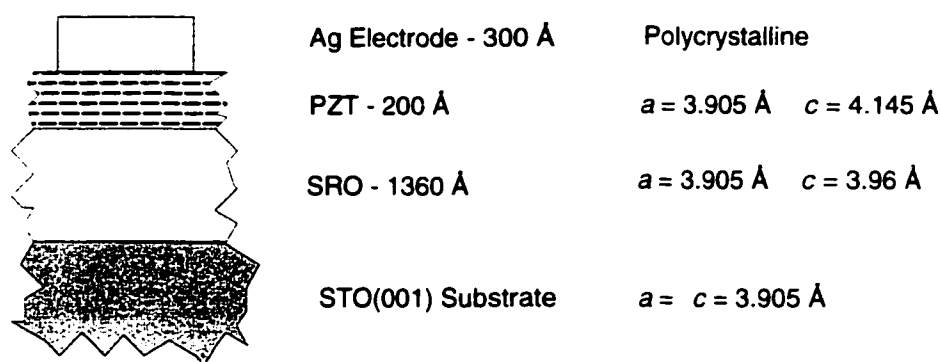


Figure 7.1.1 A side view depiction of the PZT capacitor heteroepitaxial structure. Out-of-plane lattice constants were determined by diffraction (see Fig. 7.4.1).

The ferroelectric film in question was a 200 Å thick epitaxial $\text{Pb}(\text{Zr}_{0.3}\text{Ti}_{0.7})\text{O}_3$ (PZT) (001) film grown at 700°C by MOCVD. The metal ion precursors used were tetraethyl lead, $\text{Pb}(\text{C}_2\text{H}_5)_4$, zirconium *t*-butoxide, $\text{Zr}[\text{OC}(\text{CH}_3)_3]_4$, and titanium isopropoxide, $\text{Ti}[\text{OCH}(\text{CH}_3)_2]_4$. The precursor temperatures were 28.5°C, 32°C and 32°C respectively; the precursor pressures were 400, 80 and 100 Torr, respectively. The precursor gases were carried to the reactor chamber by N_2 in heated lines in order to prevent condensation; the flow rate of the Pb mixture was 35 sccm, the reactant O_2 300 sccm, and the flow rate of the Ti and Zr gases totaled 60 sccm. The reactor pressure was 5-6 Torr, and the substrate temperature was 700°C. The growth rate of the film was 25-50 Å/min [3].

As a bulk crystal, above 425° PZT is a centrosymmetric perovskite, as can be seen in the phase diagrams in Figure 7.1.2. The O^{2-} ions sit at the face-centered positions, the

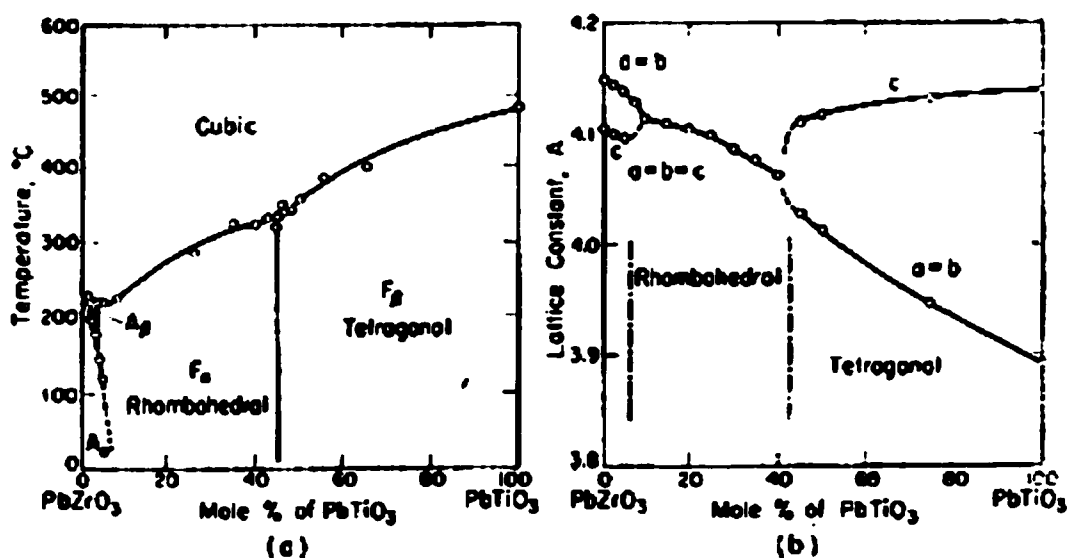


Figure 7.1.2 PZT phase diagrams from Jona and Shirane [1]. Below 425°C, a 30% Zr-70% Ti mix is tetragonal .

Pb^{2+} ions occupy the corners, and the $\text{Zr}^{4+}/\text{Ti}^{4+}$ ions are at the body-center site. When PZT is cooled below 425°C it undergoes a phase transition; the Pb^{2+} ions remain at the corner sites, but the O^{2-} and $\text{Zr}^{4+}/\text{Ti}^{4+}$ sublattices are shifted slightly along the elongated c -axis. The fractional displacement of the oxygen sublattice is 0.112 unit cells, and the Ti sublattice is displaced by 0.039 unit cells in the opposite direction. This generates a net electrical polarization [4].

Polycrystalline 300 Å thick Ag top electrodes were electron-beam evaporated through a shadow mask onto the surface of the continuous PZT film, thus defining capacitor structures. See Figure 7.1.3 for a map of the top electrodes.

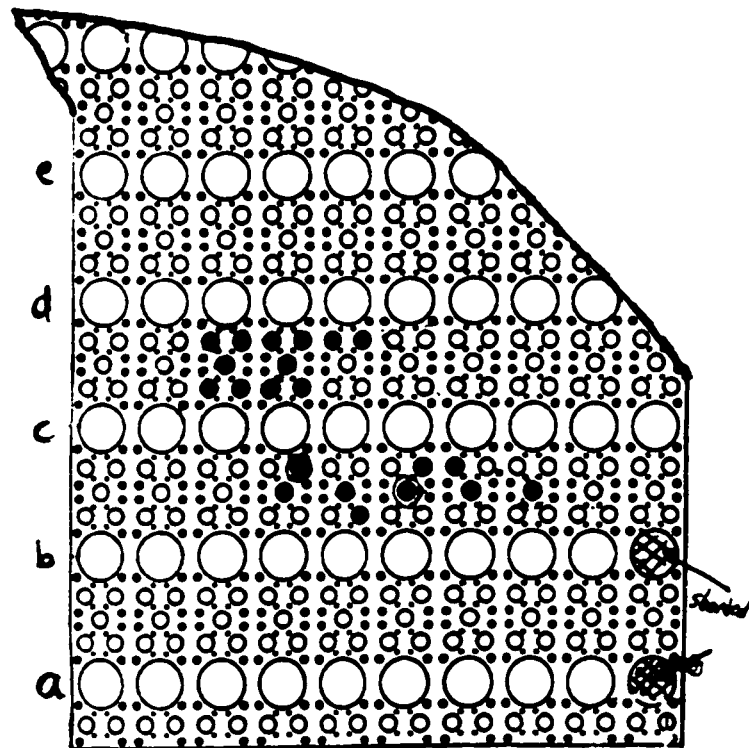


Figure 7.1.3 Map of the sample. The large pads are 0.75 mm in diameter; a pair was shorted through to the SRO lower electrode in order to perform electrical measurements. Several of the smaller 0.25 mm pads were poled in either the up or down direction. The poled pads are marked in black on this map.

7.2 Experimental Setup for PZT/SRO/STO(001) XSW Measurements

The Ag/PZT/SRO/STO(001) capacitor structures were tested electrically for their ferroelectric properties. To perform these tests, a pair of the large 0.75 mm diameter Ag pads were shorted through the PZT to the bottom SRO electrode. One test lead was put into contact with one of the shorted pads, and the circuit was completed with a test lead in contact with one of the medium-sized 0.25 mm Ag pads. The electrodes were connected to a function generator, and were monitored by a current amplifier. In order to observe switching, selected pads were cycled with 1 kHz triangle waves with amplitudes varying from 1.0 to 1.8 Volts, depending on the electrical properties of the capacitor. If the capacitor exhibited switching behavior, it was driven to saturation by triangle waves in the proper direction; most were poled at 1.8 Volts. As polarization is a measure of switched charge, the output of the current amplifier is integrated in order to obtain polarization. Figure 6.2.1 shows polarization versus voltage hysteresis loops for two of the capacitors. One of the loops is not symmetric about the zero-voltage axis. This suggests that there is a “hard” and an “easy” polarization state for this capacitor. This is known as imprint and is discussed later below conjunction with the thin-film XSW results.

The capacitors were examined via thin-film XSW at the 5-ID-C beamline in September of 1998. Initially, attempts were made to measure the Zr K fluorescence. The Zr K α peak was at 15.7 keV and could not be separated from the Sr K β peak from the substrate at 15.8 keV. Fluorescence slits were used to reduce the signal from the

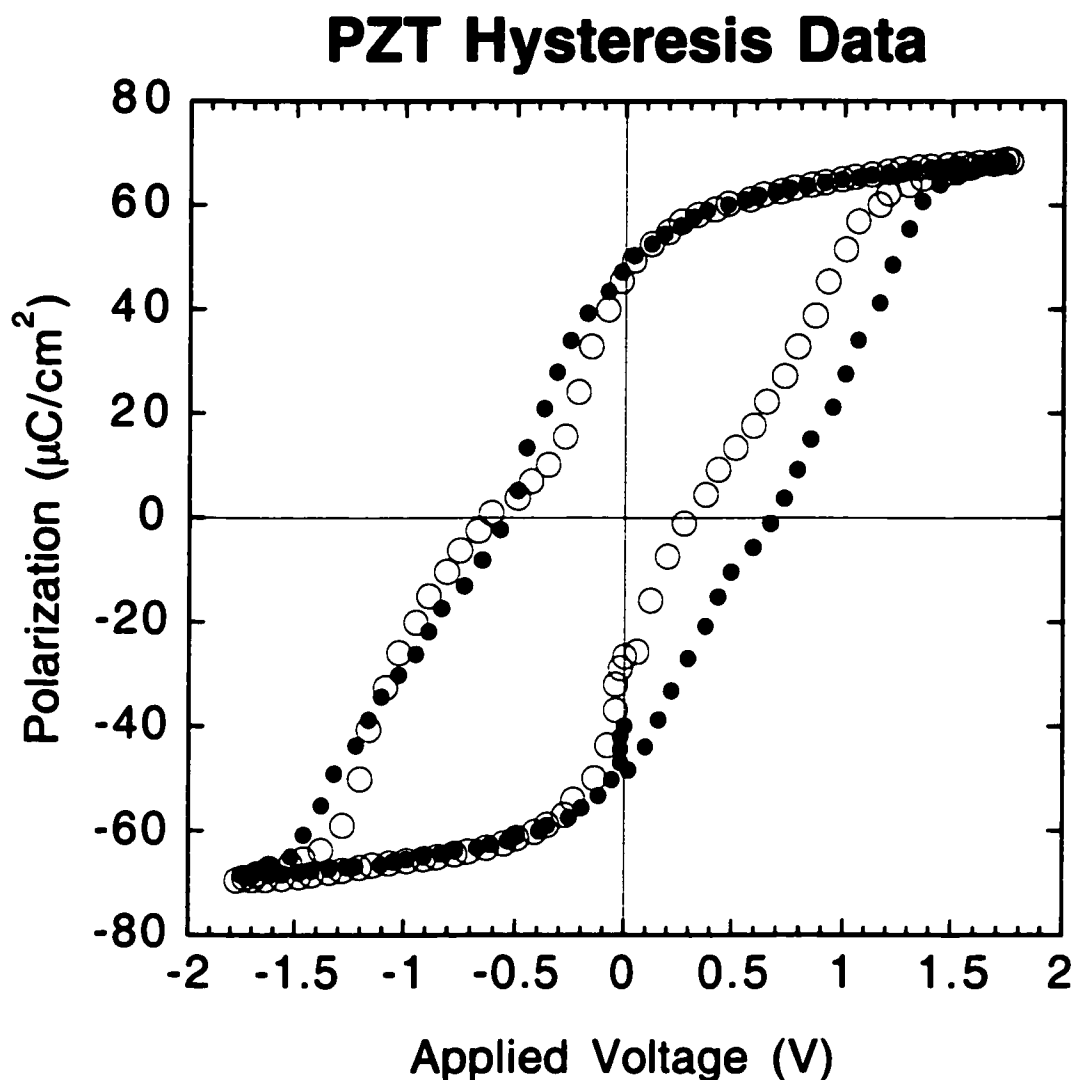


Figure 7.2.1 Polarization vs. voltage hysteresis loops for two capacitors. Note that while one loop is symmetric about zero volts, the other is shifted slightly in the negative direction. This suggests imprint.

substrate, but the count rate from the film was too low to gather proper statistics for the measurement. The Zr $K\beta$ was at 17.7 keV, but the DND upstream monochromator could not deliver an energy high enough to separate the TDS peak from the Zr signal. Instead, the beam was set to 13.5 keV, and the Pb $L\alpha$ peak was observed. See Figure 7.2.2 for the

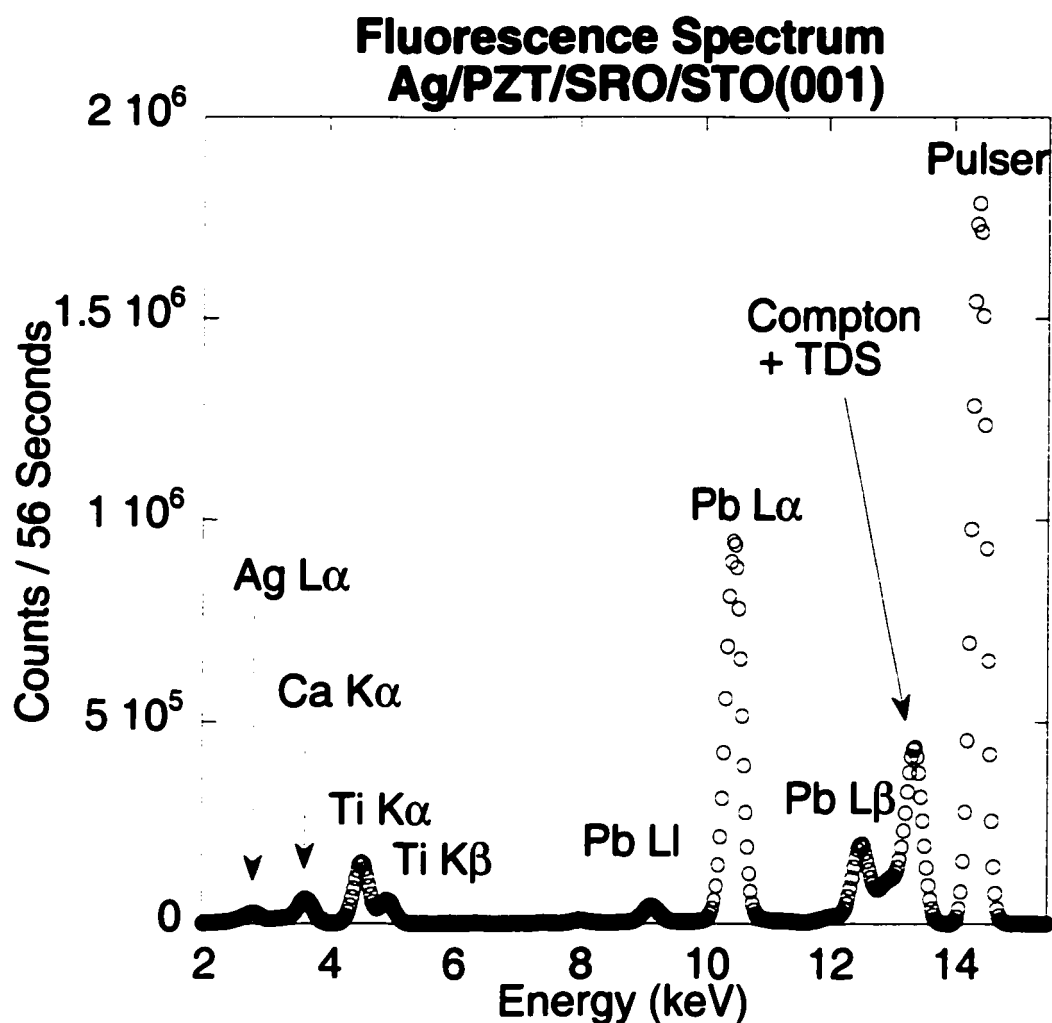


Figure 7.2.2 Fluorescence data collected by the Si(Li) detector for the PZT ferroelectric capacitor structure.

fluorescence spectrum from the sample. At 13.5 keV, the Bragg angle was 6.75° , and due to the sample's 1.9° miscut, the actual angular position of the sample was 8.65° .

The Ag pads that defined the top surface of the capacitor were $250 \mu\text{m}$ in diameter, so the beam was slitted to $180 \mu\text{m} \times 20 \mu\text{m}$ to form a $180 \mu\text{m} \times 240 \mu\text{m}$ long x-ray footprint on the surface of the capacitors. The output pulses of the fluorescence detector spectroscopic amplifier were cascaded through a series of single channel

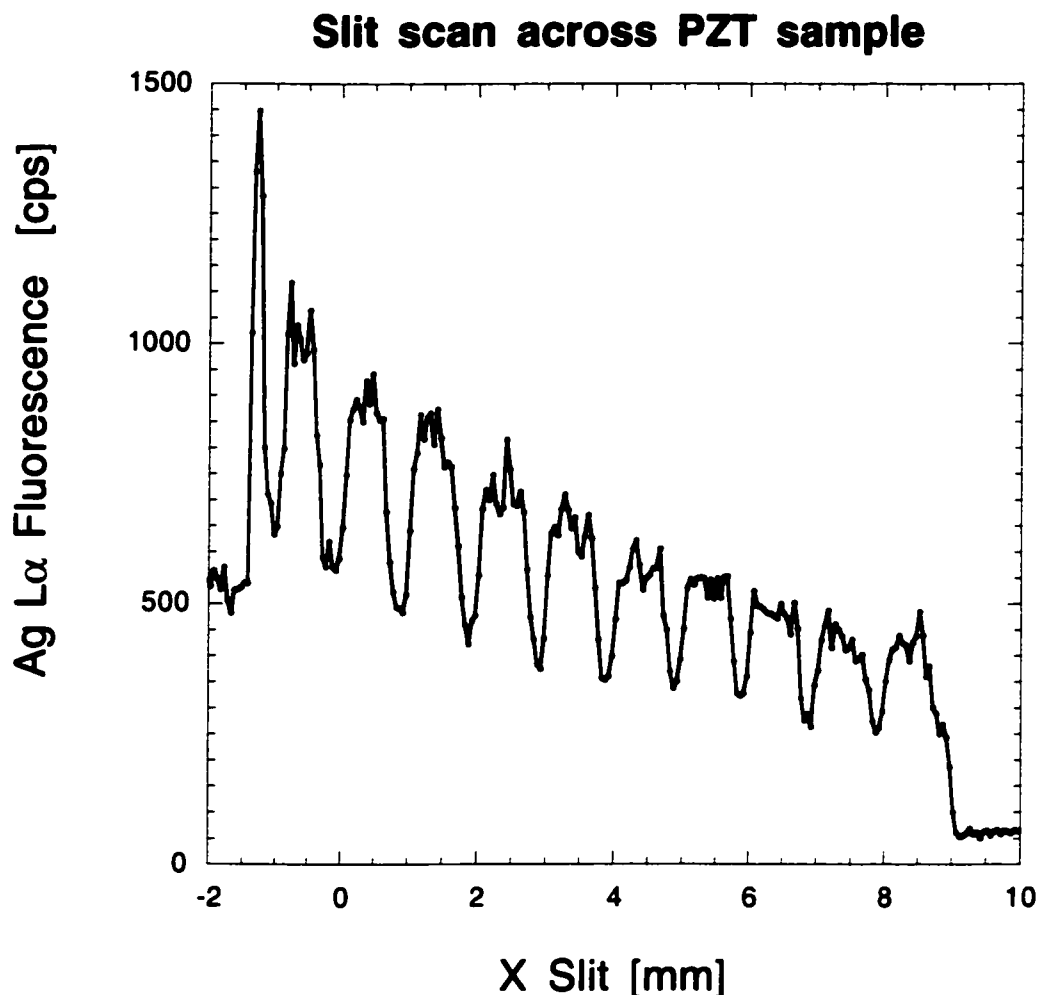


Figure 7.2.3 Output of the single channel analyzer tuned to Ag L fluorescence. The peaks in the scan correspond to the Ag top electrodes of the capacitors on the sample.

analyzers (SCAs). The SCAs allowed for the direct observation of the Ag $L\alpha$ and Pb $L\alpha$ signals as real-time counts per second. Using the motorized x motion on the defining incident beam slit and the SCA output, we were able to scan across the sample and observe the Ag $L\alpha$ signal. See Figure 7.2.3 for a sample output of a scan. The large 0.75 mm Ag pads are clearly visible as peaks on the output. The 10 peaks correspond to the 10 pads across the sample (Fig. 7.1.2). The height of the peaks decreases as the beam moves away from the fluorescence detector. By using this method, we determined our

exact position on the sample. This allowed placement of the beam centered directly on the desired 0.25 mm capacitors. We measured four of the previously poled capacitors: D3M2 and D4M2, which had been poled up, and D2M0 and D2M2, which had been poled down.

7.3 XSW Results for PZT Capacitor Structures

XSW data were collected for four capacitor structures: two poled in an up orientation and two poled in a down orientation. The rocking curves and Pb L α fluorescence were fit using a modified version of the Takagi-Taupin software used for fitting the PTO data. The software modeled the capacitor interface as follows. The SrTiO₃ substrate was treated as a centrosymmetric cubic crystal with a lattice spacing of 3.905 Å. An extra iteration in the reflectivity calculation was included to account for the SRO buffer; it was treated as a tetragonal crystal with an in-plane lattice constant matched to the substrate and an out-of-plane lattice constant of 3.960 Å. The tetragonal PZT layer was modeled as having an out-of-plane lattice constant of $c = 4.145$ Å. The c -axis lattice parameters were extracted from the position of the respective peaks in the reflectivity scans, see Figure 7.3.1. The bulk PTO fractional sub-lattice displacements of the ions (section 6.1) were used for the PZT case; this is a reasonable approximation given the accuracy of the XSW measurement, taking into account the PZT cell distortion induced by epitaxial strain. This model was used to calculate the expected fluorescence yield and reflectivity for six different cases, corresponding to film orientations of 100%, 80%, 60%, 40%, 20% and 0% in the up direction. In addition, a 50% fit was performed for a reflection that

showed a best fit of 40%. These cases were fitted to the data with the static Debye-Waller factor as a free parameter, using a chi-squared minimization algorithm.

Of the two samples poled in the up orientation, only one was measured as up; it best fit with a static Debye-Waller factor of 0.76. The other up capacitor best fit as a 40% up – 60% down mixture with a static Debye-Waller factor of 0.84. The two capacitors poled in the down orientation were measured in the down state. One best fit a 20% up – 80% down mixture with a static Debye-Waller factor of 0.70, and the other best fit a pure down state with a static Debye-Waller factor of 0.90. XSW data, sum of squares, and electrical polarization hysteresis data for the four capacitor structures are summarized in Figures 7.3.2 through 7.3.5.

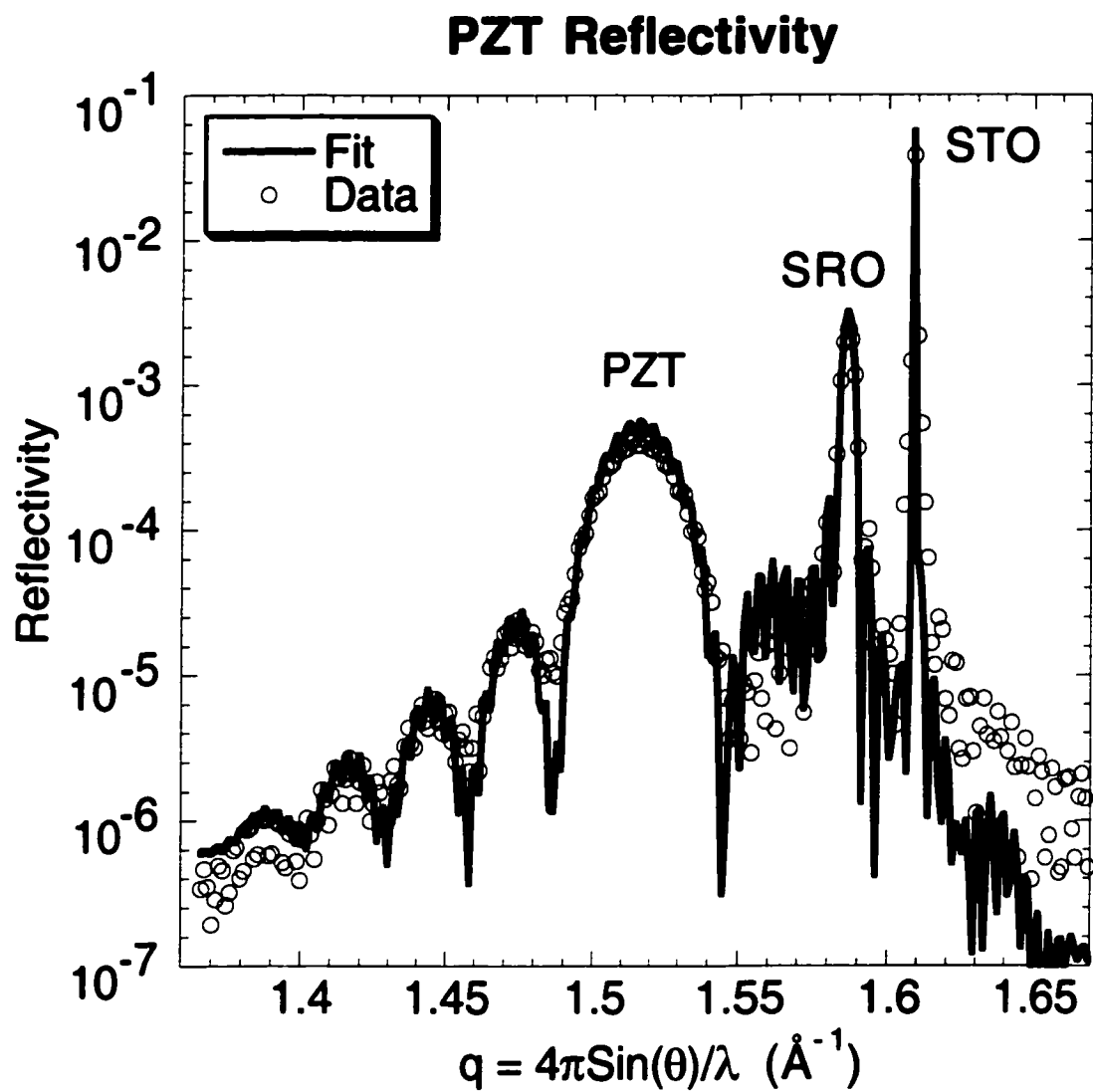


Figure 7.3.1 Theta - Two Theta scan of capacitor pad D4M2. From low to high angle, the three peaks correspond to PZT (001), SRO (001) and STO (001), respectively.

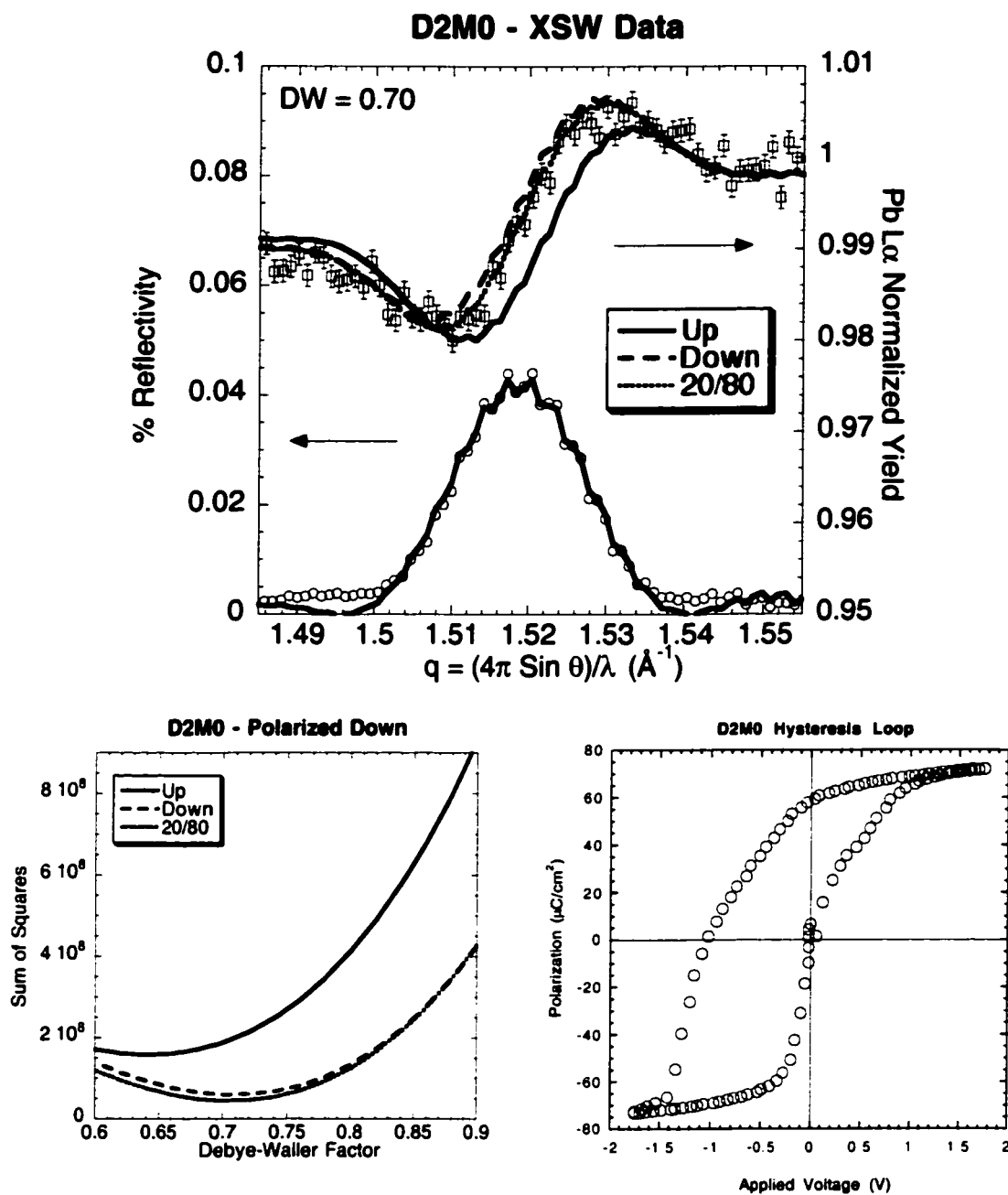


Figure 7.3.2 Capacitor D2M0: poled in the down orientation. Best fit by 20% Up - 80% Down mixture with a Debye-Waller factor of 0.70.

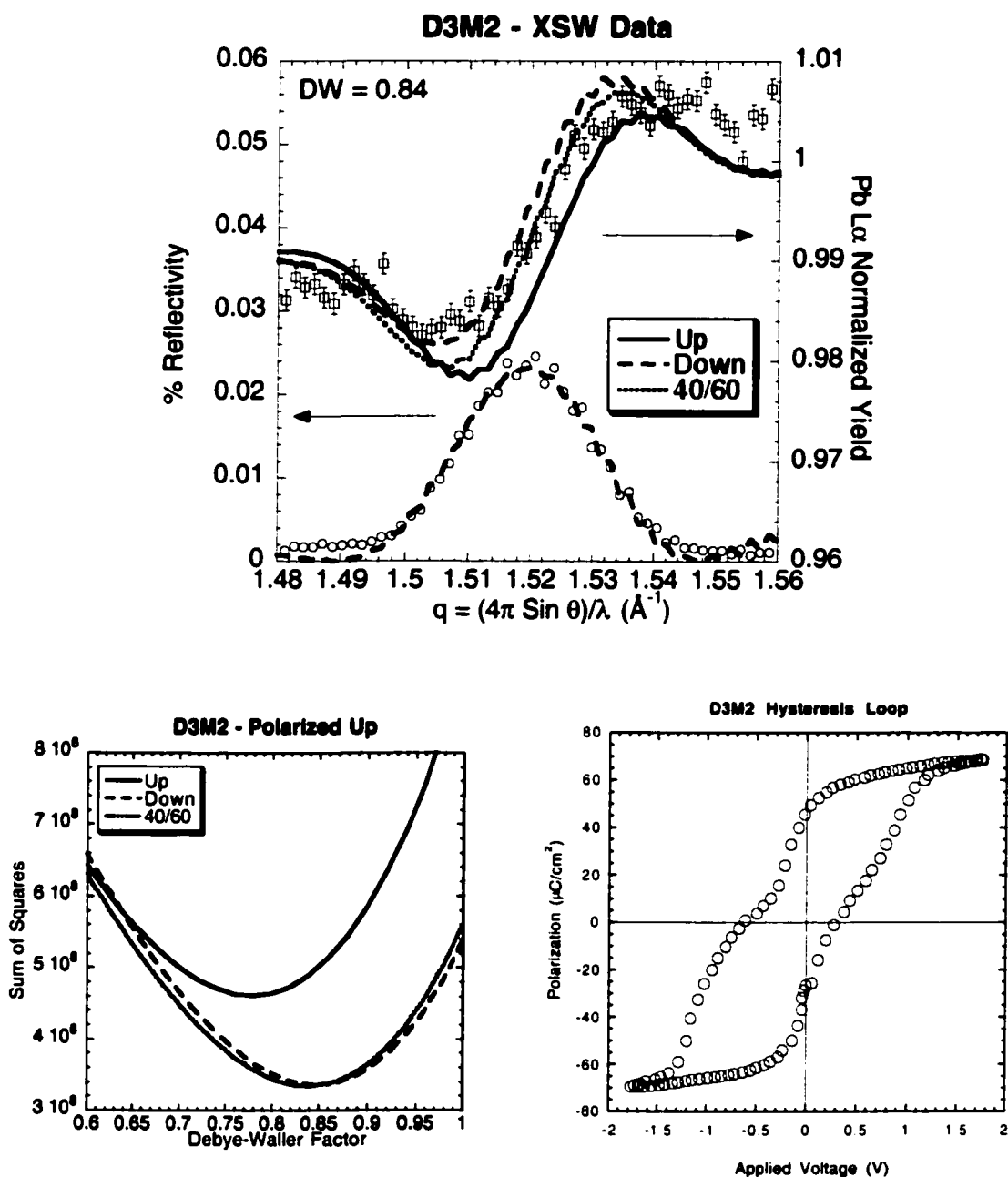


Figure 7.3.3 Capacitor D3M2: poled in the up orientation. Best fit by 40% Up - 60% Down mixture with a Debye-Waller factor of 0.84.

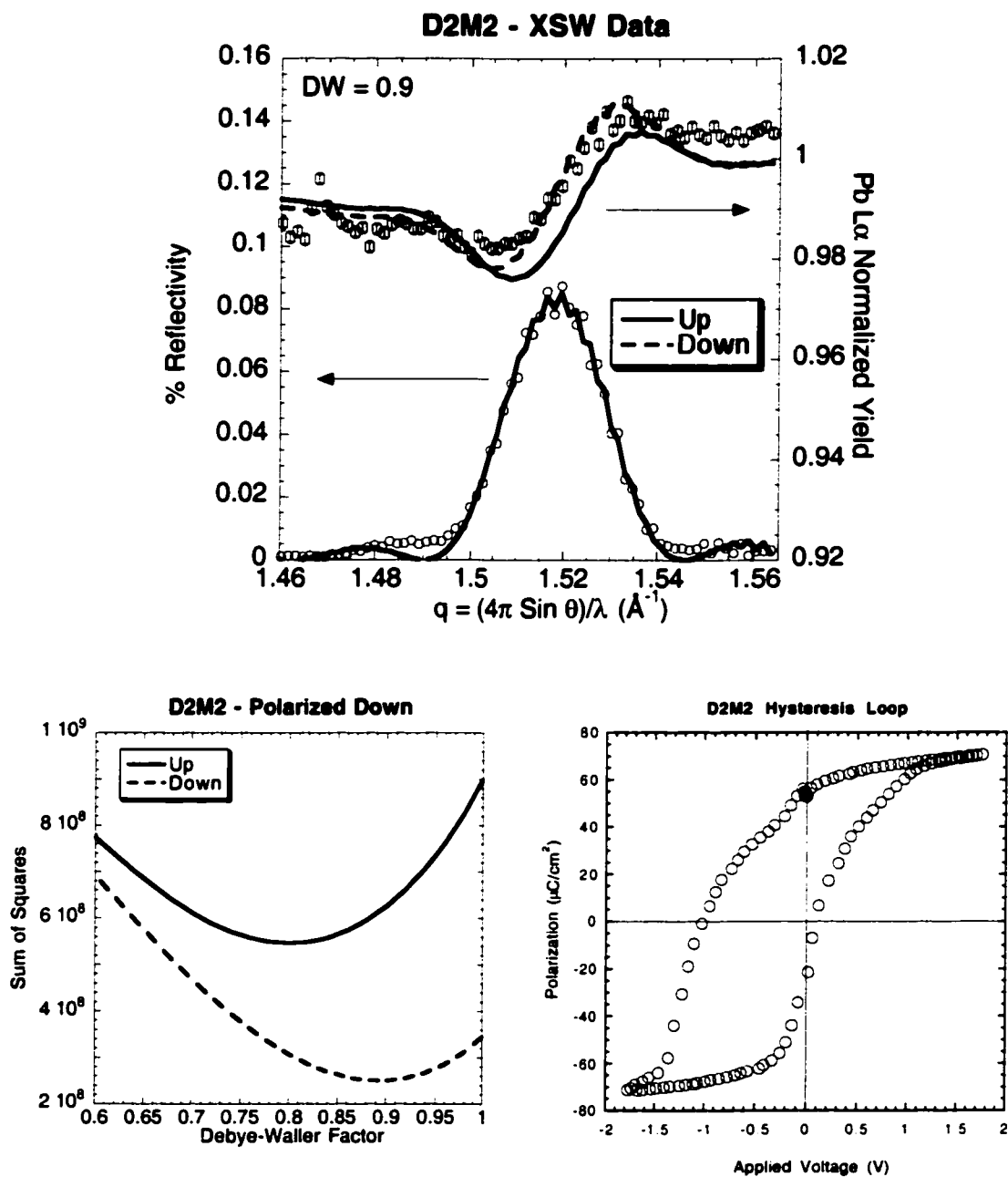


Figure 7.3.4 Capacitor D2M2: poled in the down orientation. Best fit by 100% Down with a Debye-Waller factor of 0.90.

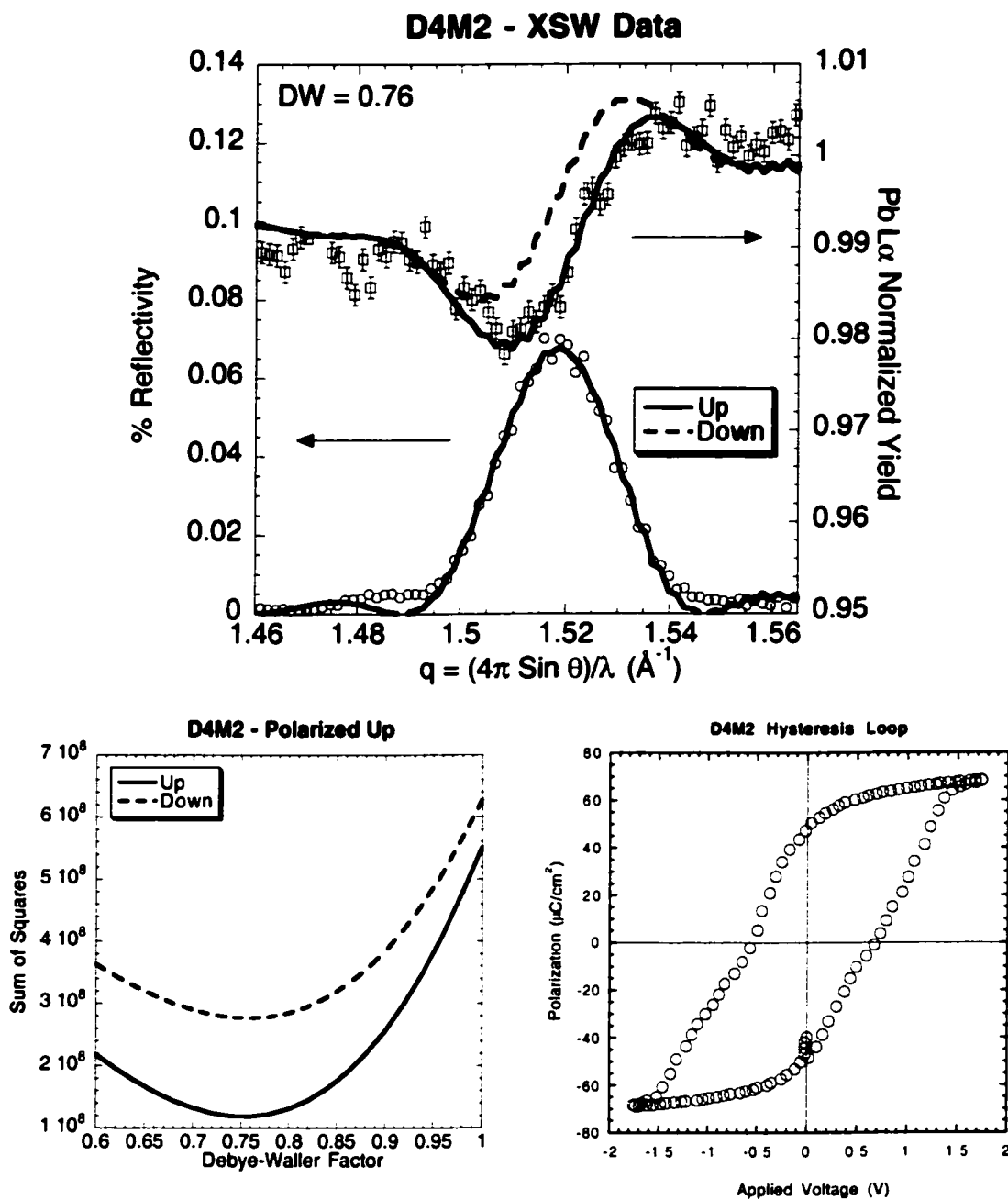


Figure 7.3.5 Capacitor D4M2: poled in the up orientation. Best fit by 100% Up with a Debye-Waller factor of 0.76.

7.4 Discussion of XSW Measurements

Four pre-poled ferroelectric capacitor structures were examined via the thin-film XSW method. Two were poled in the down orientation and two in the up orientation. The capacitors left in the down orientation best fit two simulations for down-oriented films. The first down capacitor, D2M0, most closely matched a film that was a 20% up – 80% down mixture, with a static Debye-Waller factor of 0.70; the second, D2M2, most closely matched a film that was 100% down, with a static Debye-Waller factor of 0.90. The two capacitors left polarized in the up orientation showed differing results. The first, D3M2, did not best fit an up-oriented film. It instead best fit a 40% up – 60% down mixture, with a static Debye-Waller factor of 0.84. However, the second capacitor, D4M2, did best fit a 100% up film with a static Debye-Waller factor of 0.76. The data and fits can be seen in Figures 7.3.1-7.3.4 of section 7.3.

The discrepancy in the data analysis for pad D3M2, the capacitor left in the up orientation but measured in the 40% up – 60% down state, can be explained by backswitching and is in agreement with the electrical measurements that showed a preferred down orientation for that capacitor. According to the thin-film XSW measurement, this particular poled-up capacitor reversed its polarization during the period between poling and x-ray measurements. In our PTO results in Chapter 6, it was shown that the thin films had a preferred as-grown polarity, as has been observed also in the literature [5]. Epitaxial thin films of perovskite ferroelectrics have shown a preferred orientation direction in their switching behavior. Examining the electrical hysteresis data in Figures 7.3.2 through 7.3.5, it can be seen that the loops are not symmetric about zero applied field, there is a preferred direction for switching. This shift is a sign of imprint, the tendency for ferroelectric capacitors to revert to a preferred state. The origin of imprint is unknown, but studies have shown a relationship with both asymmetric capacitor structures [6,7] and oxygen vacancies inside the films [8].

The PZT film used in this study was imprinted in the negative direction; a larger voltage was needed to switch the polarity of the film when the top electrode was negative rather than positive. The existence and direction of imprint is consistent with similar 400

Å PZT capacitor structures studied via x-ray scattering by Thompson [9]. The negative voltage on the top electrode corresponds to an up orientation of the ferroelectric film. Because of the asymmetry, the up orientation is termed the hard state and the down orientation the easy state. Note that there was bias in the selection of the capacitors. The two capacitors left in the down state, D2M0 and D2M2 (Figs. 7.3.2 and 7.3.4, respectively), are imprinted. Given the degree of imprint, these were not candidates for measurements where the capacitors would have been poled into the up orientation. The two cases where the capacitors were left in the up position, D3M2 and D4M2 (Figs. 7.3.3 and 7.3.5, respectively) show better imprint characteristics, but the capacitor that appears to have backswitched (D3M2) shows an asymmetry with an easy down state. Note that the other capacitor left in the up orientation (D4M2) suffers from almost no imprint. It is our belief that during the delay between poling and measurement, the film backswitched into its easy state, leaving it in the 40% up - 60% down mixture of polarizations. This measurement demonstrates the nondestructive nature of the XSW probe. We were able to examine the mixed capacitor and preserve the polarization orientation, whereas an electrical measurement would have destroyed the original state.

Several experiments can be suggested as successors to this study. The dynamics of backswitching can be examined. A capacitor can be poled into its hard state and thin-film XSW scans can then be performed on the sample, with data binned over time. As the capacitor switches to its easy state, this transition can be monitored via the XSW data. If the asymmetric nature of the capacitor structure is the cause of the imprint, then work could be done on growing capacitors with the same top and bottom electrodes, although the task of growing an epitaxial top electrode may or may not be trivial. Thompson's x-ray scattering work [9] suggests that in imprinted samples, the hard state may be a mixture of both up and down domains. A thin-film XSW study with an imprinted capacitor biased in the hard direction would confirm these findings. Finally, by combining the thin-film XSW method with x-ray microfocusing and *in situ* biasing, one could observe real-time switching; the x-ray beam could also be moved off the edge of the electrodes to see the effect of bias voltages on regions of PZT not directly under electrodes.

Chapter 8 - Summary

In the experiments for this dissertation we have investigated the ferroelectric-related Sr/Si(001) structure and ferroelectric thin films with x-ray techniques. The traditional x-ray standing wave (XSW) method was employed to determine the position of Sr atoms at sub-monolayer coverages on the Si (001) surface. The Si substrates were cleaned, etched, and then introduced into the UHV system at the 12ID-D undulator beamline at the Advanced Photon Source. Once in the UHV system, the substrates were outgassed and then annealed to create the clean dimerized Si (2x1) surface. Sr was then deposited from a Knudson cell at 350°C onto the room-temperature substrates. The deposition of Sr created a diffuse (3x1) surface reconstruction.

These (3x1) surfaces were then annealed at different temperatures for different periods of time in order to desorb some of the Sr and to promote the formation of well-ordered surface structures. Both a 10 minute anneal at 700°C and a 1 minute anneal at 750°C produced a (2x1) reconstruction when observed by LEED. The longer anneal at lower temperature desorbed more of the Sr, for a coverage of 0.31 ML, as compared to the 0.57 ML coverage of the 1 minute 750°C treatment. The coverages, measured after annealing, give credence to Hu's determination of surface structure as a function of coverage, also measured after annealing, as opposed to Fan's and Bakhtizin's, both who only measured as-deposited coverages. The XSW data for both the 0.31 and the 0.57 ML coverages are consistent with the symmetry demands for a cave or bridge site for the Sr atom. The 0.31 ML (2x1) reconstruction places the Sr atom closer to the bulk Si than does the 0.57 ML reconstruction.

The (3x2) reconstruction was found by annealing the 0.31 ML sample to 800°C for 1 minute, and by further annealing the 0.57 ML sample for another 10 minutes at 750°C. The low-coverage sample desorbed to 0.1 ML of Sr, while the high-coverage sample desorbed to 0.15 ML, again in agreement with Hu. The high-coverage sample was later annealed to 800°C for 1 minute, for a coverage of 0.13 ML. XSW data for the (3x2) samples were found to be consistent with the symmetry requirements for the cave or bridge site, STM studies in the literature rule out the bridge site. A possible reconstruction has chains of Sr atoms running perpendicular to the Si dimer rows, once every three cave sites. Note that the positions of the Sr atoms are consistent with the non-annealed (3x1) and high coverage (2x1) reconstructions. Extending the findings of the (3x2) surface to the (2x1) surface, a model with Sr atoms in every cave site is possible.

Epitaxial thin films of PbTiO_3 (PTO) were grown on SrTiO_3 (001) substrates. PTO, a ferroelectric perovskite, can exist in two stable polarities at room temperature. We used thin-film x-ray standing waves to measure the as-grown polarities of 100, 200, 400 and 600 Å thick films of PTO.

The thin-film XSW method is an extension of the traditional XSW measurement, which exploits the standing wave field created by the interference between incoming and diffracted plane waves in and above a crystal in the Bragg condition. In the thin-film method, the film itself rather than the substrate crystal is used to generate the XSW field. This field has the same periodicity as the diffraction planes in the film that created the Bragg reflection, and hence can be used in conjunction with fluorescence or other secondary radiation to probe the film.

For the films below the critical thickness (500 – 700 Å), we found that the PTO favored growth in a unipolar direction. Ten of the 11 reflections best fit 100% of the domains oriented in one direction. This measurement was performed over a 0.4 mm x 1.6 mm footprint, indicating good uniform film growth. In addition, 9 of the 10 unipolar reflections found the film growing in the up orientation. This is possibly due to the composition of the top layer of the STO substrate, experiments with this as a variable would be of interest. Measurements involving the Ti fluorescence signal from the film made use of the evanescent-wave emission effect to prevent Ti fluorescence from the bulk and acted to confirm the findings of the Pb fluorescence measurements. The 600 Å samples were found to be of lower quality, possibly due to the introduction of *a* domains as a stress relief mechanism.

The next step was to use the thin-film XSW method on a switched system. Ferroelectric capacitor structures were grown on a SrTiO₃ substrate, using SrRuO₃ as a bottom electrode, 200 Å of Pb(Zr_{0.3}Ti_{0.7})O₃ as a switchable dielectric, and a polycrystalline layer of Ag as a top electrode. The capacitors were then tested electrically for switching behavior and were left in either an up or a down orientation.

After slitting down the beam to the proper size for the Ag top electrode and using Ag fluorescence from those electrodes to navigate on the sample, four capacitors were probed with the thin-film XSW method. Of the capacitors poled in the down orientation, both remained in the down orientation. Of the two capacitors poled in the up orientation, one was found in the up orientation, and the other was in a mixed state, best fitting 40% up and 60% down. This was consistent with the electrical measurements performed on

the sample, which showed it to be heavily imprinted, and likely to backswitch to the preferred down orientation. The up-oriented capacitor that did not backswitch showed little evidence of imprint.

Future studies of ferroelectric thin films should make use of microfocusing optics and multi-element detectors in order to decrease measurement time. *In situ* switching experiments are of interest, along with backswitching measurements for imprinted samples.

References

Chapter 2

- [1] F. Jona and G. Shirane, *Ferroelectric Crystals* (Dover, New York, 1993).
- [2] R. Ramesh, S. Aggarwal and O. Auciello, *Mat Sci Eng R* **32**, 191 (2001).
- [3] A.I. Kingon, S.K. Streiffer, C. Basceri and S.R. Summerfelt, *MRS Bulletin*, **21**, 46 (1996).
- [4] A.I. Kingon, J.P. Maria and S.K. Streiffer, *Nature* **406**, 1032 (2000).
- [5] O. von Hippel, R.G. Breckenridge, F.G. Chesley and L. Tisza, *Ind. Eng. Chem.* **38**, 1097 (1946).
- [6] B. Wul and I.M. Goldman, *Compt. Rend. Acad. Sci. U.R.S.S.* **46**, 139 (1945); **49**, 177 (1945); **51**, 21 (1946).
- [7] O. Auciello, J.F. Scott and R. Ramesh, *Phys. Today* **51**, 22 (1998).
- [8] K. Iijima, R. Takayama, Y. Tomita and I. Ueda, *J. Appl. Phys.* **60**, 2914 (1986).
- [9] O. Auciello, K.D. Gifford and A.L. Kingon, *Appl. Phys. Lett.* **64**, 2873 (1994).
- [10] R. Ramesh, A. Inam, W.K. Chan, B. Wilkens, K. Myers, K. Remschnig, D.L. Hart and J.M. Terascon, *Science* **252**, 944 (1991).
- [11] R.A. McKee, F.J. Walker and M.F. Chisholm, *Phys. Rev. Lett.* **81**, 3014 (1998).
- [12] X. Yu and J.D. Mackenzie, *Integrated Ferroelectrics* **1**, 17 (1992).
- [13] M. Klee and U. Mackens, *Microelectron. Eng.* **29**, 185 (1995).
- [14] C.M. Foster, Z. Li, M. Buckett, D. Miller, P.M. Baldo, L.E. Rehn, G.R. Bai, D. Guo, H. You and K.L. Merkle, *J. Appl. Phys.* **78**, 2607 (1995).
- [15] C.M. Foster, ANL internal report.
- [16] S. Stemmer, S.K. Streiffer, F. Ernst, M. Ruhle, W.Y. Hsu and R. Raj, *Solid State Ionics* **75**, 43 (1995).
- [17] F. Saurenback and B.D. Terris, *Appl. Phys. Lett.* **56**, 1703 (1990).

- [18] R. Luthi, H. Haefke, K.-P. Meyer, E. Meyere, L. Howald and H.-J. Guntherodt, *J. Appl. Phys.* **74**, 7461 (1993).
- [19] A. Gruverman, O. Auciello and H. Tokumoto, *Appl. Phys. Lett.* **69**, 3191 (1996).
- [20] A. Gruverman, H. Tokumoto, A.S. Prakash, S. Aggarwal, B. Yang, M. Wutting, R. Ramesh, O. Auciello and T. Venkatesan, *Appl. Phys. Lett.* **71**, 3492 (1997)
- [21] A. Munkholm, S.K. Streiffer, M.V.R. Murty, J.A. Eastman, C. Thompson, O. Auciello, L. Thompson, J.F. Moore and G.B. Stephenson, *Phys. Rev. Lett.* **88**, 016101 (2002).
- [22] S.K. Streiffer, J.A. Eastman, D.D. Fong, C. Thompson, A Munkholm, M.V.R Murty, O. Auciello, G.-R. Bai, G.B. Stephenson, *Phys Rev Lett.* **89**, 067601 (2002).
- [23] Schwartz & Cohen, *Diffraction from Materials* (Springer-Verlag, Berlin, 2^d ed, 1987).
- [24] C. Thompson, C.M. Foster, J.A. Eastman and G.B. Stephenson, *Appl. Phys. Lett.* **71**, 3516 (1997).
- [25] C. Thompson, A. Munkholm, S.K. Streiffer, G.B. Stephenson, K. Ghosh, J.A. Eastman, O. Auciello, G.R. Bai, M.K. Lee and C.B. Eom, *Appl. Phys. Lett.* **78**, 3511 (2001).

Chapter 3

- [1] M.J. Bedzyk and G. Materlik, *Phys. Rev. B.* **32**, 6456 (1985).
- [2] B.W. Batterman, *Phys. Rev.* **133**, A759 (1964).
- [3] B.W. Batterman, *Phys. Rev. Lett.* **22**, 703 (1969).
- [4] P.L. Cowan, J.A. Golovchenko and M.F. Robbins, *Phys. Rev. Lett.* **44**, 1680 (1980).
- [5] J. Zegenhagen, *Surf. Sci. Rep.* **18**, 199 (1993).
- [6] A. Kazimirov, T. Haage, L. Ortega, A. Stierle, F. Comin and J. Zegenhagen, *Solid State Commun.* **104**, 347 (1997).

- [7] S. Takagi, *J. Phys. Soc. Jpn*, **26**, 1239 (1969).
- [8] D. Taupin, *Bull. Soc. Fr. Mineal. Crystallogr.* **87**, 469 (1964).
- [9] W.J. Bartels, J. Hornstra and D.J.W. Lobeek, *Acta Crystallogr.* **A42**, 539 (1986).
- [10] T.-L. Lee, Ph.D. thesis, Northwestern University, Evanston, 1999.
- [11] B.W. Batterman and H. Cole, *Rev. Mod. Phys.* **36**, 681 (1964).
- [12] U. Bonse and W. Graeff, *X-Ray Optics: Applications to Solids (Topics in Applied Physics, Vol22)* (Springer-Verlag, Berlin, 1977).
- [13] R.S. Becker, J.A. Golovchenko and J.R. Patel, *Phys. Rev. Lett.* **50**, 153 (1983).
- [14] T.-L. Lee, Y. Qian, P.F. Lyman, J.C. Woicik, J.G. Pellegrino and M.J. Bedzyk, *Physica B* **221**, 437 (1996).
- [15] P. Lorrain and D.R. Corson, *Electromagnetic Fields and Waves* (W.A. Freeman, San Francisco, 2^d ed, 1970).
- [16] M. Born and E. Wolf, *Principles of Optics* (Pergammon Press, New York, 6th ed., 1993).
- [17] I.K. Robinson, R.T. Tung and R. Feidenhans'l, *Phys Rev B.* **38**, 3632 (1988).
- [18] C. Thompson, C.M. Foster, J.A. Eastman and G.B. Stephenson, *Appl. Phys. Lett.* **71**, 3516 (1997).
- [19] D. Waasmaier and A. Kirfel, *Acta Crystallogr.* **A51**, 416 (1995).

Chapter 4

- [1] A. Krolzig, G. Materlik, M. Swars and J. Zegenhagen, *Nucl. Instrum. Meth.A* **219**, 430 (1984).

Chapter 5

- [1] R.A. McKee, F.J. Walker and M.F. Chisholm, *Phys. Rev. Lett.* **81**, 3014 (1998).

- [2] A.I. Kingon, J.P. Maria and S.K. Streiffer, *Nature* **406**, 1032 (2000).
- [3] J. Ramdani, *Bull. Am. Phys. Soc.* **46**, 767(2002).
- [4] X.M. Hu, Z. Yu, J.A. Curless, R. Droopad, K. Eisenbeiser, J.L. Edwards, W.J. Ooms and D. Sarid, *Appl. Surf. Sci.* **181**, 103 (2001).
- [5] F. Sanchez, M. Varela, X. Queralt, R. Aguiar, J. L. Morenza, *Appl. Phys. Lett.* **61**, 2228 (1992).
- F. Sanchez, R. Aguiar, V. Trtik, C. Guerrero, C. Ferrater, M. Varela, *J. Mat. Res.* **13**, 1422 (1998).
- O. Nakagawara, M. Kobayashi, Y. Yoshino, Y. Katayama, H. Tabata, T. Kawai, *J. Appl. Phys.* **78**, 7226 (1995).
- H. Mori, H. Ishiwara, *Jpn. J. Appl. Phys.*, **30** L1415 (1991).
- B. K. Moon, H. Ishiwara, *Jpn. J. Appl. Phys.*, **33** 1472 (1994).
- [6] W.C. Fan, N.J. Wu and A Ignatiev, *Phys. Rev. B* **42**, 1254 (1990).
- [7] R.Z. Bakhtizin, J. Kishimoto, T. Hashizume and T. Sakurai, *Appl Surf. Sci.* **94/95**, 478 (1996).
- [8] R.Z. Bakhtizin, J. Kishimoto, T. Hashizume and T. Sakurai, *J. Vac. Sci. Technol. B* **14**, 1000 (1996).
- [9] P.J. Bedrossian, Ph.D. thesis, Harvard University, Cambridge, 1989.
- [10] A. Ishizaka and Y. Shiraki, *J. Electrochem. Soc.* **133**, 666 (1986).
- [11] Y. Qian, Ph.D. thesis, Northwestern University, Evanston, 1995.
- [12] The asymmetric assumption was required due to poor sample alignment during the measurement. This changes the sample's b-factor. Proper treatment can be found in J. Zegenhagen, *Surf. Sci. Rep.* **18**, 199 (1993).

Chapter 6

- [1] F. Jona and G. Shirane, *Ferroelectric Crystals* (Dover, New York, 1993).

- [2] R.W. Schwartz, R.A. Assink and T.J. Headley, *Mater. Res. Soc. Symp. Proc.* **243**, 254 (1993).
- [3] K. Shimomura, T. Tsurami, Y. Ohba and M. Daimon, *Jap. J. Appl. Phys.* **30**, 2174 (1991).
- [4] T. Fukami, I. Minemura, Y. Hiroshima and T. Osada, *Jap. J. Appl. Phys.* **30**, 2155 (1991).
- [5] O. Auciello, K.D. Gifford and A.I. Kingon, *Appl Phys. Lett.* **58**, 36 (1991).
- [6] R.Ramesh, T.Sands and V.G. Keramidas, *J. Electron. Mater.* **23**, 19 (1994).
- [7] C.M. Foster, R. Csencsits, G.R. Bai, Z. Li, L.A. Wills, R. Hiskes, H.N. Al-Shareef and D. Dimos, *Integrated Ferroelectrics* **10**, 31 (1995).
- [8] C.M. Foster, ANL internal report.
- [9] C.M. Foster, Z. Li, M. Buckett, D. Miller, P.M. Baldo, L.E. Rehn, G.R. Bai, D. Guo, H. You and K.L. Merkle, *J. Appl. Phys.* **78**, 2607 (1995).
- [10] R.S. Becker, J.A. Golovchenko and J.R. Patel, *Phys. Rev. Lett.* **50**, 153 (1983).
- [11] C. Thompson, C.M. Foster, J.A. Eastman and G.B. Stephenson, *Appl. Phys. Lett.* **71**, 3516 (1997).
- [12] H. Nagai, *J. Appl. Phys.* **45**, 3789 (1974).
- [13] Y. Sakashita, T. Ono, H. Segawa, K. Tominaga and M. Okada, *J Appl. Phys.* **69**, 8352 (1991).
- [14] M. Kawasaki, A. Ohtomo, T. Arakane, K. Takahashi, M. Yoshimoto and H. Koinuma, *Appl. Surf. Sci.* **107**, 102 (1996).
- [15] M.J. Bedzyk and G. Materlik, *Phys Rev B.* **32** 6456 (1985).

Chapter 7

- [1] C.B. Eom, R.J. Cava, R.M. Fleming, J.M. Phillips, R.B. van Dover, J.H. Marshall, J.W.P. Hsu, J.J. Krajewski and W.F. Peck, Jr., *Science* **258**, 1766 (1992).

- [2] Q. Gan, R. A. Rao, and C. B. Eom, *Appl. Phys. Lett.* **70**, 1962 (1997).
- [3] C.M. Foster, G.R. Bai, R. Csencsits, J. Vetrone, R. Jammy, L.A. Wills, E. Carr and J. Amano, *J. Appl. Phys.* **81**, 2349 (1997).
- [4] F. Jona and G. Shirane, *Ferroelectric Crystals* (Dover, New York, 1993).
- [5] C. Thompson, C.M. Foster, J.A. Eastman and G.B. Stephenson, *Appl. Phys. Lett.* **71**, 3516 (1997).
- [6] J. Lee, A. Safari and R.L. Pfeffer, *Appl. Phys. Lett.* **61**, 1643 (1992).
- [7] J. Lee, L. Johnson, A. Safari, R. Ramesh, T. Sands, H. Gilchrist and V.G. Keramidas, *Appl. Phys. Lett.* **63**, 27 (1993).
- [8] G.E. Pike, W.L. Warren, D. Dimos, B.A. Tuttle, R. Ramesh, J. Lee, V.G. Keramidas and J.T. Evans, *Appl. Phys. Lett.* **66**, 484 (1995).
- [9] C. Thompson, A. Munkholm, S.K. Streiffer, G.B. Stephenson, K. Ghosh, J.A. Eastman, O. Auciello, G.R. Bai, M.K. Lee and C.B. Eom, *Appl. Phys. Lett.* **78**, 3511 (2001).

Appendix 1 – Software Written for Data Analysis

A1.1 - Introduction

In order to fit the thin-film XSW data collected in the ferroelectric experiments, it was necessary to write code to generate theoretical reflectivity and fluorescence curves, and to compare these curves to the actual data. The programs were written in MATLAB. The earliest versions of the code were based upon a program written in Igor by Tien-Lin Lee. In addition, code was written in MATLAB to fit the reflectivity data taken over the longer range in the crystal truncation rod measurement. This appendix will describe the two pieces of software.

A1.2 – Description of the XSW Fitting Software

The software written for the XSW analysis consists of a two-step process. For a given Debye-Waller factor and up ratio percentage, the reflectivity is fit for thickness, q-offset and a scaling factor.

The boss.m routine has a pair of nested loops that increment through up ratio and Debye-Waller factor values. At each value pair, the worker.m routine is called, and the output of worker.m, the weighted least-squares sum for the fluorescence fit, is written to a file. The counter.m routine is used to consolidate the individual data files, and the rprint.m and fprint.m routines can be used after the fits have been performed to output the fits to the file.

Worker.m first calls upon ffitter.m, which performs a weighted least-squares fit upon the reflectivity data using film thickness, q offset and a scaling factor as fitting

parameters. The reflectivity is calculated by the formulae discussed in Chapter 3. A flowchart detailing the process used to calculate the reflectivity and fluorescence is found in section A1.3, and the individual routines are detailed in section A1.4. After the reflectivity is fit, the q offset and film thickness are passed to the `flumake.m` routine, which generates the fluorescence signal from the film by summing fluorescences at various depths in the film. The `ffitter.m` routine then adjusts an overall scaling factor and a factor to account for the changing size of the footprint on the film with angle, minimizing a sum of squares between the fluorescence data and the fit. Again, flowcharts and programming details can be found in sections A1.3 and A1.4, respectively.

The XSW fitting routine is slightly modified in the case of the PZT data. Another iteration is used to account for the bottom electrode. Also, as careful measurements were made at the beamline, the footprint correction is not used as a fitting parameter.

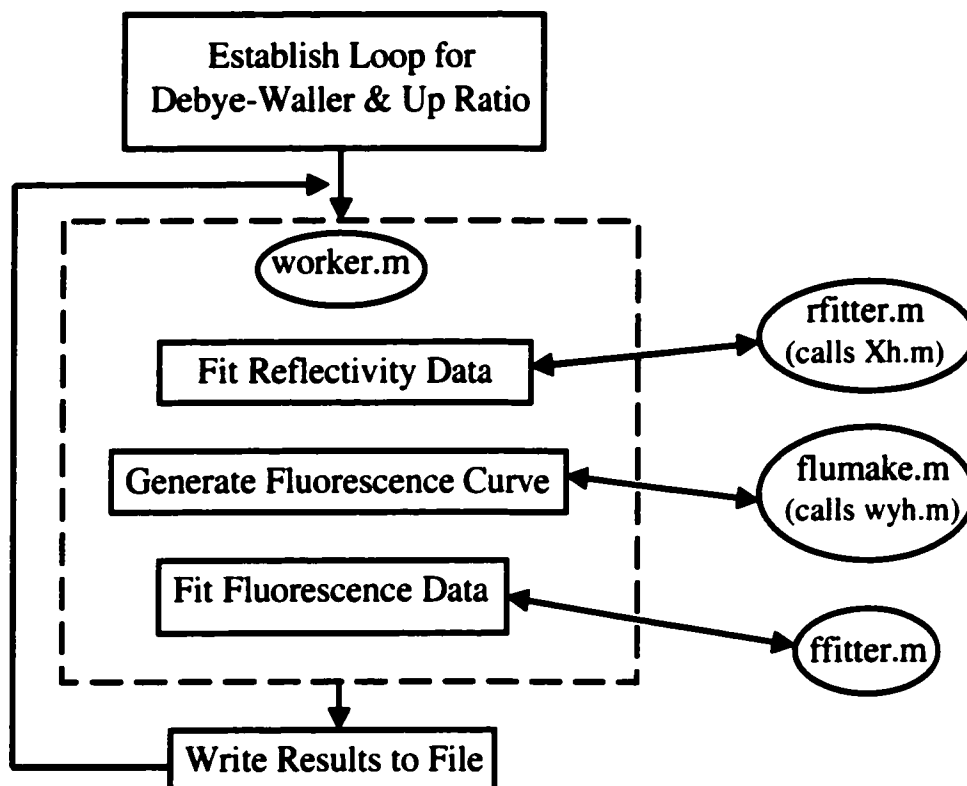
A1.3 – Flow Charts of the XSW Fitting Program

Figure A1.3.1 – Flow chart for the boss.m routine. Boss.m runs the XSW fit. It first establishes a pair of nested loops to increment values of the Debye-Waller factor and the Up ratio. It then calls the worker.m routine, which is diagramed in the dashed box. Worker.m calls rfitter.m to fit the reflectivity data, and then uses information from that fit to create a theory curve for the fluorescence in the flumake.m routine. This theory curve is then fit to the data in the ffitter.m routine. Worker.m returns details of the fits to boss.m, which writes them to a file.

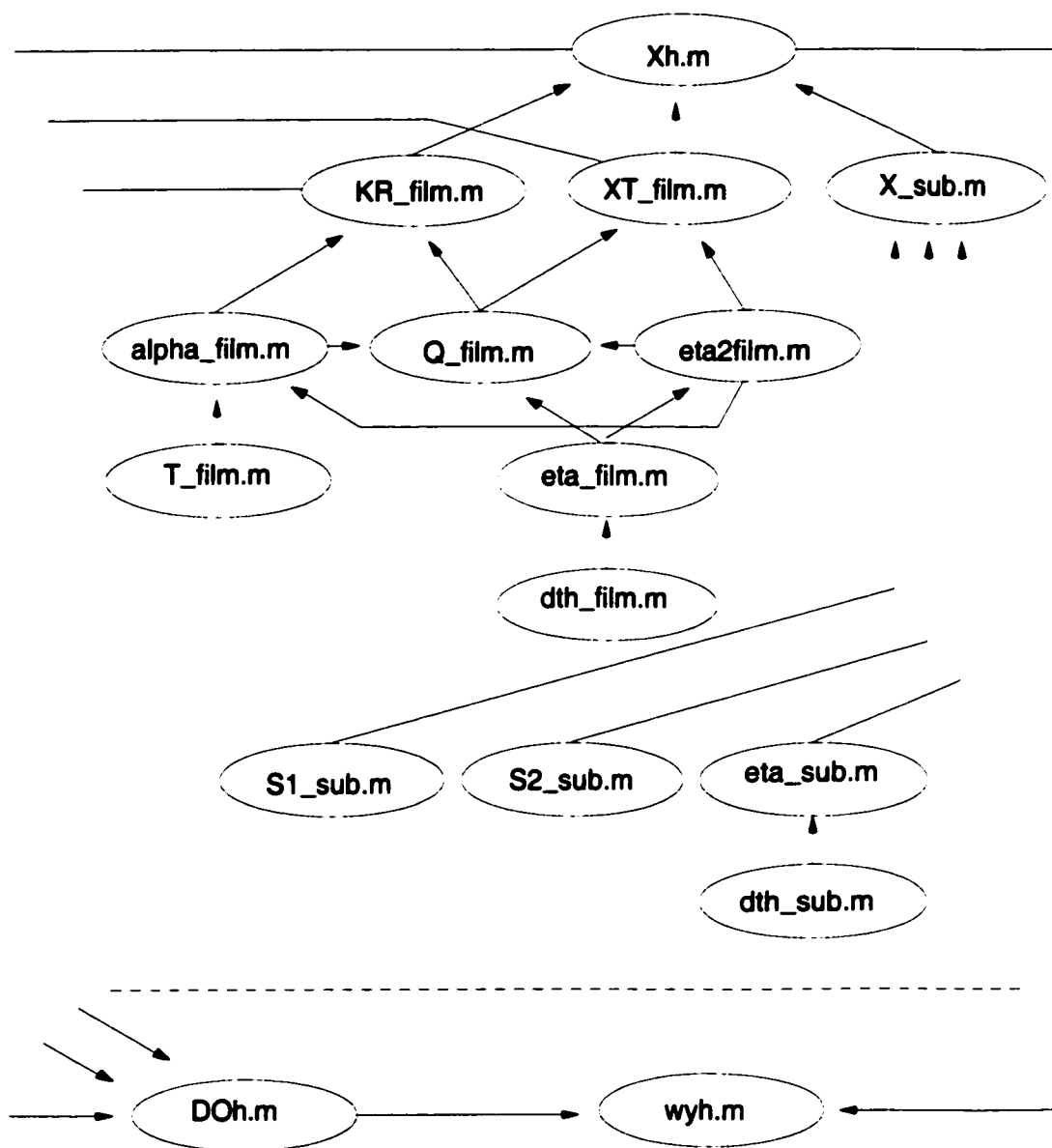


Figure A1.3.2 - Flow chart relating Xh.m, wyh.m and their components. This diagram details how the reflectivity and fluorescence are built up from the more basic components.

A1.4 - Description of Routines for the XSW Fitting Program

The XSW fitting program was written in MATLAB. The individual parts of the program are listed here, with the routines that call them, the routines they call upon, their purpose, and if applicable, the formula from Chapter 3 they represent.

alpha_film.m

Calls T_film.m, eta2film.m
 Called by KR_film.m, Q_film.m
 Purpose Calculates the quantity α for the film.
 Equation 3.3.9

boss.m

Calls worker.m
 Called by Executed by user
 Purpose Sets up loops to feed worker.m Debye-Waller and up-ratio percentage, records fit results in files.

counter.m

Called by Executed by user
 Purpose Collects data fit files from boss.m and prints into one file.

defvar.m

Called by flumake.m, rfitter.m
 Purpose Sets all the variables needed by the fitting program.

DOh.m

Calls XT_film.m, Xh, KR_film
 Called by wyh.m
 Purpose Calculates the total amplitude for the reflection.
 Equation 3.3.25

dth_film.m

Called by eta_film.m
 Purpose Calculates $\Delta\theta$ from q for the film.

dth_sub.m

Called by eta_sub.m, Q_film.m
 Purpose Calculates $\Delta\theta$ from q for the substrate.

eta2film.m

Calls eta_film.m
 Called by alpha_film.m, Q_film.m, XT_film.m
 Purpose Calculates $(\eta^2 - 1)^{0.5}$

eta_film.m

Calls dth_film.m
 Called by eta2film.m
 Purpose Calculates η for the film.
 Equation 3.3.6

eta_sub.m

Calls dth_sub.m
 Called by S1_sub.m, S2_sub.m
 Purpose Calculates η for the substrate.
 Equation 3.3.6

ffitter.m

Called by worker.m
 Purpose Minimizes a sum of squares between the fit and data, adjusting a scale factor and a correction for angle.

flumake.m

Calls defvar.m, wyh.m
 Called by fprint.m, worker.m
 Purpose Builds the fluorescence signal, based upon Debye-Waller and up ratio seeds and results from the reflectivity fit.

fprint.m

Calls flumake.m
 Called by Executed by user.
 Purpose Prints fluorescence output file based upon user input.

KR_film.m

Calls alpha_film.m, q_film.m
 Called by Doh.m, Xh.m
 Purpose Calculates χ .
 Equation 3.3.10

Q_film.m

Calls eta2film.m, eta_film.m, alpha.m
 Called by KR_film.m, XT_film.m
 Purpose Calculates Q for the film.
 Equation 3.3.11

rfitter.m	
Calls	defvar.m, Xh.m
Called by	worker.m
Purpose	Minimizes a sum of squares between the fit and data, adjusting a scale factor, thickness, and a q-offest.
rprint.m	
Calls	defvar.m, Xh.m
Called by	Executed by user
Purpose	Prints reflectivity output file based upon user input.
S1_sub.m	
Calls	eta_sub.m,
Called by	X_sub.m
Purpose	Calculates a quantity used in substrate reflectivity.
S2_sub.m	
Calls	eta_sub.m
Called by	X_sub.m
Purpose	Calculates a quantity used in substrate reflectivity.
T_film.m	
Called by	alpha_film.m
Purpose	Calculates T for the film.
Equation	3.3.7
worker.m	
Calls	rfitter.m, flumake.m, ffitter.m
Called by	Boss.m
Purpose	Performs the reflectivity and fluorescence fits.
wyh.m	
Calls	Xh.m, Doh.m
Called by	flumake.m
Purpose	Calculates the fluorescence for a given Debye-Waller factor, up ratio and film thickness.
Xh.m	
Calls	KR_film.m, X_sub.m, XT_film
Called by	rfitter.m, Doh.m, wyh.m
Purpose	Calculates X_h for the film.
Equation	3.3.17

XT_film.m

Calls eta2film.m, Q_film.m

Called by DOh.m, Xh.m

Purpose Calculates X_T .

Equation 3.3.23

X_sub.m

Calls eta_sub.m, S1_sub.m, S2_sub.m

Called by Xh.m

Purpose Calculates the reflectivity for the substrate.

A1.5 – Description of CTR Fitting Software

The software written in MATLAB for the CTR analysis can be run through a graphical user interface. Through this, the user can enter fitting parameters and choose one of three options. The first option is to perform a probe, a one-pass fit that calculates the reflectivity based upon the user input and compares this to the data. The second option is to perform a least-squares fit using the user's input as a seed. The final option is to print the fit based upon the user input into a file.

All three choices calculate the reflectivity from the CTR based upon the formulae found in section 3.5. A flowchart detailing the process used to calculate the reflectivity is found in section A1.6, and the individual routines are detailed in section A1.7. Reflectivity is calculated for both the film and substrate, and then summed at the level of fields. The fitting parameters include factors accounting for the roughness of the substrate and film, the offset between the substrate and film, the c -axis lattice parameter of the film, the fraction of up domains in the film, the thickness of film measured in unit cells, the Gaussian spread in the film thickness, and an overall scaling factor.

With the large number of fitting parameters, it is desirable to perform many fits automatically and record the results. This is done via the `workfit.m` routine, which takes seeds from the seeder file and records the result of each fit. The `counter.m` routine takes the output files from `workfit.m` and collects them into one file.

A1.6 – Flow Charts of the CTR Fitting Program

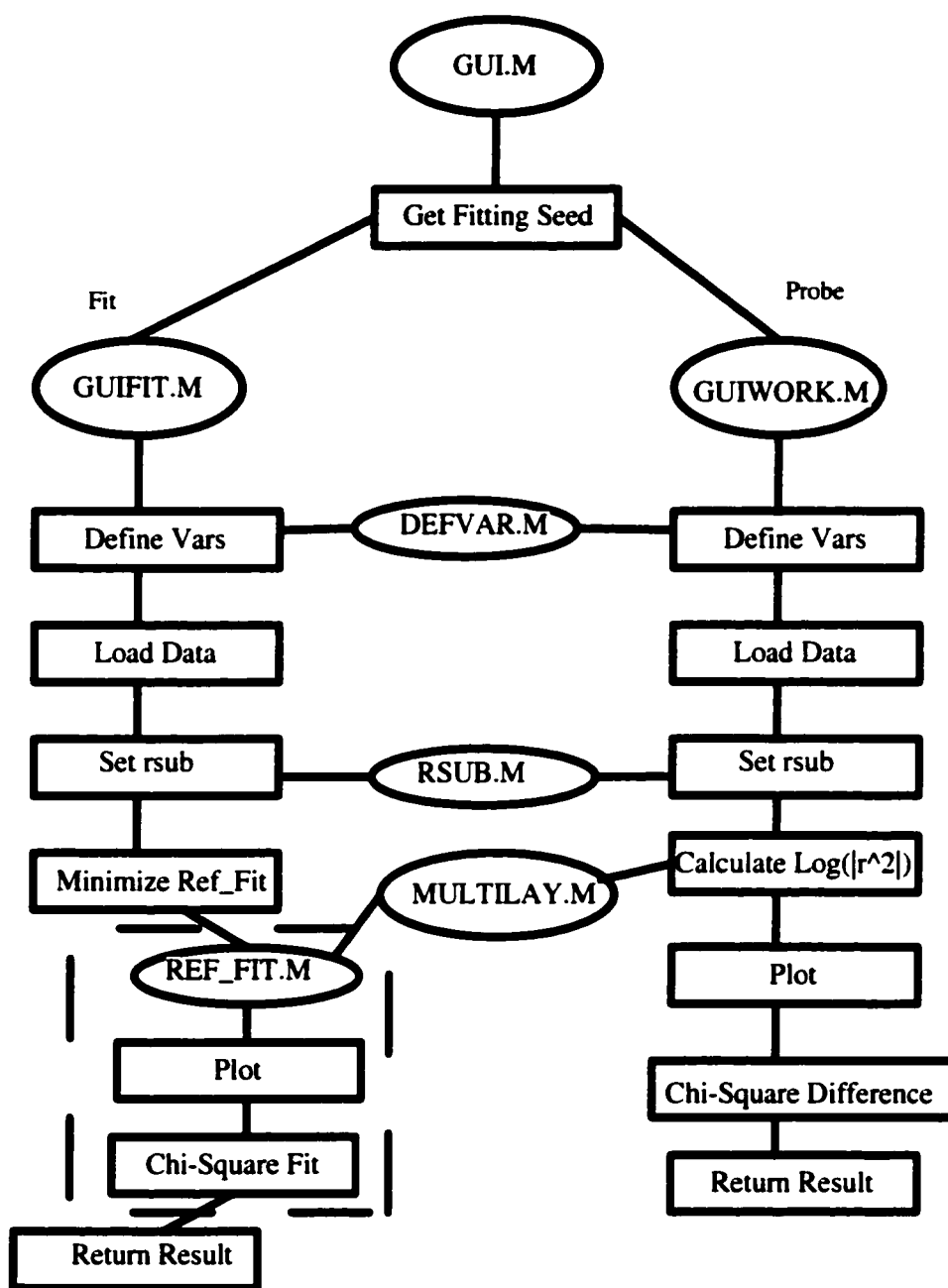


Figure A1.6.1 – Flow chart detailing the CTR fitting routines.

A1.7 - Description of Routines for the CTR Fitting Program

The XSW fitting program was written in MATLAB. The individual parts of the program are listed here, with the routines that call them, the routines they call upon, their purpose, and if applicable, the formula from Chapter 3 they represent.

counter.m

Called by Executed by user
Purpose Collects data fit files from workfit.m and prints into one file.

defvar.m

Called by guifit.m, guiprint.m, guiwork.m, workfit.m
Purpose Sets the variables needed by the fitting program.

Ffilm.m

Calls pb.m, ti.m, o.m
Called by rfilm.m
Purpose Calculates the structure factor of the film.

Fsub.m

Calls sr.m, ti.m, o.m
Called by
Purpose Calculates the structure factor of the substrate.

gui.m

Calls guifit.m, guiwork.m or guiprint.m
Purpose Graphical user interface to let user set fitting parameters and call routines to single-iteration fit the data, fit the data, or print the fit.

guifit.m

Calls defvar.m, rsub.m ref_fit.m
Called by gui.m
Purpose Performs a minimization on the output of ref_fit.

guiprint.m

Calls defvar.m, rsub.m, multilay.m
Called by gui.m
Purpose Prints the fit into a file.

guiwork.m

Calls

defvar.m, rsub.m, multilay.m

Called by

gui.m

Purpose

Performs a one-pass least-squares fit upon the data.

multilay.m

Calls

rtotal.m

Called by

guiprint.m, guiwork.m, ref_fit.m

Purpose

Accounts for a Gaussian spread in film thicknesses by performing a weighted average.

o.m

Called by

Fsub.m, Ffilm.m

Purpose

Calculates atomic form factor for O.

pb.m

Called by

Ffilm.m

Purpose

Calculates atomic form factor for Pb.

ref_fit.m

Calls

multilay.m

Called by

guifit.m, workfit.m

Purpose

Calculates the sum of squares difference between the fit and data.

rfilm.m

Calls

Ffilm.m

Called by

rtotal.m

Purpose

Calculates the reflectivity from the film.

Equation

3.5.4

rsub.m

Calls

Fsub.m

Called by

guifit.m, guiprint.m, guiwork.m, workfit.m

Purpose

Calculates the reflectivity from the substrate.

Equation

3.5.2

rtotal.m

Calls

rfilm.m

Called by

multilay.m

Purpose

Calculates the reflectivity from the film/substrate system.

Equation

3.5.5

seeder

Called by

Purpose

workfit.m

Data file containing an array of seeding information.

sr.m

Called by

Purpose

Fsub.m

Calculates atomic form factor for Sr.

ti.m

Called by

Purpose

Fsub.m, Ffilm.m

Calculates atomic form factor for Ti.

workfit.m

Calls

Called by

Purpose

seeder, defvar.m, rsub.m, ref_fit.m

Executed by user

Allows for fitting from a file of seeds.